Politecnico di Torino

Politecnico di Torino

Master's Degree in Aerospace Engineering

A.A. 2025/2026

Graduation Session March/April 2026

Development of advanced structural analysis and monitoring techniques for pressurized lunar rovers

Supervisors:

Erasmo Carrera

Alfonso Pagani

Marco Petrolo

Karim Abu Salem

Candidate:

Angelo Carriere

Abstract

This thesis evaluates a numerical framework for Lamb-wave-based structural health monitoring (SHM) of aerospace thin-walled structures, with a focus on the skins and substructures of pressurized rovers where accurate multilayer models and robust diagnostics are required. The work builds on the Carrera Unified Formulation (CUF), exploiting through-thickness expansions with different accuracy–cost levels to model composite plates and shells and to assess when simplified kinematics remain valid. A simplified representation of a piezoelectric actuator–sensor network is also included to simulate guided-wave generation, propagation, scattering, and interaction with typical damage mechanisms.

Dispersion characteristics, time-of-flight, amplitude variations, and wavenumber content are analyzed to quantify h/p convergence and to assess damage sensitivity across modeling choices.[1] The results show the regimes in which equivalent single-layer theories fail and layer-wise descriptions become necessary to correctly capture interlaminar phenomena and damage-related signatures, highlighting explicit trade-offs between computational effort and diagnostic fidelity.

Damage localization is further investigated through a machine-learning-based model that processes wave-response features extracted from the CUF simulations to estimate the damage position within the monitored structure. This section lays the groundwork for a modular, high-complexity SHM capability that will require additional integrations to reliably reproduce structural response in harsh lunar operating conditions.

[1] Here, h/p convergence refers to the numerical convergence of the finite-element model with respect to spatial discretization, achieved either by reducing the characteristic element size h (mesh refinement) or by increasing the polynomial order p of the element shape functions.

Table of Contents

List of Tables

List of Figures

Glossary

AI

Artificial intelligence

BEM

Boundary Element Method

CFRP

Carbon Fiber Reinforced Polymer

CLEC

Complete Linear Expansion Case

CUF

Carrera Unified Formulation

CWT

Continuous Wavelet Transform

DSNE

Design Specification for Natural Environments

DWT

Discrete Wavelet Transform

EMC

Electromagnetic Compatibility

EOC

Environmental and Operational Conditions

ESL

Equivalent Single Layer

EVA

Extra Vehicular Activities

FBG

Fiber Bragg Gratings

FEM

Finite Element Method

FNs

Fundamental Nuclei

GCR

Galactic Cosmic Rays

GEL

Grid Element Length

GWs

Guided Waves

HITF

Hypervelocity Impact Technology Facility

HLE

Hierarchical Legendre Expansion

ISS

International Space Station

LRO

Lunar Reconnaissance Orbiter

LRV

Lunar Roving Vehicle

LE

Lagrange Expansion

LW

Layer-Wise

MAE

Mean Absolute Error

MEM

Meteoroid Engineering Model

MEMS

Micro-Electro-Mechanical System

MMOD

Micrometeoroid and Orbital Debris

MRD

Minimum Resolvable Distance

MSE

Mean Squared Error

NDT

Non-Destructive Testing

ODPO

Orbital Debris Program Office

PSR

Permanently Shadowed Region

PVDF

Polyvinylidene Fluoride

PVD

Principle of Virtual Displacements

PZT
Lead Zirconate Titanate

RBF
Radial Basis Function

RMS
Root Mean Square

RMSE
Root Mean Square Error

SEE
Single Event Effects

SEP
Solar Energetic Particle

SHM
Structural Health Monitoring

STFT
Short-Time Fourier Transform

SVM
Support Vector Machine

TE
Taylor Expansion

TID
Total Ionizing Dose

ToF
Time-of-Flight

UT
Ultrasonic Testing

WVD
Wigner–Ville Distribution

Chapter 1

Introduction

The renewed effort to return to the Moon, within the framework of current international space exploration programs, entails the need to design pressurized rovers capable of ensuring safe mobility and habitation for astronauts in extreme environments. These vehicles must operate under unique conditions, including severe thermal excursions resulting from the lunar day–night cycle, the absence of both atmosphere and magnetic field leading to direct exposure to radiation and micrometeoroids, as well as the pervasive presence of highly abrasive lunar regolith. The combination of these factors introduces unprecedented design challenges from structural, thermal and operational perspectives.

A pressurized rover must withstand internal pressurization loads, localized impacts and the cumulative effects of fatigue cycles, while maintaining low mass and high reliability. Protection against micrometeoroid impacts (MMOD shielding) and radiation mitigation are additional critical requirements. At the same time, it is crucial to develop structural health monitoring (SHM) solutions capable of detecting damage and degradation at an early stage, thereby enhancing vehicle safety and extending its operational lifespan. In this context, innovative approaches such as Lamb wave-based techniques and the use of extremely precise sensors are gaining increasing relevance.

From a methodological standpoint, conventional finite element methods (FEM) do not always provide sufficient accuracy in modeling the behavior of laminated or multilayered structures subjected to complex and multiphysics loads. To overcome these limitations, the Carrera Unified Formulation (CUF) is introduced as a general modeling approach that enables systematic variation of model fidelity through hierarchical expansions across the thickness, while constructing the fundamental stiffness matrices in a unified manner. This framework allows for a consistent treatment of problems involving thermo-mechanical loads, impacts, discontinuities and elastic wave propagation.

1.1 Aerospace SHM: definition and relevance

Structural Health Monitoring is the set of methods that, through sensor networks, dedicated hardware and algorithms, continuously or intermittently observe the state of the structure to autonomously and effectively detect, locate and quantify damage, overcoming the limitations of periodic NDT. In aerospace, structures are lightweight, often anisotropic and layered, therefore techniques sensitive to localized defects and reliable models that take environmental and operational variability into account are required. For a pressurized lunar rover, SHM safeguards the integrity and leak-tightness of the hull, mitigates risks from micrometeoroid/orbital-debris impacts and thermo-mechanical cycling, while reducing unplanned Extra Vehicular Activities (EVAs) with benefits in safety, time and consumables. Most pressurized rover concepts feature thin composite skins and critical joints due to stress concentrations, which are well-suited to guided-wave SHM and multiscale techniques. From the state-of-the-art standpoint, Lamb waves are among the most mature for plates/shells, with high sensitivity to cracks even in complex structures with stiffeners, but they require dispersion control and nontrivial environmental compensation. Vibration-based techniques, in fact, support global monitoring but are sensitive to environmental/operational variability, whereas optical sensors such as FBGs (Fiber Bragg Gratings) offer strain and temperature measurements immune to electromagnetic interference with lightweight integration.

1.2 Lunar Surface Mobility and Pressurized Rovers: Context and Structural Challenges

Crewed lunar exploration demands engineering solutions that ensure safety, autonomy and operational continuity in an extreme environment; within this framework, pressurized rovers are the primary enabler of long-range surface mobility. This section frames the mission context and the role of pressurized rovers, synthesizing the lessons learned from the first vehicles (Apollo LRV, Lunokhod) and subsequent concepts, highlighting their strengths and limitations. In this regard, a clear distinction must be drawn between unpressurized rovers, characterized by lightness and teleoperability and pressurized ones, which serve as mobile habitats offering greater autonomy and comfort at the cost of increased complexity and mass and are therefore more suitable for medium- to long-duration missions. With respect to pressurized rovers, the cross-cutting design drivers are emphasized: modularity; energy and thermal management; micrometeoroids shielding; the abrasiveness of regolith and large thermal excursions; as well as careful attention to structural details and interfaces. The following subsections present the environment and pressurization, structural criticalities and the solutions currently employed.

1.2.1 Lunar environment

The lunar environment constitutes one of the most hostile contexts for the operation of pressurized vehicles, imposing structural and thermal-control choices aimed at ensuring integrity, leak-tightness and durability under extreme conditions. The combination of cratered morphology, fine and porous regolith, a plasma/-electrostatic environment, severe thermal cycles, radiation and micrometeoroid fluxes defines the loads and the design criteria for thin panels, joints, windows and feedthroughs, guiding both material selection and the adoption of multilayer shields and in-situ monitoring strategies. In this regard, NASA's *Design Specification for Natural Environments* (DSNE, 2019) summarizes requirements and guidelines drawn from operational experience and the technical literature, providing reference environmental parameters, design criteria and verification methodologies [1].

Geology and Geomorphology

The lunar surface has been shaped by billions of years of meteoritic bombardment: craters dominate the morphology and their size distribution informs the age of surfaces, with younger regions being less cratered and ancient areas approaching saturation for microcraters, as described by Wilhelms [2] and by Neukum and Ivanov [3]. From a structural standpoint, irregular terrains and localized elevation changes demand careful attention to stability (risk of rollover), impact loads and stress concentrations during traversal, all of which feed fatigue phenomena at the level of frames, attachments and panels.

Regolith

Lunar regolith derives from mechanical comminution and partial melting (glasses, agglutinates) induced by impacts; Apollo samples show greater thicknesses and finer granulometry in the highlands compared to the younger basaltic maria [4], as illustrated by the grain-size distribution of Apollo 17 soil in Figure 1.1, which confirms the prevalence of fine particles ($< 100\,\mu$m). Soil density and porosity determine the response under cyclic loading, favoring stress localization and crack initiation in wheels, suspensions and frames; moreover, fine dust, which is easily mobilized, increases contamination and abrasion of joints and mechanisms, as recently studied by Gábor Kalácska and colleagues [5]. For composite materials, the low thermal conductivity of near-surface layers amplifies local gradients and through-thickness thermal mismatch between skins and cores in sandwich structures, with associated delamination risks.

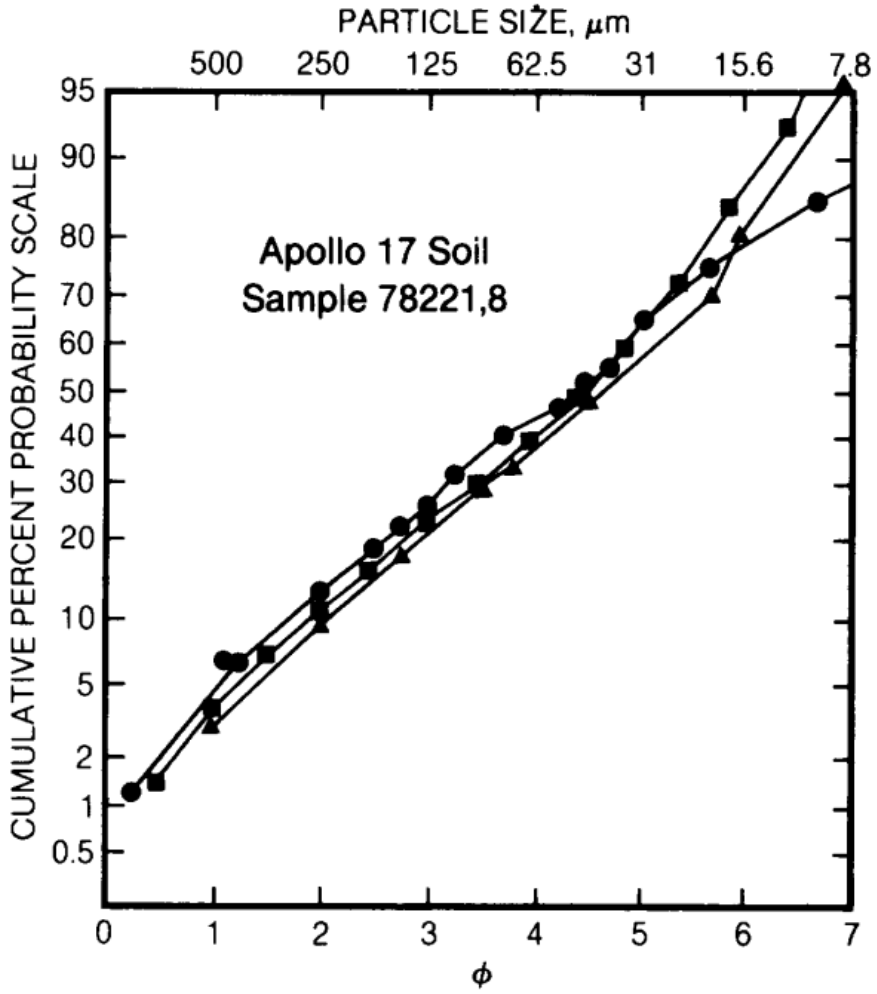

Figure 1.1: Typical grain-size distribution of lunar regolith, expressed as mass percentage by particle-size classes; representative of Apollo soils [6].

Cislunar Plasma and Electrostatic Effects

Immersed in the solar wind and lacking both a significant atmosphere and magnetosphere, the lunar surface can charge from a few up to hundreds of volts, with dynamics that are accentuated at the poles and at the terminator [7]. The levitation/settling of charged dust and wheel–regolith tribocharging aggravate deposits and discharges, especially within permanently shadowed regions where photoemission is absent; this entails requirements for conductive materials or dissipative coatings, controlled grounding paths and system-level electromagnetic compatibility (EMC) [8].

Thermal Environment and Radiation

The synodic day–night cycle (29.5 Earth days) induces extreme excursions: typically up to +120 °C during the day and down to −150 °C at night at the equator, with attenuation toward the poles but minima in permanently shadowed regions (PSR) that can fall below −230 °C. Figure 1.2 illustrates typical temperature histories over a full diurnal cycle at different latitudes, with extreme equatorial variations damping toward nearly flat profiles at 89°. Structures must tolerate cyclic thermal gradients/strains and shadow–light transients that amplify stresses near defects and interfaces; the low thermal conductivity of regolith accentuates thermal non-uniformities [9]. In radiative terms, the combination of solar wind, galactic cosmic rays (GCR) and solar energetic particle (SEP) events entails total ionizing dose (TID) and single event effects (SEE) on materials and electronics, with secondary neutron contributions from the soil; partial shielding by the terrain reduces exposure relative to free space and guides choices of placement and thicknesses, as reported by Daniel Matthiä and Thomas Berger [10].

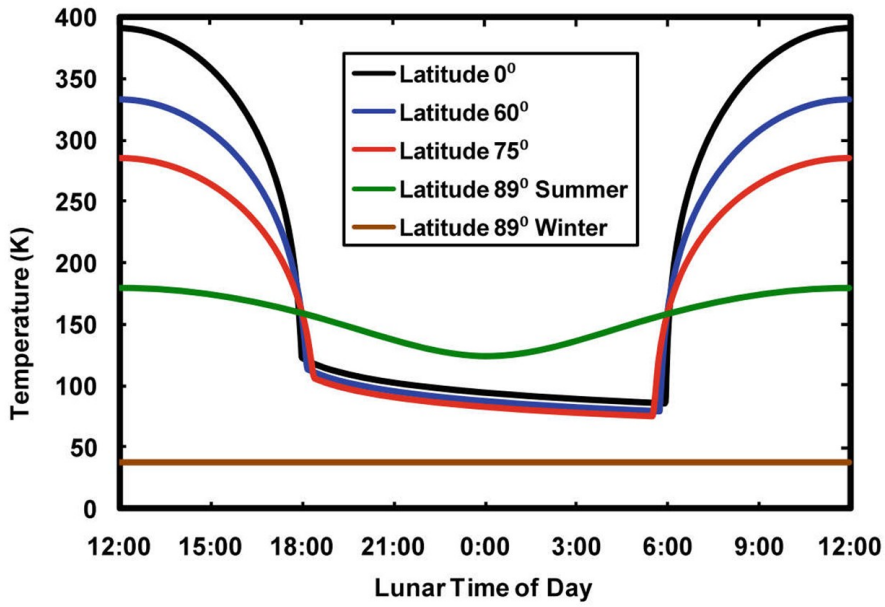

Figure 1.2: Latitudinal surface temperature excursions over one diurnal cycle derived from LRO/Diviner observations and thermophysical modeling [4].

Meteoroid Activity and Micrometeoroids

The absence of an atmosphere exposes the surface to micrometeoroid fluxes with masses ranging from fractions of milligrams to a few grams and impact velocities typically in the 13–18 km/s range, capable of generating craters, spallation and perforations; for pressurized hulls the primary risk is loss of containment. An important role in this context is played by the NASA Meteoroid Environment Office, which, in the Meteoroid Engineering Model (MEM) [11], describes approaches and modeling methods for meteoroid fluxes. Even sub-millimetric microcraters can act as crack initiators and stress concentrators, especially under thermal cycling; mitigation is achieved with Whipple or stuffed Whipple shields (fragmenting bumper, standoff, dissipative rear wall) featuring ceramic/textile layers (e.g., Nextel, Kevlar) and, at times, foams or honeycombs [12].

Neutral Exosphere and Lack of Convection

The tenuous lunar exosphere provides neither aerodynamic shielding nor convective heat exchange: impacts transfer their energy directly to the surface and thermal exchanges are radiative/ conductive, mandating dedicated external protections and robust thermal-control architectures for panels, joints and windows. This condition, combined with the factors outlined above, completes, albeit in a highly condensed and simplified form, the environmental design drivers that inform structural criteria, material selection and monitoring strategies for next-generation pressurized vehicles.

1.2.2 Structural issues of a pressurized rover

The structural integrity of a pressurized lunar rover is one of the main design challenges, as it must ensure crew safety in an extreme environment. Unlike uncrewed rovers, it must withstand a combination of loads: internal pressurization, thermal excursions and thermo-mechanical stresses, micrometeoroid and orbital debris impacts, ionizing radiation, dynamic and vibrational loads experienced both during transport and under operational conditions.

Internal pressurization

The internal pressure of the habitat represents one of the primary loads and is typically maintained between 34 and 101 kPa, for crew comfort and life support [1], with structures and materials required to withstand significant membrane stresses. The most critical areas are openings, joints and attachments, which are main sources of stress concentrations, often addressed through structural redundancy, stiffeners and multilayer solutions, as implemented in ISS modules. This approach balances safety and mobility by enabling reduced thicknesses and

the use of advanced materials such as Al-Li alloys or Carbon Fiber Reinforced Polymer (CFRP) composites. In this regard, the experience gained from years of ISS operation is fundamental, since many aspects are similar; numerous studies have sought to summarize these insights [13].

Thermal cycles and thermo-mechanical stresses

Thermal excursions induce cyclic loads that can cause thermal fatigue and progressive damage, with specific risks of delamination in composites and crack initiation in metals. Particularly critical are multi-material joints and interfaces, where rapid, heterogeneous thermal gradients exacerbate the problem. Advanced numerical tools such as Carrera Unified Formulation now enable coupled multiphysics analyses of thermo-mechanical responses in multilayer shells.

Micrometeoroid and orbital debris impacts

The lack of an atmosphere exposes the vehicle to MMOD fluxes, entailing continuous risk of erosion, crack formation and more rarely, perforation. Probabilistic estimates for long-duration missions ($\geq$ 1 year) indicate that a pressurized rover with an exposed area of 20–30 m^2 faces a non-negligible probability of being hit by particles capable of producing serious damage [14]. The structural approach distinguishes between rare but critical impact events, mitigated through passive protection systems such as Whipple shields, bumpers, rear walls and dissipative fabrics and cumulative progressive damage, whose long-term evolution is addressed through probabilistic analyses to predict structural performance over extended mission durations. Figure 1.3 shows cumulative meteoroid flux as a function of particle mass, highlighting that sub-millimeter meteoroids dominate numerically. Structurally, this implies that pressurized rovers and habitats should be engineered not only for rare catastrophic impacts, but above all for repeated exposure to high-frequency micrometeoroid "rain", which drives surface erosion, crack nucleation and progressive loss of mechanical properties.

Ionizing radiation

The lunar surface is exposed to SEP, GCR (including high-Z and energy nuclei (HZE)) and high-energy electromagnetic radiation in the UV/X/γ range [10, 15]. These fluxes cause not only radiobiological hazards for crews but also mechanical degradation, embrittlement and loss of elastic properties in materials. Current research focuses on hydrogenated polymeric and multilayer shields, composite solutions and mass optimization of the protective structures; there are numerous studies evaluating the impact of such radiation on various material classes to assess their suitability for lunar application [16, 17, 18].

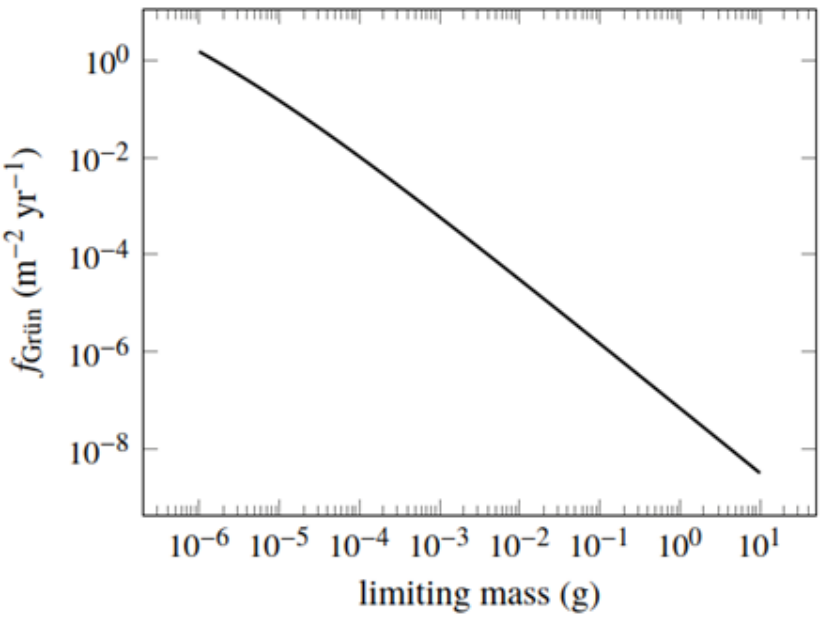

Figure 1.3: Cumulative meteoroid flux as a function of mass according to NASA's MEM 3 model [11].

Dynamic loads and vibrations

Ground-induced impacts, vibrational transients and cycles triggered by uneven terrain (in addition to the "classical" dynamic loads from launch) are key sources of structural fatigue and damage to the frame, joints and crew comfort (as also indicated by past experience [19]). Modern modeling adopts multi-degree-of-freedom dynamic models and validation with tests on regolith simulants, as in Ding et al. [20]; new suspension and damping systems, already adopted in the latest concepts (Artemis, FLEX), reduce the risk of defect accumulation and localized damage. Addressing these challenges requires advanced analysis methodologies. The CUF, for instance, allows refined modeling of the dynamic behavior of laminated and multilayered structures, naturally capturing local effects such as elastic wave propagation and sensitivity to defects or discontinuities. The integration of these numerical models with Structural Health Monitoring systems will enable real-time prediction and tracking of damage evolution during the mission, ultimately enhancing reliability and operational lifetime of the rover [21].

1.3 Materials and Known Structural Solutions

Over recent decades, research has identified advanced polymer-matrix composites for thin panels and shells; lightweight alloys such as aluminum, lithium and titanium; and protective solutions including Whipple multilayer shields, ceramic fabrics like Nextel and honeycomb sandwich structures.

The following sections provide a focused overview of candidate materials and structural solutions, illustrating their performance under typical lunar environmental stresses and referencing real applications in platforms such as the International Space Station and various pressurized rover concepts.

1.3.1 Advanced Composites

Fiber-reinforced polymer composites, mainly based on carbon or aramid fibers, are promising for pressurized lunar rovers due to their exceptional strength-to-weight ratios enabling mass reduction without compromising safety, critical for rover endurance and mobility. Structurally, multilayer anisotropic panels tailored by fiber orientation resist internal pressurization and distributed dynamic loads but require vigilance against manufacturing defects, delamination and thermo-mechanical induced crack propagation.

Advances include nanofiller or conductive fiber integration to enhance electrical conductivity and dissipate electrostatic charges induced by lunar regolith, enabling SHM via self-sensing electrical property changes linked to damage [22]. Thermal conductivity challenges of polymer matrices necessitate insulating layers or embedded conductive foils.

Applications of multilayer composites have been demonstrated in inflatable and rigid modules tested by NASA and Bigelow Aerospace, as reported in [23, 24], showing high resistance to micrometeoroid impacts through energy absorption and projectile fragmentation.

Numerically, advanced multilayer modeling with methods like CUF accurately represents delaminations and thermoelastic effects beyond classical equivalent-thickness approaches.

1.3.2 Lightweight Alloys

Widely used aerospace alloys, particularly aluminum and titanium varieties, merge high strength-to-weight ratios, excellent machinability and proven spaceflight heritage. ISS pressurized modules primarily use welded or bolted aluminum integrated with multilayer micrometeoroid shielding [14]. These alloys exhibit high fatigue strength and isotropic behavior, but thermal cycling on the lunar surface can induce significant stresses.

Limitations include vulnerability to micrometeoroid perforation without shielding and abrasion from regolith dust impacting service life. Aluminum dissipates internal heat well but is sensitive to extreme thermal cycling; titanium offers durability improvements at the cost of higher density and expense.

Designs typically combine alloys as primary load-bearing elements with multilayer composite shields to resist radiation and micrometeoroid impacts.

1.3.3 Whipple Shields

Whipple shields provide effective micrometeoroid and orbital debris protection through a modular multilayered configuration: a thin bumper fragments incoming hypervelocity projectiles into particle clouds, absorbed by spaced internal layers (spall liner, rear wall), dispersing impact energy and mitigating penetration risk.

Materials vary among aluminum, ceramic fabrics such as Nextel and aramid fibers like Kevlar, with honeycomb sandwich rear walls adding structural strength and mass efficiency.

With decades of testing at NASA's Hypervelocity Impact Technology Facility (HITF), design guidelines from the Meteoroid and Orbital Debris Program Office (ODPO) inform shield design [25, 26].

For mobile lunar rovers, Whipple shield mass and thickness trade against mobility requirements. Lunar-specific impact fluxes and frequencies necessitate tailored configurations, with hybrid shields based on aluminum, Nextel, and Kevlar showing promise, although their adaptation to lunar applications is still ongoing [14, 27].

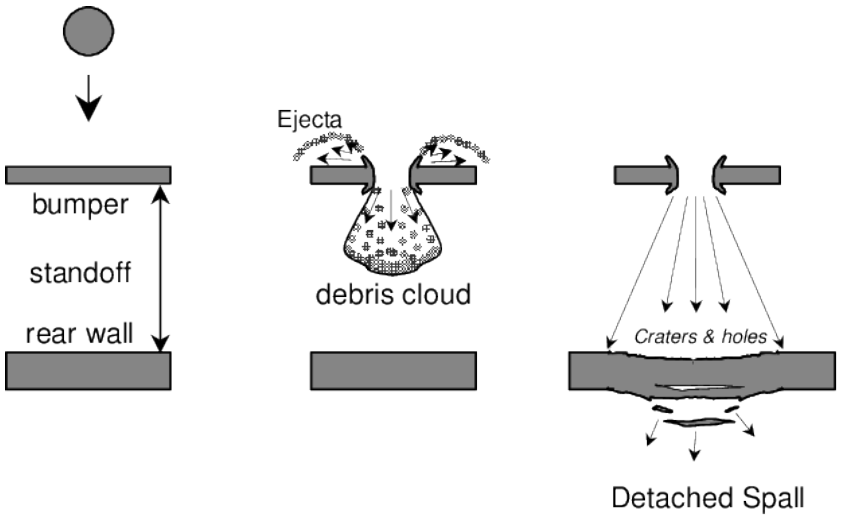

Figure 1.4: Schematic of a Whipple shield illustrating multilayer defense against hypervelocity impacts [26].

1.4 Structural Health Monitoring Techniques

SHM techniques have become indispensable in the design of complex space systems, allowing real-time assessment of structural condition through damage initiation and progression detection without direct inspections. Unlike traditional Non-Destructive Evaluation methods, SHM provides continuous, active and permanent monitoring for long-duration missions where manual maintenance is infeasible.

For pressurized lunar rovers, SHM is a key design element rather than optional. Minimizing structural safety margins and EVAs requires real-time fault detection, as undetected failures could jeopardize vehicle integrity and crew safety [28].

The lunar environment introduces additional challenges for SHM compared with terrestrial and orbital applications. These include extreme thermal cycling, which affects sensor sensitivity and calibration; the absence of atmospheric acoustic damping; exposure to electrostatic discharges caused by charged regolith; and ionizing radiation, which accelerates the aging of piezoelectric and polymer sensors and compromises long-term measurement stability. A review by Gorgin et al. also discusses several methods for properly accounting for the many factors that influence sensor measurements [29].

Varied SHM approaches tackle these issues, from passive acoustic emission sensors to vibrational methods analyzing modal frequencies, to advanced guided-wave techniques. Each has strengths and weaknesses, but all face the challenge of maintaining reliable, sensitive monitoring under harsh lunar conditions.

1.4.1 Sensor-Based Approaches for SHM: Overview of Available Solutions

One major SHM branch involves physical sensors distributed on the structure measuring mechanical or environmental parameters in real time. Widely tested in aerospace, they form the technological foundation for monitoring systems. Chief solutions include:

- **Electrical resistance strain gauges**: Direct local strain measurements with good sensitivity but require extensive wiring and suffer thermal drift.
- **Piezoelectric sensors (PZT)**: Serve as actuators and receivers, detecting vibrations and generating elastic waves for guided-wave inspections. Fragile and sensitive, they can be affected by harsh environments.
- **Fiber optic sensors (Fiber Bragg Gratings, FBG)**: Immune to electromagnetic interference, lightweight and able to cover large areas. Promising for lunar use but needs radiation-hardened readout electronics.

- **MEMS accelerometers and inertial sensors**: Capture vibration and dynamic fields; compact but with precision degrading over time and temperature.

Technological maturity, commercial availability and integration ease benefit these methods. FBG arrays and PZT actuator-receiver networks suit extended coverage and distributed detection; others excel in localized monitoring of critical or high-risk zones.

Recent research enhances diagnostic sensitivity through advanced signal processing, enabling quasi-areal monitoring and synergy with guided-wave approaches detailed later.

1.4.2 Lamb Waves for SHM of Space Structures

Lamb waves, guided elastic waves propagating in thin plates or shells, are among the most promising SHM techniques for space vehicles and pressurized rovers. They combine longitudinal and transverse motions, classified as symmetric (S0, S1, ...) or antisymmetric (A0, A1, ...) depending on displacement field symmetry relative to the laminate mid-plane [30, 31].

Lamb waves propagate over long distances with low attenuation and short wavelengths to detect millimeter-scale defects, ideal for common aerospace composite damages like delamination, cracks, or micrometeoroid impacts [32]. Their dispersive characteristics, represented via phase and group velocity curves, relate signal features to geometry and discontinuities [33].

Actuator-receiver configurations of PZT or FBG sensors enable wave packet stimulation and detection of changes post-interaction with defects. Time-frequency signal analysis combined with numerical methods reconstructs structural health "images" [34].

The lunar environment and multilayer pressurized rovers require precise predictive models. The Carrera Unified Formulation offers arbitrary accuracy numerical modeling of layered structures, efficiently simulating Lamb wave propagation considering material heterogeneity, anisotropy, thin thicknesses and defects [35, 36]. Compared to FEM, CUF uses fewer degrees of freedom while capturing dispersion and scattering, improving stability and reducing computational cost.

CUF extends naturally to multiphysical domains, incorporating mechanical, thermoelastic, piezoelectric and coupled electro-mechanical phenomena, crucial for lunar SHM under extreme thermal conditions with active sensor integration.

Integrating guided waves with CUF creates key synergy: guided waves offer defect sensitivity, CUF delivers robust simulations for complex scenarios, enabling optimized monitoring strategy design.

Chapter 2

Fundamentals of Plate Structures and CUF Theory

This chapter aims to provide a brief overview of the fundamentals of plate structures, where two in-plane dimensions prevail over the thickness direction. While numerous analogies exist with one-dimensional beam structures, the present thesis focuses exclusively on plate modeling, thus limiting the discussion to plates only.

Following the presentation of elasticity fundamentals, attention focuses on the Carrera Unified Formulation, a powerful analysis tool that overcomes the limitations of classical plate theories through hierarchical kinematics. CUF enables accurate modeling of multilayered plates with advanced through-thickness effects, forming the theoretical basis for the numerical implementations examined in this work.

For the following sections, a reference system such as the one shown in Figure 2.1 is considered.[1] The mid-surface is located at $z = 0$, while the plate thickness extends from $-h/2$ to $+h/2$. The formulations in this chapter follow [37].

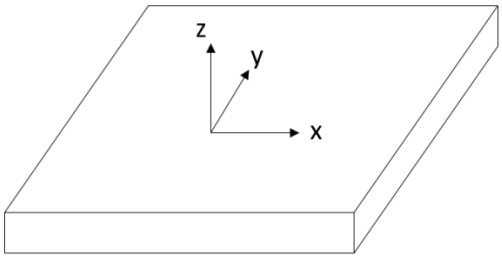

Figure 2.1: Plate reference system.

[1]The plate reference system follows the convention adopted in standard plate theories, with the mid-surface lying in the x-y plane and the thickness along the z direction.

2.1 Fundamentals of Elasticity

In order to determine the mechanical response of the plate, namely strains and, through Hooke's law, stresses, the displacement field is first introduced with respect to the previously defined reference system. The three-dimensional displacement vector is written as

$$\mathbf{u}(x,y,z;t) = \begin{Bmatrix} u(x,y,z;t) \\ v(x,y,z;t) \\ w(x,y,z;t) \end{Bmatrix}, \tag{2.1}$$

where u, v and w denote the displacement components along the x-, y- and z-directions, respectively. In the present chapter a static framework is considered and the explicit dependence on time is therefore neglected; a brief discussion on time integration schemes is provided in Section 3.3.2 and the interested reader is referred to specialized texts for a comprehensive treatment of dynamic problems.

The subsequent steps consist in considering a generic plate and identifying the general kinematic and constitutive relations between the unknown fields of the problem. A suitable plate model is then introduced by means of a set of simplifying but mechanically sound assumptions, with the aim of obtaining an algebraic system that can be solved by means of a standard finite element formulation.

According to the Principle of Virtual Work, the equilibrium of the structure requires that the virtual work of the external loads equals the virtual work of the internal stresses. In the continuous setting, the internal virtual work is defined as

$$\delta L_i = \int_V \{\sigma\} \{\delta\varepsilon\}^T \, dV, \tag{2.2}$$

where $\{\sigma\}$ and $\{\varepsilon\}$ collect the independent stress and strain components. After introducing the strain–displacement relations and the constitutive law and applying a finite element discretization of the displacement field, the external and internal virtual work take the discrete forms

$$\delta L_e = \{\delta\mathbf{S}\}^T \{\mathbf{P}\}, \tag{2.3}$$

$$\delta L_i = \{\delta\mathbf{S}\}^T [\mathbf{K}] \{\mathbf{S}\}, \tag{2.4}$$

where $[\mathbf{K}]$ is the global stiffness matrix, $\{\mathbf{P}\}$ is the vector of applied loads and $\{\mathbf{S}\}$ is the vector of generalized nodal displacements. By imposing the equilibrium condition $\delta L_e = \delta L_i$ for any admissible virtual displacement field $\{\delta\mathbf{S}\}$, the finite element equilibrium equations are obtained:

$$[\mathbf{K}] \{\mathbf{S}\} = \{\mathbf{P}\}. \tag{2.5}$$

2.1.1 Stress and Strain Tensors

Considering also Figure 2.2, the stress and strain tensors are defined as

$$\boldsymbol{\sigma} = \begin{Bmatrix} \sigma_{xx} & \sigma_{xy} & \sigma_{xz} \\ \sigma_{yx} & \sigma_{yy} & \sigma_{yz} \\ \sigma_{zx} & \sigma_{zy} & \sigma_{zz} \end{Bmatrix}, \qquad \boldsymbol{\varepsilon} = \begin{Bmatrix} \varepsilon_{xx} & \varepsilon_{xy} & \varepsilon_{xz} \\ \varepsilon_{yx} & \varepsilon_{yy} & \varepsilon_{yz} \\ \varepsilon_{zx} & \varepsilon_{zy} & \varepsilon_{zz} \end{Bmatrix}. \tag{2.6}$$

These tensors are symmetric, therefore the off-diagonal terms satisfy $\sigma_{ij} = \sigma_{ji}$ and $\varepsilon_{ij} = \varepsilon_{ji}$. As a consequence, a generic stress and strain state can be represented by column vectors containing only six independent components:

$$\boldsymbol{\sigma} = \begin{Bmatrix} \sigma_{xx} \\ \sigma_{yy} \\ \sigma_{zz} \\ \sigma_{xy} \\ \sigma_{xz} \\ \sigma_{yz} \end{Bmatrix}, \qquad \boldsymbol{\varepsilon} = \begin{Bmatrix} \varepsilon_{xx} \\ \varepsilon_{yy} \\ \varepsilon_{zz} \\ \varepsilon_{xy} \\ \varepsilon_{xz} \\ \varepsilon_{yz} \end{Bmatrix}. \tag{2.7}$$

These two vectors are usually further partitioned as follows:

$$\boldsymbol{\sigma}_n = \begin{Bmatrix} \sigma_{yy} \\ \sigma_{xy} \\ \sigma_{yz} \end{Bmatrix}, \qquad \boldsymbol{\varepsilon}_n = \begin{Bmatrix} \varepsilon_{yy} \\ \varepsilon_{xy} \\ \varepsilon_{yz} \end{Bmatrix}, \qquad \boldsymbol{\sigma}_\omega = \begin{Bmatrix} \sigma_{xx} \\ \sigma_{zz} \\ \sigma_{xz} \end{Bmatrix}, \qquad \boldsymbol{\varepsilon}_\omega = \begin{Bmatrix} \varepsilon_{xx} \\ \varepsilon_{zz} \\ \varepsilon_{xz} \end{Bmatrix}. \tag{2.8}$$

where the subscripts n and ω denote, respectively, the normal and in-plane components of the stress and strain vectors. This partition is particularly convenient in plate theories, where in-plane and transverse components often play different roles in the constitutive and equilibrium equations.

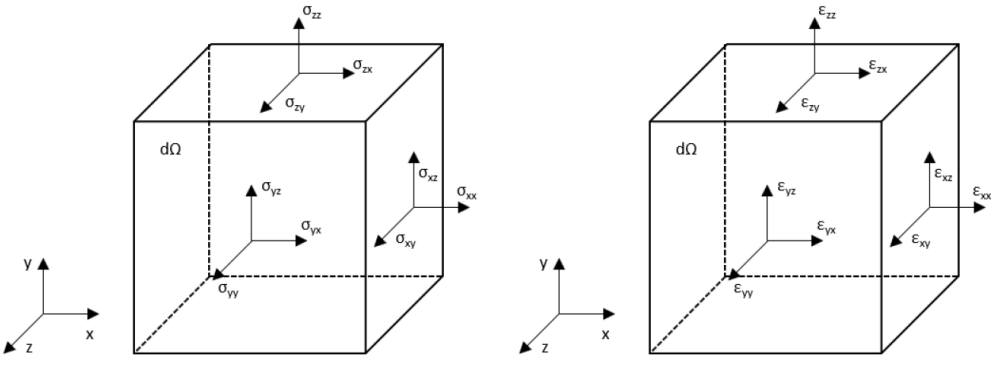

Figure 2.2: Stress and Deformation components.

2.1.2 Linear Strain-Displacement Relations

In order to simplify the problem, it is often convenient to adopt the small deformations assumption, which allows the strain components to be related linearly to the displacement field through the following relations:

$$\varepsilon_{xx} = \frac{\partial u}{\partial x}, \quad \varepsilon_{yy} = \frac{\partial v}{\partial y}, \quad \varepsilon_{zz} = \frac{\partial w}{\partial z}, \tag{2.9}$$

$$\varepsilon_{xy} = \frac{1}{2}\left(\frac{\partial u}{\partial y} + \frac{\partial v}{\partial x}\right), \quad \varepsilon_{xz} = \frac{1}{2}\left(\frac{\partial w}{\partial x} + \frac{\partial u}{\partial z}\right), \quad \varepsilon_{zy} = \frac{1}{2}\left(\frac{\partial w}{\partial y} + \frac{\partial v}{\partial z}\right). \tag{2.10}$$

This assumption neglects rigid-body rotations of finite amplitude, so that all second-order terms in the displacement gradients are ignored.

In the previous expressions, a comma followed by a subscript is used to denote partial differentiation with respect to the corresponding coordinate (for example, $u_{,x} = \partial u/\partial x$). In order to simplify the notation, it is convenient to rewrite the strain–displacement relations in matrix form. At this stage, the strain components can be expressed as

$$\boldsymbol{\varepsilon}_\Omega = D_\Omega \mathbf{u}, \qquad \boldsymbol{\varepsilon}_n = D_n \mathbf{u} = \left(D_{n\Omega} + D_{nn}\right) \mathbf{u}, \tag{2.11}$$

where D_Ω, $D_{n\Omega}$ and D_{nn} are differential operator matrices defined as

$$D_\Omega = \begin{bmatrix} 0 & 0 & \dfrac{\partial}{\partial z} \\ \dfrac{\partial}{\partial x} & 0 & 0 \\ \dfrac{\partial}{\partial z} & 0 & \dfrac{\partial}{\partial x} \end{bmatrix}, \quad D_{n\Omega} = \begin{bmatrix} 0 & \dfrac{\partial}{\partial z} & 0 \\ 0 & \dfrac{\partial}{\partial x} & 0 \\ 0 & 0 & 0 \end{bmatrix}, \quad D_{nn} = \begin{bmatrix} 0 & 0 & \dfrac{\partial}{\partial y} \\ \dfrac{\partial}{\partial y} & 0 & 0 \\ 0 & \dfrac{\partial}{\partial y} & 0 \end{bmatrix}. \tag{2.12}$$

The geometrical relations between strains and displacements can also be written in a compact vectorial form as

$$\boldsymbol{\varepsilon} = D\,\mathbf{u}, \tag{2.13}$$

where D is the global differential operator collecting all the derivatives of the displacement field:

$$D = \begin{bmatrix} 0 & \dfrac{\partial}{\partial y} & 0 \\ \dfrac{\partial}{\partial x} & 0 & 0 \\ 0 & 0 & \dfrac{\partial}{\partial z} \\ \dfrac{\partial}{\partial z} & 0 & \dfrac{\partial}{\partial x} \\ 0 & \dfrac{\partial}{\partial z} & \dfrac{\partial}{\partial y} \\ \dfrac{\partial}{\partial y} & \dfrac{\partial}{\partial x} & 0 \end{bmatrix}. \tag{2.14}$$

This compact notation is particularly useful for the derivation of the finite element formulation, since it allows the stiffness matrix to be written directly in terms of the operator D and the material constitutive matrix.

2.1.3 Constitutive Equations (Hooke's Law)

The three–dimensional Hooke's law for a generic linear elastic material can be written in compact form as

$$\{\boldsymbol{\sigma}\} = [\mathbf{C}]\{\boldsymbol{\varepsilon}\}, \tag{2.15}$$

where $[\mathbf{C}]$ is the 6×6 constitutive matrix. This relation is completely general and does not rely on any assumption about the material symmetry.[2]

For a Kirchhoff plate the transverse shear stresses are assumed to be zero, so that only the in–plane normal and shear components are retained. In this case, Hooke's law reduces to

$$\{\boldsymbol{\sigma}^*\} = [\mathbf{C}^*]\{\boldsymbol{\varepsilon}^*\}, \tag{2.16}$$

with

$$\{\boldsymbol{\sigma}^*\} = \begin{Bmatrix} \sigma_{xx} \\ \sigma_{yy} \\ \tau_{xy} \end{Bmatrix}, \qquad \{\boldsymbol{\varepsilon}^*\} = \begin{Bmatrix} \varepsilon_{xx} \\ \varepsilon_{yy} \\ \gamma_{xy} \end{Bmatrix}. \tag{2.17}$$

and the reduced constitutive matrix

$$[\mathbf{C}^*] = \begin{bmatrix} a_{11} & a_{12} & a_{31} \\ a_{21} & a_{22} & a_{32} \\ a_{61} & a_{62} & a_{66} \end{bmatrix}. \tag{2.18}$$

where the coefficients a_{ij} depend on the material properties and on the adopted ordering of the stress and strain components. In the following, the superscript $(\cdot)^*$ is used to indicate that the stress and strain vectors are written under the Kirchhoff plate assumptions.

[2]It is worth noting that the constitutive matrix $[\mathbf{C}]$ is different from the global stiffness matrix $[\mathbf{K}]$ appearing in the finite element equilibrium equations $[\mathbf{K}]\{\mathbf{S}\} = \{\mathbf{P}\}$. The former characterises the material behaviour at the continuum level, whereas the latter relates nodal displacements and nodal forces in the discretised structural model and is built by assembling the element contributions derived from $[\mathbf{C}]$.

Isotropic material

For an isotropic material, normal and shear behaviours are uncoupled: a pure shear strain does not generate normal stresses and, conversely, pure normal strains do not induce shear stresses. Moreover, the response is the same along any in–plane direction, so that

$$a_{11} = a_{22}.$$

The constitutive matrix takes the simplified form

$$[\mathbf{C}] = \begin{bmatrix} a_{11} & a_{12} & 0 \\ a_{12} & a_{11} & 0 \\ 0 & 0 & a_{66} \end{bmatrix}. \tag{2.19}$$

with

$$a_{11} = 2G + \frac{2G\nu}{1-2\nu}, \qquad a_{12} = \frac{2G\nu}{1-2\nu}, \qquad a_{66} = G. \tag{2.20}$$

where ν is the Poisson ratio and G is the shear modulus, related to the Young's modulus E by

$$G = \frac{E}{2(1+\nu)}. \tag{2.21}$$

The in–plane stress–strain relations become

$$\begin{aligned} \sigma_{xx} &= 2G\,\varepsilon_{xx} + \frac{2G\nu}{1-2\nu}\left(\varepsilon_{xx} + \varepsilon_{yy}\right), \\ \sigma_{yy} &= 2G\,\varepsilon_{yy} + \frac{2G\nu}{1-2\nu}\left(\varepsilon_{xx} + \varepsilon_{yy}\right), \\ \tau_{xy} &= G\,\gamma_{xy}. \end{aligned} \tag{2.22}$$

which correspond to a plane–stress state in the plate.

Orthotropic and anisotropic materials

In an orthotropic plate the mechanical properties along x and y are different, so that

$$a_{11} \neq a_{22}.$$

This is the typical situation for composite laminates, where the stiffness along the fibre direction can be one or two orders of magnitude larger than in the transverse direction. The degree of orthotropy is often quantified through the ratio

$$\frac{E_L}{E_T},$$

where E_L and E_T are the longitudinal and transverse Young's moduli, respectively. Large values of this ratio allow very stiff structures to be obtained in selected directions, with significant weight savings compared to isotropic metals.

For a three–dimensional orthotropic lamina, Hooke's law in the material principal directions (1,2,3) reads

$$\begin{Bmatrix} \sigma_1 \\ \sigma_2 \\ \sigma_3 \\ \tau_{23} \\ \tau_{13} \\ \tau_{12} \end{Bmatrix} = \begin{bmatrix} C_1 & C_{12} & C_{13} & 0 & 0 & 0 \\ C_{12} & C_2 & C_{23} & 0 & 0 & 0 \\ C_{13} & C_{23} & C_3 & 0 & 0 & 0 \\ 0 & 0 & 0 & C_4 & 0 & 0 \\ 0 & 0 & 0 & 0 & C_5 & 0 \\ 0 & 0 & 0 & 0 & 0 & C_6 \end{bmatrix} \begin{Bmatrix} \varepsilon_1 \\ \varepsilon_2 \\ \varepsilon_3 \\ \gamma_{23} \\ \gamma_{13} \\ \gamma_{12} \end{Bmatrix}, \tag{2.23}$$

where the coefficients C_i are functions of the engineering constants E_1, E_2, E_3, G_{12}, G_{13}, G_{23} and ν_{ij}. This law is written in the material reference system aligned with the fibres. When the lamina is rotated with respect to the global plate axes (x, y, z), a transformation based on a rotation matrix $\mathbf{T}$ is required, leading to a transformed stiffness matrix $\mathbf{Q} = \mathbf{T}\mathbf{C}\mathbf{T}^T$. In the general case, $\mathbf{Q}$ contains additional coupling terms between normal and shear components, revealing that the lamina behaves as an anisotropic material in the global reference frame.

In the context of plate theory, these distinctions between isotropic, orthotropic and fully anisotropic behaviour directly affect the form of the in–plane constitutive matrix $[\mathbf{C}]$ and, consequently, the stiffness of the structural model. For a more detailed discussion on the constitutive modelling of composite laminates and anisotropic elasticity, the interested reader is referred to classical textbooks such as *Mechanics of Composite Materials* by R. M. Jones [38].

2.2 Plate Theories

Starting from the general displacement, strain and stress fields introduced in the previous sections, plate theories are obtained by introducing specific kinematic assumptions through the thickness that reduce the number of unknowns while preserving the most relevant deformation mechanisms. Different choices of these assumptions lead to different models, with distinct ranges of validity in terms of thickness, loading conditions and material anisotropy.

Two classical formulations are briefly recalled: the Kirchhoff–Love theory, which is suitable for thin plates where transverse shear can be neglected and the Reissner–Mindlin theory, which relaxes this restriction and can be applied to moderately thick plates. These models represent the starting point and reference benchmark for the higher–order CUF plate formulations adopted in this thesis.

2.2.1 Classical Kirchhoff-Love Theory

The Kirchhoff–Love theory is widely employed in aeronautical and aerospace applications; however, its range of validity is constrained by the underlying assumptions, which can be summarised as follows:

- The plate is thin, i.e. the in–plane dimensions are much larger than the thickness, a/h, $b/h \gg 1$ (typical values of this ratio are of the order of 10^2).
- The stress components associated with the thickness direction are neglected, so that $\sigma_{zz} = \sigma_{xz} = \sigma_{yz} = 0$, in accordance with the plane–stress assumption introduced in Subsection 2.1.3.
- After deformation, lines initially normal to the mid-surface remain orthogonal to it and the plate thickness h remains constant, as illustrated in Figure 2.3. This condition leads to a vanishing normal strain, $\varepsilon_{zz} = 0$.

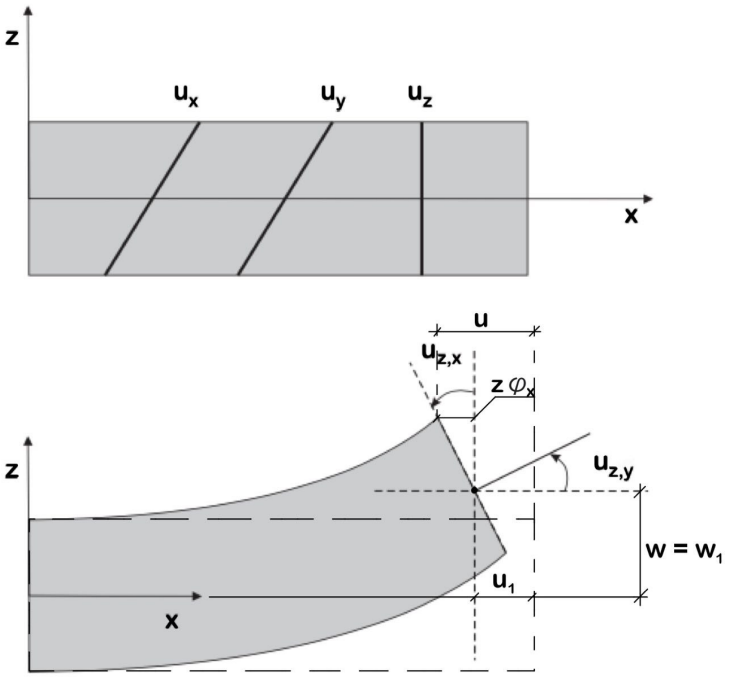

Figure 2.3: Deformation field in the Kirchhoff–Love plate theory.

Under these hypotheses, the generic displacement component can be expressed in the form

$$u(x, y, z) = u_0(x, y) + z\,\varphi(x, y), \tag{2.24}$$

which corresponds to an axiomatic choice of a linear polynomial basis through the thickness. Specialising this expression to the Kirchhoff–Love kinematics, the

displacement field can be written as

$$\begin{aligned} u(x,y,z) &= u_1(x,y) - z\,\frac{\partial w_1(x,y)}{\partial x}, \\ v(x,y,z) &= v_1(x,y) - z\,\frac{\partial w_1(x,y)}{\partial y}, \\ w(x,y,z) &= w_1(x,y). \end{aligned} \tag{2.25}$$

where u_1, v_1 and w_1 are the mid-surface displacements.

The rotations of the normal to the mid-surface about the x- and y-axes, φ_x and φ_y, are directly related to the transverse displacement as

$$\varphi_x = -\frac{\partial w_1}{\partial y}, \qquad \varphi_y = -\frac{\partial w_1}{\partial x}. \tag{2.26}$$

Considering the above assumptions and the small-strain relations, the only non-zero strain component involving the thickness coordinate is the in–plane shear strain, which can be written as

$$\varepsilon_{xy}(x,y,z) = \frac{1}{2}\left(\frac{\partial u_1}{\partial y} + \frac{\partial v_1}{\partial x}\right) - z\,\frac{\partial^2 w}{\partial x\,\partial y}. \tag{2.27}$$

Finally, by applying Hooke's law, the corresponding shear stress distribution becomes

$$\sigma_{xy}(x,y,z) = \frac{1}{2}G\left(\frac{\partial u_1}{\partial y} + \frac{\partial v_1}{\partial x}\right) - Gz\,\frac{\partial^2 w}{\partial x\,\partial y}. \tag{2.28}$$

which highlights the linear variation of σ_{xy} through the thickness predicted by the Kirchhoff–Love model.

2.2.2 Reissner-Mindlin Plate Theory

The Reissner–Mindlin theory relaxes the Kirchhoff–Love constraint that the normal to the mid-surface remains perpendicular after deformation. Independent rotations of the normal, $\varphi_x(x,y)$ and $\varphi_y(x,y)$, are therefore introduced and the displacement field becomes

$$\begin{aligned} u(x,y,z) &= u_1(x,y) + z\,\varphi_y(x,y), \\ v(x,y,z) &= v_1(x,y) - z\,\varphi_x(x,y), \\ w(x,y,z) &= w_1(x,y). \end{aligned} \tag{2.29}$$

This kinematic description allows transverse shear strains to be non-zero and

written as

$$\begin{aligned}
\varepsilon_{xy}(x,y,z) &= \frac{1}{2}\left(\frac{\partial u_1}{\partial y} + \frac{\partial v_1}{\partial x}\right) - \frac{z}{2}\left(\frac{\partial \varphi_x}{\partial y} + \frac{\partial \varphi_y}{\partial x}\right), \\
\varepsilon_{xz}(x,y,z) &= \frac{1}{2}\left(\frac{\partial w_1}{\partial x} - \varphi_x\right), \\
\varepsilon_{yz}(x,y,z) &= \frac{1}{2}\left(\frac{\partial w_1}{\partial y} - \varphi_y\right).
\end{aligned} \tag{2.30}$$

The in–plane strains retain the same structure as in the Kirchhoff–Love model, while ε_{xz} and ε_{yz} are now explicitly accounted for. Since the Reissner–Mindlin theory does not enforce the parabolic distribution of transverse shear through the thickness, a shear correction factor k is often introduced in the constitutive equations for ε_{xz} and ε_{yz} to improve accuracy, especially for moderately thick plates.

2.3 Carrera Unified Formulation

Despite the fact that solutions from classical theories still form the foundation for numerous structural analysis software packages used across various engineering sectors, the Carrera Unified Formulation addresses the simplifications inherent in these approaches while maintaining a limited computational cost [39]. Specifically, higher-order effects and physical inconsistencies such as torsion or in-plane deformations require kinematic enrichment, theoretically involving an infinite number of terms; however, increasing the number of terms escalates the complexity of both formulation and solution [40]. The CUF provides a unified framework for developing refined structural theories for beams, plates and shells through hierarchical expansions of displacement fields.

The following subsections offer a concise description of CUF theory. Readers seeking deeper insights are referred to the following texts:

- Carrera, E., *Finite Element Analysis of Structures Through Unified Formulation*, Wiley, Chichester, 2014 [39].
- Petrolo, M. (Ed.), *Advances in Predictive Models and Methodologies for Numerically Efficient Linear and Nonlinear Analysis of Composites*, Springer, Cham, 2019 [40].

2.3.1 Displacement Field in 2D CUF Models

In the CUF framework, the displacement field is expressed as a generic expansion of generalized displacements through arbitrary expansion functions. The generic

displacement is obtained as the product of two expansion functions that extend the nodal results, analogous to classical FEM methods. For two-dimensional plate models, the displacement field is given by

$$\mathbf{u}(x, y, z) = F_\tau(z)\mathbf{u}_\tau(x, y) \quad \tau = 1, 2, \ldots, M. \tag{2.31}$$

This formulation differs from beam models, as the generalized displacements $\mathbf{u}_\tau$ now depend on the plate mid-plane coordinates (x, y), while the expansion is performed through the thickness direction (z-axis).

The thickness expansion function $F_\tau(z)$ can be modelled using various bases, such as Lagrange, Taylor, or Legendre polynomials; the power of CUF lies in its unified notation (Eq. (2.33)) and the ability to associate different expansion functions to each node through the concept of fundamental nuclei, which will be briefly discussed in the following subsection. This approach provides remarkable flexibility, enabling global-local analyses and adaptive computational refinement.

The generalized displacements $\mathbf{u}_\tau(x, y)$ are interpolated using the unknown nodal displacement vector $\mathbf{q}_\tau^i$ and two-dimensional shape functions $N_i(x, y)$:

$$\mathbf{u}_\tau(x, y) = N_i(x, y)\mathbf{q}_\tau^i \quad i = 1, 2, \ldots, k. \tag{2.32}$$

Thus, the complete CUF displacement field for a plate is:

$$\mathbf{u}(x, y, z) = F_\tau(z)N_i(x, y)\mathbf{q}_\tau^i \quad \tau = 1, 2, \ldots, M \quad i = 1, 2, \ldots, k, \tag{2.33}$$

where M represents the number of expansion terms (i.e., nodes in the thickness expansion mesh) and k the number of nodes per element in the structural mesh.

Taylor Expansion Models (TE)

The Taylor Expansion (TE) model employs Taylor polynomials as the generic expansion functions $F_\tau(z)$ in the displacement field through the thickness. For a third-order expansion ($N = 3$), the basis comprises monomials up to z^3, yielding the displacement field:

$$\begin{aligned} u_x &= u_{x0} + zu_{x1}^1 + z^2u_{x2}^2 + z^3u_{x3}^3, \\ u_y &= u_{y0} + zu_{y1}^1 + z^2u_{y2}^2 + z^3u_{y3}^3, \\ u_z &= u_{z0} + zu_{z1}^1 + z^2u_{z2}^2 + z^3u_{z3}^3, \end{aligned} \tag{2.34}$$

where the superscripts denote the expansion order and u_{x0}, u_{y0}, u_{z0} represent mid-plane displacements.

The expansion order N is specified as input and can be chosen arbitrarily. Classical Kirchhoff (TE -1) and Mindlin-Reissner (TE 0) theories emerge as particular cases of first-order Taylor expansions under their respective kinematic

assumptions. Higher-order fields, such as TE1 shown in Fig. 2.4, are obtained arbitrarily at the cost of increased unknowns and computational expense.

The TE1 case, known as the Complete Linear Expansion (CLEC), enables linear variation through the thickness and accounts for ϵ_{xx}, ϵ_{zz} and γ_{xz} terms previously neglected in classical plate theories, thus capturing essential higher-order effects.

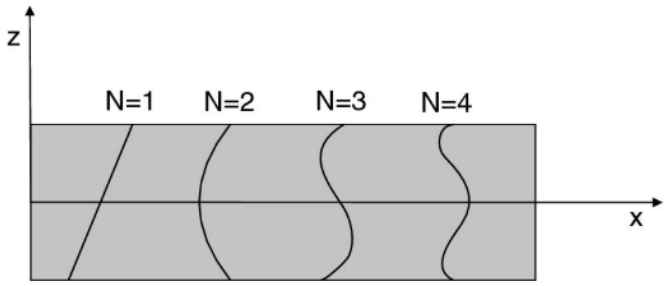

Figure 2.4: Qualitative representation of the through-the-thickness displacement field for Taylor Expansion models of increasing order N = 1,2,3,4 in the CUF framework [39].

Lagrange Polynomial Models (LE)

Lagrange Expansion models are based on Lagrange polynomials adopted as generic expansion functions $F_\tau(z)$ through the thickness in the CUF framework [39]. In contrast to Taylor polynomials, which provide a global monomial-based description of the thickness behaviour (typical of Equivalent Single Layer, ESL, approaches), Lagrange polynomials naturally lend themselves to Layer-Wise (LW) descriptions, since interpolation nodes can be placed at or within individual layers to better follow material interfaces and property jumps.

In LE models, the thickness is subdivided into one or more subdomains and within each subdomain a Lagrange interpolation of order p is introduced. Typical choices in CUF are three-node linear (L3), four-node bilinear (L4), nine-node quadratic/cubic (L9), or higher-order elements, whose nodes are distributed along the thickness according to a parent coordinate system [40]. When used in an ESL fashion, LE expansions approximate the entire laminate with a single equivalent continuum, whereas in LW formulations different sets of Lagrange functions are associated with each layer or group of layers, leading to a more detailed, though computationally more expensive, representation.

The main advantage of Lagrange-based expansions is their capability to accurately capture steep gradients and discontinuities of stresses and strains across the thickness, for instance at material or stiffness jumps in multilayered composites, without necessarily resorting to very high global polynomial orders as in TE models.

Moreover, LE models fit naturally within the finite element philosophy, since the same interpolation concept is employed both in the in-plane mesh and in the through-the-thickness expansion, thus providing an efficient and flexible tool for global–local analyses in CUF.

2.3.2 FNs, Mass Matrix and Loading Vector

As discussed in Section *Fundamentals of Elasticity*, also within the CUF framework the governing equations are derived by applying the Principle of Virtual Displacements (PVD). By adopting the CUF displacement field in the form of Eq. (2.33), the mass and stiffness matrices, as well as the load vector, can be expressed in terms of *fundamental nuclei* (FNs), whose structure is independent of the specific choice (and order) of the expansion functions.

Stiffness Matrix

In accordance with the subdivision between normal and in-plane components of the stress and strain vectors introduced in Eq. (2.8), one obtains

$$\delta L_{\text{int}} = \delta u_{sj}^{\text{T}} \, k^{\tau sij} \, u_{\tau i}, \tag{2.35}$$

where $k^{\tau sij}$ denotes the stiffness matrix written in terms of fundamental nuclei. Its explicit components can be written as follows [39]:

$$k_{xx}^{\tau sij} = Z_{pp11}^{\tau s} \int_\Omega N_{i,x} N_{j,x} \, \mathrm{d}\Omega + Z_{pp66}^{\tau s} \int_\Omega N_{i,y} N_{j,y} \, \mathrm{d}\Omega + Z_{nn55}^{\tau,z s,z} \int_\Omega N_i N_j \, \mathrm{d}\Omega, \tag{2.36}$$

$$k_{xy}^{\tau sij} = Z_{pp12}^{\tau s} \int_\Omega N_{i,y} N_{j,x} \, \mathrm{d}\Omega + Z_{pp66}^{\tau s} \int_\Omega N_{i,x} N_{j,y} \, \mathrm{d}\Omega, \tag{2.37}$$

$$k_{xz}^{\tau sij} = Z_{pn13}^{\tau,z s} \int_\Omega N_i N_{j,x} \, \mathrm{d}\Omega + Z_{nn55}^{\tau s,z} \int_\Omega N_{i,x} N_j \, \mathrm{d}\Omega, \tag{2.38}$$

$$k_{yx}^{\tau sij} = Z_{pp12}^{\tau s} \int_\Omega N_{i,x} N_{j,y} \, \mathrm{d}\Omega + Z_{pp66}^{\tau s} \int_\Omega N_{i,y} N_{j,x} \, \mathrm{d}\Omega, \tag{2.39}$$

$$k_{yy}^{\tau sij} = Z_{pp22}^{\tau s} \int_\Omega N_{i,y} N_{j,y} \, \mathrm{d}\Omega + Z_{pp66}^{\tau s} \int_\Omega N_{i,x} N_{j,x} \, \mathrm{d}\Omega + Z_{nn44}^{\tau,z s,z} \int_\Omega N_i N_j \, \mathrm{d}\Omega, \tag{2.40}$$

$$k_{yz}^{\tau sij} = Z_{pn23}^{\tau,z s} \int_\Omega N_i N_{j,y} \, \mathrm{d}\Omega + Z_{nn44}^{\tau s,z} \int_\Omega N_{i,y} N_j \, \mathrm{d}\Omega, \tag{2.41}$$

$$k_{zx}^{\tau sij} = Z_{nn55}^{\tau,z s} \int_\Omega N_i N_{j,x} \, \mathrm{d}\Omega + Z_{np13}^{\tau s,z} \int_\Omega N_{i,x} N_j \, \mathrm{d}\Omega, \tag{2.42}$$

$$k_{zy}^{\tau sij} = Z_{nn44}^{\tau,z s} \int_\Omega N_i N_{j,y} \, \mathrm{d}\Omega + Z_{np23}^{\tau s,z} \int_\Omega N_{i,y} N_j \, \mathrm{d}\Omega, \tag{2.43}$$

$$k_{zz}^{\tau sij} = Z_{nn55}^{\tau s} \int_\Omega N_{i,x} N_{j,x} \, \mathrm{d}\Omega + Z_{nn44}^{\tau s} \int_\Omega N_{i,y} N_{j,y} \, \mathrm{d}\Omega + Z_{nn33}^{\tau,z s,z} \int_\Omega N_i N_j \, \mathrm{d}\Omega. \tag{2.44}$$

where N_i and N_j are the in-plane shape functions, the subscripts (x, y, z) denote partial derivatives with respect to the in-plane coordinates and $Z_{\bullet}^{\tau s}$ are the CUF fundamental nuclei collecting the contributions of the material stiffness coefficients and thickness expansion functions.

In the figures reported in [39], the assembly procedure of the CUF stiffness matrix is illustrated by iterating over the index pairs (τ, s) and (i, j). The first pair (τ, s) refers to the expansion functions associated with the cross-section, whereas the indices i, j are related to the structural finite element mesh.

Figure 2.5 shows that, for each structural node pair (i, j), there exists a τ–s sub-matrix, which is obtained by assembling the corresponding fundamental nuclei $k^{\tau sij}$. Subsequently, the i–j sub-matrices are constructed by gathering all τ–s blocks associated with the same pair of structural nodes, as depicted in Fig. 2.6.

Finally, by assembling all the i–j sub-matrices, the global stiffness matrix $\mathbf{K}$ is obtained, as illustrated in Fig. 2.7. The resulting global matrix has dimension $(x \times x)$, where x is the total number of degrees of freedom (DOFs) of the model.

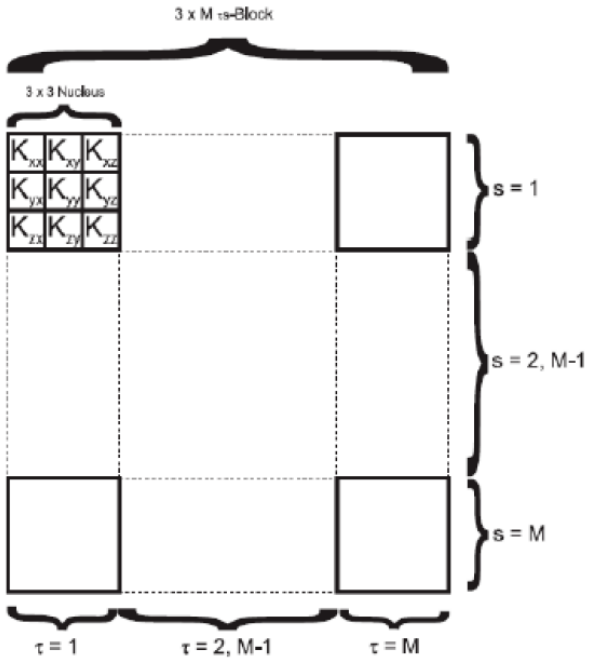

Figure 2.5: Assembly of the τ–s sub-matrix for a given pair of structural nodes (i, j) in the CUF framework [39].

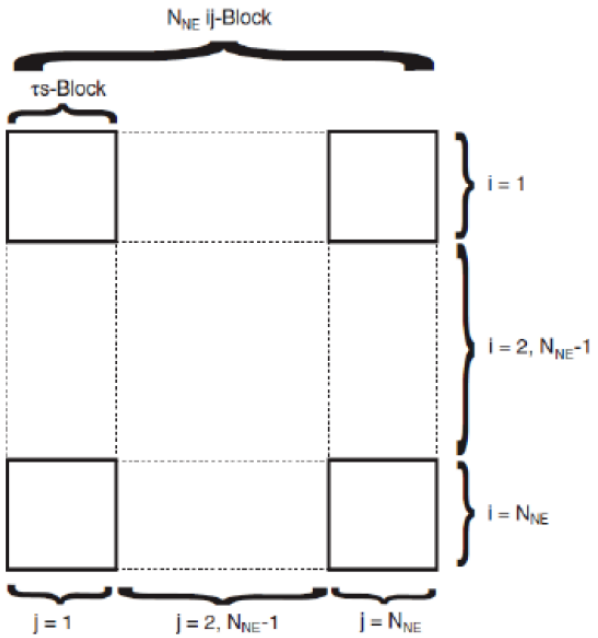

Figure 2.6: Assembly of the i–j sub-matrix by collecting all τ–s blocks associated with the same pair of structural nodes (i, j) [39].

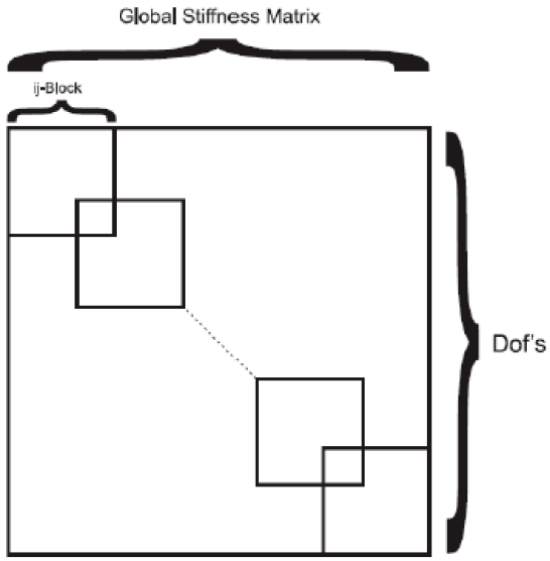

Figure 2.7: Assembly of the global stiffness matrix $\mathbf{K}$ from the set of i–j sub-matrices in the CUF formulation [39].

Mass Matrix

In order to introduce the time dependence into the CUF formulation, the virtual work of inertia must be added to the internal and external contributions. The inertial virtual work can be written as

$$\delta L_{\text{ine}} = \int_{\Omega} \delta \mathbf{u}_{sj}^{\mathrm{T}} N_j \left[\int_A (\rho \mathbf{I})\, F_\tau F_s \, \mathrm{d}z \right] N_i \, \ddot{\mathbf{u}}_{\tau i} \, \mathrm{d}\Omega, \tag{2.45}$$

where ρ is the mass density, $\ddot{\mathbf{u}}_{\tau i}$ is the nodal acceleration vector associated with the CUF generalized displacements and F_τ, F_s are the thickness expansion functions.

This expression can be conveniently rewritten in compact form by introducing the mass matrix in terms of fundamental nuclei:

$$\delta L_{\text{ine}} = \delta \mathbf{u}_{sj}^{\mathrm{T}} \, \mathbf{m}^{\tau sij} \, \ddot{\mathbf{u}}_{\tau i}, \tag{2.46}$$

where $\mathbf{m}^{\tau sij}$ denotes the CUF mass matrix in FN form. Its components are:

$$m_{xx}^{\tau sij} = m_{yy}^{\tau sij} = m_{zz}^{\tau sij} = \rho \int_A F_\tau F_s \, \mathrm{d}z \int_\Omega N_i N_j \, \mathrm{d}\Omega \tag{2.47}$$

$$m_{xy}^{\tau sij} = m_{xz}^{\tau sij} = m_{yx}^{\tau sij} = m_{yz}^{\tau sij} = m_{zx}^{\tau sij} = m_{zy}^{\tau sij} = 0 \tag{2.48}$$

By assembling the elemental contributions of the stiffness and mass matrices, the undamped free–free dynamic problem in CUF can be written at the global level as

$$\mathbf{M}\ddot{\mathbf{U}} + \mathbf{K}\mathbf{U} = \mathbf{P}, \tag{2.49}$$

where $\mathbf{U}$ is the global vector of nodal unknowns and $\mathbf{P}$ is the external loading vector. Assuming a harmonic response of the form $\mathbf{U}(t) = \mathbf{U}_i e^{\mathrm{i}\omega_i t}$, the natural frequencies ω_i can be obtained by solving the associated eigenvalue problem

$$\left(-\omega_i^2 \mathbf{M} + \mathbf{K}\right) \mathbf{U}_i = \mathbf{0}, \tag{2.50}$$

where $\mathbf{U}_i$ is the i-th eigenvector.

Consistent Load Vector

The contribution of external mechanical loads to the CUF formulation is obtained by evaluating the virtual work of the applied forces. For a generic surface load $p_\alpha(x, y)$ acting on a horizontal surface of the plate, where the index α denotes the load direction ($\alpha = x, y, z$), the virtual variation of the external work reads

$$\delta L_{\text{ext}}^{p_\alpha} = \int_\Omega \delta u_\alpha \, p_\alpha \, \mathrm{d}\Omega. \tag{2.51}$$

In the case of a concentrated nodal load, the loading vector can be written as

$$\mathbf{P} = \{ P_{u_x},\, P_{u_y},\, P_{u_z} \}^{\mathrm{T}}, \tag{2.52}$$

and the corresponding virtual work reduces to

$$\delta L_{\mathrm{ext}} = \mathbf{P}^{\mathrm{T}} \delta \mathbf{u}. \tag{2.53}$$

Within the CUF framework, the displacement field is expressed in terms of thickness expansion functions $F_\tau(z)$ and in-plane shape functions $N_i(x, y)$ (see Eq. (2.33)). Introducing this kinematic description into Eq. (2.51) for a surface load p_α applied at a generic coordinate z_p, the virtual work becomes

$$\delta L_{\mathrm{ext}}^{p_\alpha} = \int_\Omega F_s(z_p)\, N_j\, \delta u_{\alpha_{sj}}\, p_\alpha \, \mathrm{d}\Omega, \tag{2.54}$$

where $F_s(z_p)$ multiplies the in-plane interpolation to account for the actual position of the load along the thickness.

For a point load, Eq. (2.53) can be rewritten in CUF form as

$$\delta L_{\mathrm{ext}} = F_s(z_p)\, N_j(x_p, y_p)\, \mathbf{P} \delta \mathbf{u}_{sj}^{\mathrm{T}}, \tag{2.55}$$

where (x_p, y_p, z_p) denotes the load application point. This expression is directly used to construct the *consistent load vector* by associating the external force components with the corresponding generalized displacement variables $\mathbf{u}_{sj}$ to be loaded. In this way, the external actions are projected onto the CUF degrees of freedom in a manner that is fully compatible with the adopted shape and expansion functions, ensuring consistency between the load representation and the finite element interpolation.

2.3.3 Multiphysics Extensions (Hygro - Thermo - Electro - Mechanical)

The unified nature of CUF makes it particularly attractive for the analysis of multilayered smart structures subjected to combined mechanical, thermal, hygroscopic and electro-mechanical actions. In a single variational framework, CUF allows the simultaneous description of displacements, temperature, moisture content and electric potential (together with the associated fluxes and gradients), so that the relevant couplings can be captured consistently across all layers of the structure. This is essential, for example, when dealing with hybrid laminates, fibre–metal laminates or sandwich plates operating in aggressive hygrothermal environments and equipped with piezoelectric actuators or sensors.

From a continuum standpoint, the multiphysics CUF formulation relies on the standard balance laws extended to include thermal and hygroscopic fields. For each

layer, the partially coupled hygro–thermo–mechanical problem is governed by the following equations [41].

Equilibrium equations

$$\begin{aligned}
\frac{\partial \sigma_{xx}^k}{\partial x} + \frac{\partial \sigma_{xy^k}}{\partial y} + \frac{\partial \sigma_{xz^k}}{\partial z} + b_x^k = 0, \\
\frac{\partial \sigma_{xy^k}}{\partial x} + \frac{\partial \sigma_{yy^k}}{\partial y} + \frac{\partial \sigma_{yz}^k}{\partial z} + b_y^k = 0, \\
\frac{\partial \sigma_{xz^k}}{\partial x} + \frac{\partial \sigma_{yz^k}}{\partial y} + \frac{\partial \sigma_{zz^k}}{\partial z} + b_z^k = 0,
\end{aligned} \tag{2.56}$$

Heat conduction equation

$$\frac{\partial q_x^k}{\partial x} + \frac{\partial q_y^k}{\partial y} + \frac{\partial q_z^k}{\partial z} = 0. \tag{2.57}$$

Fick's second law of diffusion (steady state)

$$\frac{\partial f_x^k}{\partial x} + \frac{\partial f_y^k}{\partial y} + \frac{\partial f_z^k}{\partial z} = 0. \tag{2.58}$$

together with the hygro–thermo–elastic constitutive relations, the strain–displacement, thermal–gradient and moisture–gradient equations, as reported in detail in [41]. In this setting, stresses depend not only on mechanical strains, but also on temperature and moisture variations; conversely, heat and moisture fluxes are driven by the corresponding gradients through anisotropic conductivity and diffusivity tensors.

Although the complete multiphysics capability of CUF would require the specification of all optional thermal, hygroscopic and electro-mechanical parameters at material level, in the present work only the classical purely mechanical equations are retained and these additional couplings are not activated. As a consequence, the numerical results presented here do not aim at capturing the direct effects of temperature, moisture or piezoelectric fields, but rather provide a mechanically consistent reference framework for Lamb-wave simulations in multilayered structures.

Given the well-known sensitivity of Lamb waves to even very small variations of stiffness and mass, a more comprehensive model for future developments should fully exploit the multiphysics capabilities of CUF by consistently integrating the hygro–thermo–electro–mechanical field equations and related material parameters. In this way, the same unified formulation adopted in this thesis could be extended to investigate in detail the additional interaction mechanisms discussed in Section 3.5, *Challenges and Common Solutions*.

2.4 MUL2 Code

In this section, the *Multilayered Structures* code, which has been developed by the Mul2 research group at Politecnico di Torino on the basis of the Carrera Unified Formulation, is briefly introduced. This tool is able to investigate through-the-thickness phenomena with an accuracy that many commercial solvers cannot achieve, thus providing a reliable instrument especially suited for global–local analyses of aerospace and other advanced structures. In this thesis, the code is used in its version 11, which is driven by 11 input files with `.dat` extension from which all the data required for the analysis are read, while a recent development effort within the Mul2 group is devoted to the creation of a graphical user interface in order to make the software more user-friendly and potentially more attractive for industrial exploitation. Consequently, rather than detailing the internal implementation of the code, this subsection focuses on presenting and describing the input files employed to set up each analysis, regardless of whether the structures under investigation are plates, beams, shells, or mixed configurations.

File Analysis

The file `ANALYSIS.dat` contains some of the general and preliminary information of the simulation, such as the type of analysis to be performed (e.g. linear static analysis, free vibration analysis, dynamic analysis, thermo–mechanical analysis and so on). Each analysis type is associated in the code with an integer identifier (for example, `101` for linear static analysis, `103` for free vibration), which is specified in the first line of the file. The following line defines the solver to be used (either the full generic solver or the full ABACI solver), then the number of modes required as output for modal analyses and finally a keyword that enables or disables the shear-locking correction for beams, plates or solids. Figure 2.8 shows an example of the `ANALYSIS.dat` file, highlighting the structure of these input parameters.

ANALYSIS.dat

```
1   106              (101 for Structural Static Analysis,  102 for Structural Static with Aerodynamic
2
3   100               ( 100 = Full Generic Solver      300 = Full ABACI Solver)
4
5   30               Number of Modes for the Modal Analysis (** ATTENTION to ALL Modes choise)
6
7   NONE              Sheral locking correction beam (NONE/REDI/SELI/MITC)
8   MITC              Sheral locking correction plate (NONE/REDI/SELI/MITC)
9   NONE              Sheral locking correction solid (NONE/REDI/SELI/MITC)
10
```

Figure 2.8: Example of the `ANALYSIS.dat` input file.

File Versors

The file `VERSORS.dat` defines the local reference systems associated with each element type, so that materials with specific lay-ups can be correctly oriented with respect to the global axes. For each versor, the file lists an identifier followed by the three components of the unit vector in the global coordinate system. A common choice is to use `(1 0 0)` for plate-like elements and `(0 0 1)` for beam-like elements, as illustrated in Fig. 2.9, where an example of the `VERSORS.dat` file is reported.

VERSORS.dat

```
1

VERSOR  1         1   0   0


Usually:  1. For plate,    1    0    0
          2. For beam,     0    0    1

```

Figure 2.9: Example of the `VERSORS.dat` input file.

File Time Response

The file `TIME_RESP.dat` is required only when a dynamic analysis is performed. It specifies the parameters related to the time discretization, such as the initial and final time instants, the total number of time steps and the output frequency (i.e. how often the results are stored). In addition, this file contains the parameters that define possible time-dependent loads, including sinusoidal excitations, step loads and Lamb-type wave inputs, as shown in the example reported in Fig. 2.10.

TIME_RESP.dat

```
0.0D-4    1.0D-4    TI   TF
1000              NSTEP
50                post every
---------------------------------------
1
LAMB    100000  3   1.0    LAMB    f   n    AMPLITUDESTEP

```

Figure 2.10: Example of the `TIME_RESP.dat` input file.

File Boundary Condition

The file `BC.dat` defines the boundary conditions applied to the structure, namely kinematic constraints and external loads. Five keywords are currently available: `F-POINT`, `F-PRESS`, `D-POINT`, `D-LINE` and `D-PLANE`. With the exception of `F-PRESS`, all these entries require the geometric parameters needed to describe the point, line or plane that identifies the region where the load or constraint is applied, together with the corresponding values of forces or prescribed displacements in the three global directions. The `F-PRESS` option allows the user to apply a pressure load either on a subset of elements belonging to a given surface or on the entire face and can also be used to precisely specify the position along the thickness where the pressure is assumed to act. An example of the `BC.dat` file is shown in Fig. 2.11, where both displacement-type and force-type conditions are reported.

BC.dat

```
6

D-PLANE  1   1.0D0      0.0D0        0.0D0       0.0D0        0.0D0  0.0D0  0.0D0
D-PLANE  2   0.0D0      1.0D0        0.0D0       0.0D0        0.0D0  0.0D0  0.0D0
D-PLANE  3   1.0D0      0.0D0        0.0D0      -1.0D0        0.0D0  0.0D0  0.0D0
D-PLANE  4   0.0D0      1.0D0        0.0D0      -1.0D0        0.0D0  0.0D0  0.0D0
F-PRESS  5   ALL              1          2         1.0
F-POINT  5   0.5D0      0.50       0.005D0       0.0D0         0.0D0      1.0D0



F-PLANE  id     a,b,c,d,      fu, fv,  fw
F-POINT  id     x, y, z,      fu, fv,  fw
D-PLANE  id     a,b,c,d,      u, v,  w
D-LINE   id     x1,y1,z1,  x2,y2,z2,  u, v, w
D-POINT  id     x, y, z,      u, v,  w

```

Figure 2.11: Example of the `BC.dat` input file.

File Material

In the file `MATERIAL.dat` the mechanical properties of the materials used in the analysis are defined, for both isotropic and orthotropic behaviours. The keywords `ISO_M` and `ORT_M` are employed to specify, respectively, isotropic materials (e.g. Young's modulus, Poisson's ratio and density) and orthotropic laminas with different stiffnesses along the principal material directions. This file can also be used to introduce additional information such as damping parameters and, when required, thermal, hygroscopic and piezoelectric properties, which enable a multiphysics extension of the CUF-based model.

MATERIAL.dat

```
2   2   N_MAT = total number of materials

ORT-M   1    128.1D9  8.2D9    8.2D9   0.27    0.27  0.2     4.7D9    3.44D9    4.7D9  1570D0
ISO-M   2    2.274D9       0.36       1100.0D0


ISO-M   ID     E       v       rho
ORT-M   ID     ELL   ELZ    ELT     vLT    vLZ     vTZ        GLT    GLZ     GTZ      rho
DAMP    0.000D0   0.00D0

T-EXP   IDMAT      A1  A2  A3  A4  A5   A6
T-SPC   IDMAT      SPECIFIC_HEAT
T-CON   IDMAT      kt11 kt12   kt13   kt21   kt22  kt23  kt31    kt32  kt33

Z-EXP   IDMAT      d11 d12 d13 d14 d15 d16  d21 d22 d23 d24 d25 d26  d31 d32 d33 d34 d35 d36
Z-PRM   IDMAT      kz11 kz12   kz13   kz21   kz22  kz23  kz31    kz32  kz33

M-EXP   IDMAT      m11 m12 m13 m14 m15 m16  m21 m22 m23 m24 m25 m26  m31 m32 m33 m34 m35 m36
M-PRM   IDMAT      km11 km12   km13   km21   km22  km23  km31    km32  km33
```

Figure 2.12: Example of the `MATERIAL.dat` input file.

File Lamination

The file `LAMINATION.dat` is used to define the different laminations adopted in the analysis. Two main commands are available: `LAM2`, intended for homogeneous laminates and `LAMC`, which allows several physical layers to be compacted into an equivalent single layer. For each layer, the file specifies its thickness, fibre orientation (ply angle), associated material identifier and lamination ID, thus providing a flexible description of both simple and more complex stacking sequences.

MATERIAL.dat | LAMINATION.dat

```
3   N_LAM = total number of laminations

LAMC    1   3
1   1   2.150000D-04   0.0D0 90.0D0
2   1   2.150000D-04   0.0D0 0.0D0
3   1   2.150000D-04   0.0D0 90.0D0
LAM2   2  2   0.0D0   0.0D0
LAMC    3   3
1   1   2.150000D-04   0.0D0 90.0D0
2   1   2.150000D-04   0.0D0 45.0D0
3   1   2.150000D-04   0.0D0 -45.0D0

```

Figure 2.13: Example of the `LAMINATION.dat` input file.

File Nodes

The file `NODES.dat` lists all the nodes of the structure under investigation, together with their identifiers and spatial coordinates. For each node, the file reports the node ID, the Cartesian coordinates (x, y, z) and the through-the-thickness expansion type associated with that node, which can be chosen among Taylor (`TE`), Lagrange (`LE`) or Legendre (`HLE`) expansions.

NODES.dat

```
14641

1       0.00000000D+00      0.00000000D+00      0.00000000D+00      HLE 2
2       2.49999994D-03      0.00000000D+00      0.00000000D+00      HLE 2
3       0.00000000D+00      2.49999994D-03      0.00000000D+00      HLE 2
4       2.49999994D-03      2.49999994D-03      0.00000000D+00      HLE 2
5       4.99999989D-03      0.00000000D+00      0.00000000D+00      HLE 2
6       0.00000000D+00      4.99999989D-03      0.00000000D+00      HLE 2
7       4.99999989D-03      2.49999994D-03      0.00000000D+00      HLE 2
8       2.49999994D-03      4.99999989D-03      0.00000000D+00      HLE 2
9       4.99999989D-03      4.99999989D-03      0.00000000D+00      HLE 2
```

Figure 2.14: Example of the `NODES.dat` input file.

File Connectivity

The file `CONNECTIVITY.dat` completes the definition of the in-plane mesh by specifying the number, type and nodal connectivity of all finite elements. For each element, the file reports: the element type (e.g. `Q4`, `Q9` or `Q16`), the element ID, the ordered list of the nodes belonging to that element and, as the last entry, the identifier of the corresponding `EXP_CONN` file, which defines the through-the-thickness properties. The node numbering within each element follows a fixed convention that depends on the chosen interpolation; for `Q9` elements, this convention is illustrated in the example of Fig. 2.15, adapted from the MUL2 training material [42].

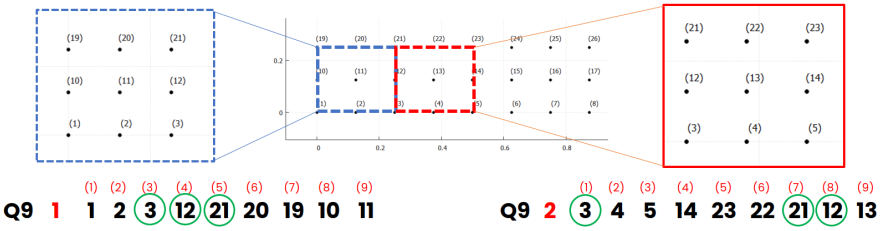

Figure 2.15: Node numbering convention for a `Q9` element, adapted from MUL2 training material [42].

CONNECTIVITY.dat

```
1600

Q16  1      1   2   5   10  12  14  20  15  13  11  6   3   4   7   9   8       1   1
Q16  2      10  16  23  34  36  38  42  32  25  20  14  12  18  27  29  22      1   1
Q16  3      34  44  57  72  74  78  82  66  53  42  38  36  47  61  63  51      1   1
Q16  4      72  89  105 122 124 130 134 114 97  82  78  74  91  108 109 94      1   1
Q16  5      122 145 167 192 195 196 202 178 153 134 130 124 149 169 171 151     1   1
Q16  6      192 215 241 270 274 278 280 254 227 202 196 195 218 247 250 219     1   2
Q16  7      270 301 332 364 366 370 376 342 311 280 278 274 303 337 338 305     1   2
Q16  8      364 401 436 472 474 479 487 446 411 376 370 366 403 439 442 407     1   2
Q16  9      472 511 557 599 603 605 607 564 526 487 479 474 517 558 562 521     1   2
Q16  10     599 641 686 735 740 741 747 702 651 607 605 603 645 688 694 647     1   2
Q16  11     735 781 834 885 889 891 897 844 796 747 741 740 783 838 842 789     1   2
```

Figure 2.16: Example of the `CONNECTIVITY.dat` input file.

File Expansion Connectivity

Regarding the through-the-thickness properties, the information required for their definition is contained in the present file and in the following one. Once the individual plies (either homogeneous or orthotropic) have been defined in `LAMINATION.dat`, different laminations can be generated by modifying the stacking sequence. In the files `EXP_CONN_*.dat`, each through-the-thickness element (of type `B2`, `B3` or `B4`) is described by its identifier, the associated ply (referenced via the lamination ID defined in `LAMINATION.dat`) and the IDs of the corresponding thickness nodes, which are then referenced in the associated file `EXP_MESH_*.dat`. Within the framework of this thesis, this file has also been used to introduce damage, by defining additional laminations with degraded material properties and assigning them only to a limited number of elements, as discussed in Subsections 4.5.1 and 4.5.2.

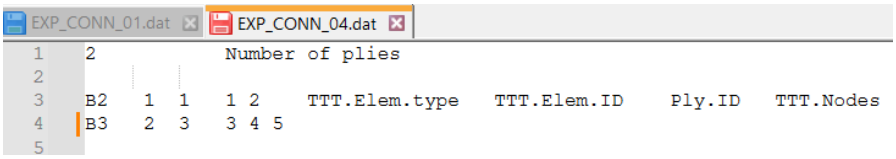

Figure 2.17: Example of the `EXP_CONN_*.dat` input file.

File Expansion Mesh

In each file `EXP_MESH_*`, the coordinates of the CUF expansion nodes along the thickness are listed for the through-the-thickness elements defined in the corresponding `EXP_CONN_*` file. In this way, the expansion mesh in the z direction is explicitly specified and consistently linked to the lamination and ply information used in the CUF model.

File Postprocessing

Finally, the file `POSTPROCESSING.dat` collects the information related to the desired output for postprocessing. It is possible to request a `.vtk` output file, which can be visualised in ParaView and is particularly suitable for three-dimensional inspection of the results. By modifying the integers that follow the `PARA 20` command, the user can control the density of the graphical output (i.e. the number of fields written to the `.vtk` file), obtaining a more or less detailed visualisation while keeping the same numerical solution and computational cost, at the expense of increased postprocessing time. Alternatively, pointwise output can be requested by specifying, for each point, an identifier and spatial coordinates using the `PNT` entries. In the case of dynamic analyses, the pointwise request returns, for every time step, the full set of quantities of interest (displacements, stresses, strains in all

components, etc.), whereas the ParaView output is generated only for those time instants that are selected through the `TIME_RESP.dat` file.

POSTPROCESSING.dat

```
3

PARA     20  GLB     2 2 1  2 2 1  2 2 2
PNT 1    0.15D0          0.2500D0  4.0700000D-03
PNT 2    1.00000D-01      0.00000D-01  -1.0D-03

```

Figure 2.18: Example of the `POSTPROCESSING.dat` input file.

Chapter 3

Lamb Waves and Simulation Methods

Following the brief introduction given in Section 1.4 *Structural Health Monitoring Techniques*, this chapter discusses the main characteristics of SHM methods based on Lamb waves, which constitute the core diagnostic tool investigated in the present thesis. The aim is not to provide an exhaustive and fully rigorous treatment of all the physical and mathematical aspects involved, but rather to frame and summarize the most relevant features for the intended applications.

Since the 1980s, a large number of scientific works have investigated guided-wave propagation in plates and shells, building on the seminal studies by Lamb in 1917 that established the theoretical foundations of the phenomenon. Among the many available contributions, the review *"Guided Lamb waves for identification of damage in composite structures: A review"* by Zhongqing Su, Lin Ye and Ye Lu [43] has been used as a primary reference and guideline for organizing the material presented in the following sections.

3.1 Lamb Wave Fundamentals

3.1.1 Key Advantages for SHM Applications

The features that make Lamb waves particularly promising and attractive as a damage detection tool can be summarized as follows:

1. Capability to inspect large structural areas, even when covered by coating and insulation systems.

2. Ability to interrogate the entire cross-section of the structure with high accuracy.

3. Use of simple, low-cost, lightweight and reliable components.

4. High sensitivity to multiple defects, with the potential for accurate multi-damage identification.

5. Low power consumption and excellent cost-effectiveness.

With increasing levels of sophistication, a Lamb-wave-based SHM system should not only detect the presence of damage qualitatively, but also localize and quantify it, enabling continuous assessment of structural health and prediction of the residual service life. However, several challenges remain, particularly those related to wave propagation speed and complex reflection patterns at structural boundaries, which can distort the scattered signals measured by sensors and tend to restrict practical analyses to relatively small regions within a larger monitored area.

3.1.2 Physical Characteristics and Dispersion

To investigate this phenomenon, it is essential to revisit the concepts introduced in Section 1.4, focusing on the fundamental characteristics of Lamb waves.

Lamb waves arise from the superposition of longitudinal and shear modes in thin plates, with propagation characteristics depending on excitation angle, frequency and structural geometry. These modes are classified as symmetric or antisymmetric, governed by the Rayleigh-Lamb characteristic equations:

$$\frac{\tan(qh)}{\tan(ph)} = -\frac{4k^2qp}{(k^2-q^2)^2} \qquad \text{for symmetric modes,} \tag{3.1}$$

$$\tan(qh) = -\frac{(k^2-q^2)^2}{4k^2qp} \qquad \text{for antisymmetric modes,} \tag{3.2}$$

where

$$p^2 = \frac{\omega^2}{c_L^2} - k^2 \qquad q^2 = \frac{\omega^2}{c_T^2} - k^2 \qquad k = \frac{\omega}{c_p}$$

with h, k, c_L, c_T, c_p, ω are the plate half-thickness, wavenumber, velocities of longitudinal and transverse modes, phase velocity and wave circular frequency, respectively.

These equations demonstrate the dispersive nature of Lamb waves, as phase velocity c_p varies with frequency for each mode, producing characteristic dispersion curves. Additionally, Love (1911) identified a transverse shear motion (SH mode) perpendicular to the propagation plane between laminate layers, distinct from vertical shear waves and confirmed by finite element simulations and experiments. This Love mode complements Lamb modes in some damage identification schemes.

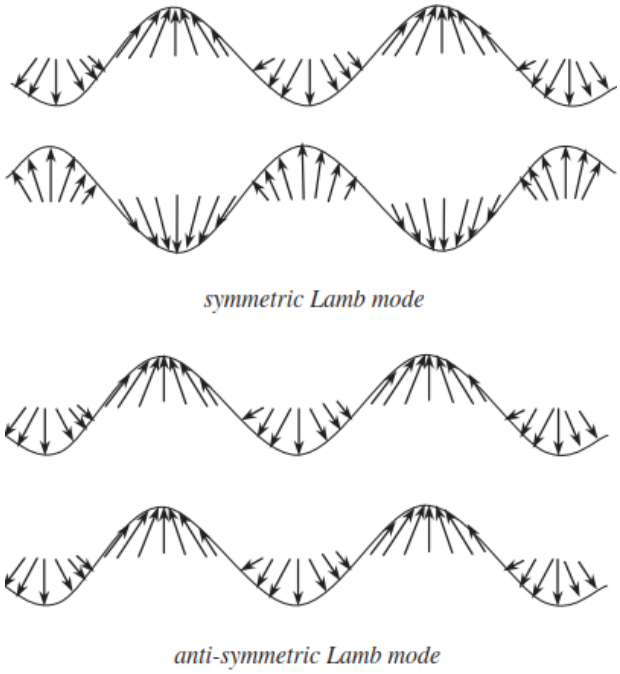

Figure 3.1: Symmetric and antisymmetric Lamb wave modes [43].

3.2 Generation and Selection of Lamb Waves

3.2.1 Excitation and Sensing Technologies

Currently, several methods based on different physical principles exist to excite the structure under examination and generate Lamb guided waves. For the sake of brevity, these approaches are summarized in Table 3.1 [43], which highlights the main advantages and drawbacks of five commonly adopted solutions. In the context of a pressurized lunar rover, where large, multilayered surfaces must be monitored with high reliability over long durations, a comprehensive SHM architecture is therefore expected to account for and possibly combine, multiple among these technologies in order to achieve adequate coverage, redundancy and robustness.

3.2.2 Mode and Excitation-Signal Selection

A proper Lamb mode for damage detection should ideally exhibit limited dispersion, low attenuation, high sensitivity to the targeted damage and practical excitability and detectability, while also allowing (at least partial) mode selectivity. In this context, it has been shown that using a narrow-band input signal helps to mitigate wave-packet spreading due to dispersion; for this reason, windowed tonebursts are often preferred over short pulses as diagnostic excitations.

Method	Advantages	Drawbacks
Bulk ultrasonic transducer (contact UT)	Mature and widely available equipment. Can excite several Lamb modes within a single measurement, enabling partial mode selection.	Non-negligible mass/volume of the probe and limited access to complex geometry. Requires access and contact (often with couplant).
Laser-based ultrasound (non-contact)	Non-contact excitation/measurement, useful for inaccessible or hot surfaces. Effective for curved surfaces or complicated geometry.	High cost and system complexity; alignment and safety constraints. Often more suitable for laboratory setups than embedded in-situ SHM.
Piezoelectric element (PZT)	Excellent performance for Lamb-wave actuation and sensing. Negligible mass/volume; easy integration; wide frequency response. Low power consumption and low cost; suitable for dense SHM networks.	Multimodal excitation is common; advanced signal processing is often required. Possible nonlinearities/hysteresis under large fields or high temperature. Brittleness, limited fatigue life and limited displacement/actuation authority.
Interdigital transducer (PVDF)	Flexible and conformable to curved surfaces. Easier handling and good dimensional stability compared to piezoceramics. Wavelength can be tuned via electrode spacing.	Weak driving force; mainly used as a sensor. As an actuator, typically effective only at low frequencies.
Optical fibre (FBG-based sensing)	Lightweight; immune to electromagnetic interference; long life. High strain resolution and potential for multiplexing/distributed sensing. Low power consumption.	Ultrasonic Lamb-wave acquisition requires dedicated high-speed interrogation. Strong directivity and sensitivity to sensor orientation. Embedded fibres can increase sensitivity but may reduce structural properties and complicate repair.

Table 3.1: Common excitation/sensing approaches for Lamb waves: main advantages and drawbacks.

For a toneburst defined by a central excitation frequency f_0 and a number of cycles n, the effective selectable frequency range $[f_{\min}, f_{\max}]$ can be related to the signal bandwidth, showing that increasing n reduces the bandwidth and therefore tends to reduce dispersion. However, when a large number of cycles is used on small coupons, different wave components (incident and reflected wave packets) can overlap in time, complicating the interpretation.

An alternative way to select a suitable frequency–cycle combination is based on the *minimum resolvable distance* (MRD) concept, where smaller MRD values indicate better spatial resolution and, consequently, more suitable excitation parameters for damage localization. In many practical cases, the fundamental modes S_0 and A_0 provide favourable trade-offs, with S_0 generally exhibiting good through-thickness sensitivity and propagation capability, while A_0 is often more sensitive to surface-related damage and can provide shorter wavelengths (hence

higher sensitivity to small defects), at the cost of higher attenuation in many configurations.

In this regard, the reader is referred to further studies [44] showing how dispersion curves can be used to identify the key parameters required for the analysis, such as the most suitable excitation frequency, the corresponding shortest wavelength in the plate and the appropriate time step and grid element length (GEL), in accordance with the guidelines reported in the following sections. An example of this procedure will, however, be briefly presented in Section 4.4.1.

Within the present thesis, Lamb-wave propagation analyses were performed using the `MUL2` software, based on the CUF. In this framework, a localized time-dependent excitation was applied to the structure in order to generate guided waves; such loading induces both S_0 and A_0 wave packets propagating along the structure at different group velocities. The applied excitation can be expressed as

$$F_{1,2}(t) = F_0 \, \sin(\omega t) \, \sin\left(\frac{\omega t}{2n}\right), \tag{3.3}$$

where $F_{1,2}(t)$ denotes the applied force (or equivalent nodal load) at the excited location(s), F_0 is the load amplitude, $\omega = 2\pi f_0$ is the angular frequency associated with the central excitation frequency f_0, t is time and n is the number of cycles that controls the duration (and therefore the bandwidth) of the toneburst. In particular, the factor $\sin(\omega t)$ defines the carrier at frequency f_0, while the multiplicative window $\sin(\omega t/2n)$ progressively turns the excitation on and off, concentrating energy around f_0 and reducing spectral leakage compared to a non-windowed sinusoid.

3.3 Modeling and Simulation

Analytical investigations of Lamb-wave dispersion are widespread in the literature. For a given frequency, the admissible wavenumbers are obtained by solving the characteristic equations, typically via iterative root-finding (e.g., Newton–Raphson) and dispersion curves can be interpreted as the loci of these roots. Common analytical frameworks include the transfer matrix (Thomson–Haskell) method and the global matrix approach. While the transfer matrix formulation can become ill-conditioned if the plate thickness (h) is large and the frequency (f) is high, the global matrix approach remains more robust, albeit sometimes with slower convergence. Approximate analytical insight can also be obtained by homogenising layered laminates through effective elastic constants.

3.3.1 Spatial Discretisation Methods

Analytical modelling of Lamb waves in composites rapidly becomes complex; therefore, numerical approaches (and in particular FEM-based simulations) have been widely developed in parallel to support dispersion analysis and, ultimately, damage identification in layered structures. Depending on the application, models ranging from simplified 1D formulations to full 3D discretisations have been proposed and alternative element types (solid, shell, strip) have been adopted to excite and capture specific wave components (e.g., symmetric/antisymmetric modes and shear-horizontal contributions). Hybrid strategies combining analytical descriptions (e.g., normal-mode expansions) with numerical models (e.g., FEM/BEM) have also been introduced to improve efficiency and to better handle phenomena such as edge reflections, mode conversion and absorbing boundary conditions.

Within this work, spatial discretisation is addressed using the CUF, which enables refined kinematic descriptions through hierarchical expansions while keeping the number of degrees of freedom under control.

Element Size Constraints and Resolution Requirements

Most studies investigating the interaction of Lamb waves with discontinuities and defects have been carried out using FEM or similar weak-form discretisations. However, ultrasonic guided-wave analyses impose strict spatial refinement constraints: the characteristic element length must be significantly smaller than the minimum wavelength to limit numerical dispersion and achieve acceptable accuracy. A commonly reported guideline is to adopt an element length-to-wavelength ratio on the order of 1/20, while a lower bound often used in practice is ~ 10 nodes per wavelength [44]. This requirement, together with the small time steps needed in transient simulations and the large monitored domains typical of SHM, can make standard FEM computationally expensive for realistic damage-detection scenarios.

Hierarchical Legendre Elements (HLE)

As shown by de Miguel, Pagani and Carrera in *"Higher-order structural theories for transient analysis of multi-mode Lamb waves with applications to damage detection"*, local beam kinematics (e.g., Taylor-type expansions) may be inconvenient when dealing with thin-walled reinforced structures characterised by corners, joints and bonded interfaces, since assembling multiple structural parts can become cumbersome and may reduce accuracy at the connections [45]. For this reason, Hierarchical Legendre Elements (HLE) are adopted in the present thesis within the CUF framework, as they provide a non-local cross-sectional representation and enable the coupling of different components while preserving displacement compatibility.

In HLE, the generalized unknowns over the cross-section are interpolated by means of hierarchical basis functions derived from Legendre polynomials, following the philosophy of the p-version of the finite element method. The one-dimensional Legendre polynomials are defined through the recursion

$$L_0 = 1, \qquad L_1 = \zeta, \qquad L_p(\zeta) = \frac{2p-1}{p}\,\zeta\,L_{p-1}(\zeta) - \frac{p-1}{p}\,L_{p-2}(\zeta), \qquad p = 2,3,\ldots \tag{3.4}$$

and the associated hierarchical interpolating functions can be built from normalized integrals as

$$\phi_p(r) = \sqrt{\frac{2p-1}{2}} \int_{-1}^{r} L_{p-1}(\zeta)\,d\zeta, \qquad p = 2,3,\ldots \tag{3.5}$$

A quadrilateral reference domain is introduced in the parametric coordinates $(r, s) \in [-1,1] \times [-1,1]$ and enriched by vertex, side and internal modes. The vertex modes coincide with standard bilinear interpolation:

$$F_\tau(r,s) = \frac{1}{4}\,(1 - r_\tau r)\,(1 - s_\tau s)\,, \qquad \tau = 1,2,3,4, \tag{3.6}$$

where (r_τ, s_τ) denote the vertex coordinates. For polynomial order $p \geq 2$, side modes are introduced so that each function is active on one side only and continuity across adjacent domains is enforced through standard C^0 assembly. For $p \geq 4$, internal modes are generated as products of 1D hierarchical functions,

$$F(r,s) = \phi_{p_1}(r)\,\phi_{p_2}(s), \qquad p_1, p_2 = 2,3,\ldots \tag{3.7}$$

This hierarchical cross-sectional discretisation makes it possible to represent complex geometries through a mesh of hierarchical sub-domains and to assemble different structural components without ad-hoc constraints. Such a feature is particularly advantageous for guided-wave analyses, since corners and joints are locations where wave reflections and mode conversions are expected and cross-sectional compatibility is essential to capture these effects reliably.

3.3.2 Time Integration Schemes

Lamb-wave-based damage identification ultimately relies on the interpretation of measured wave signals, which are often affected by practical issues such as measurement noise, interference from structural vibrations, multi-mode superposition and large data volumes. For this reason, a variety of analysis strategies are commonly adopted to extract robust damage-sensitive features, generally grouped into time-domain, frequency-domain and combined time–frequency approaches.

- **Time-domain analysis:** it works directly on the recorded waveform (e.g., time-of-flight, residual signals with respect to a baseline), offering an intuitive link to damage localization; however, it may struggle to isolate defect-scattered information when noise affects specific frequency bands and it typically requires a reference (baseline) signal for comparison.
- **Frequency-domain analysis:** it examines how the signal energy is distributed in frequency (e.g., via Fourier-based methods), which is useful for separating contributions associated with different modes and for identifying dominant frequency content; nevertheless, purely frequency-based views may lose temporal information and, in some cases, require dense spatial sampling to achieve explicit mode separation.
- **Time–frequency analysis:** it combines temporal and spectral information to better handle non-stationary wave packets, enabling the identification of transient features that may be hidden in either domain alone.
  - **STFT:** applies a Fourier analysis over a moving time window, providing a practical compromise between time and frequency resolution, but limited by the fixed window size.
  - **WVD (and variants):** can provide higher resolution than STFT, but it is typically more sensitive to sampling requirements and may introduce artifacts when applied to raw signals.
  - **Wavelet Transform (CWT/DWT):** uses localized waveforms to represent the signal at multiple scales, supporting visualization of dispersive wave packets and effective denoising/feature extraction, at the cost of increased computational effort (especially for continuous forms).

Newmark Method and Time Step Constraints

In transient dynamic analyses, the governing equations must be discretized in time. In Lamb-wave-based SHM simulations, the very short wave periods typically require extremely small time steps; for this reason, explicit time-integration schemes are often adopted together with mass-lumping strategies, although they remain conditionally stable and thus impose strict constraints on Δt.

Since the CUF is frequently employed to compare different structural theories (and this aspect is also addressed in the present thesis) it is not always possible (nor convenient) to diagonalize the mass matrix in a consistent manner across all the considered models. Consequently, the computational advantages typically associated with explicit time-integration schemes would be reduced. For this reason, the time-integration strategy implemented in the present CUF framework is the implicit Newmark method.

Accordingly, the update relations at time $t + \Delta t$ are:

$$\dot{U}_{t+\Delta t} = \dot{U}_t + \left[(1-\gamma)\ddot{U}_t + \gamma\ddot{U}_{t+\Delta t}\right]\Delta t, \tag{3.8}$$

$$U_{t+\Delta t} = U_t + \dot{U}_t\Delta t + \left[\left(\frac{1}{2}-\beta\right)\ddot{U}_t + \beta\ddot{U}_{t+\Delta t}\right]\Delta t^2, \tag{3.9}$$

where Δt is the time increment and γ and β are parameters controlling stability and accuracy.

Although the refined temporal discretization required by Lamb-wave problems can make implicit solvers computationally demanding, in linear analyses the system matrices remain constant over time. This allows the dynamic stiffness matrix to be factorized only once at the beginning of the simulation and reused at each time step, reducing the overall computational cost.

Nevertheless, an accurate time discretization remains essential to resolve the highest frequency content of the propagating guided waves. As affirmed by Moser *et al.* in *"Modeling elastic wave propagation in waveguides with the finite element method"*, for the Newmark time integration scheme an effective compromise is to adopt *20 points per cycle* of the highest frequency of interest, which provides accurate solutions in an efficient manner [46]. This guideline can be expressed as:

$$\Delta t \approx \frac{1}{20 f_{\max}}, \tag{3.10}$$

where $f_{\max}$ denotes the highest frequency of interest.

3.4 Damage Identification Methods

Damage identification strategies based on Lamb waves can be broadly grouped into *direct* and *inverse* approaches. Direct methods aim at detecting and, in simple cases, localizing damage by extracting damage-sensitive indicators directly from the measured signals (often through comparison with a baseline condition). Their main advantages are simplicity, limited computational cost and suitability for rapid screening; however, their accuracy can be affected by operational and environmental variability and they often require reference data for a reliable comparison.

Inverse methods, instead, formulate damage identification as a reconstruction problem: the goal is to infer the damage location and/or severity by matching measurements to a model (physics-based, data-driven, or hybrid). These approaches are typically more appropriate for complex configurations (e.g., multilayered structures, complex geometries, multi-damage scenarios) because they can integrate more information and constraints, but they generally require higher computational effort, stronger modelling assumptions, or larger datasets.

Remark: For further details on the methods introduced in this section (including recent algorithmic developments, experimental validations and technology-demonstration projects) the interested reader is referred to the numerous papers and research projects available in the open literature [32, 34].

3.4.1 Direct Algorithm

A representative direct strategy is based on *Time-of-Flight* (ToF) variations. In a pitch–catch configuration, an actuator generates a guided-wave packet and a sensor records the arrival time of a selected wave feature (e.g., the first threshold crossing, the envelope peak, or a correlation peak). The presence of damage along the propagation path may alter the effective travel time, due to scattering, mode conversion, or changes in the effective propagation velocity, enabling both detection and a first-order localization.

Besides ToF, other signal characteristics can also vary as a consequence of defect-induced scattering, most notably the *amplitude* (and, more generally, energy-related measures) of the received wave packet. In the direct-approach framework, deviations from a baseline (healthy) measurement are therefore exploited to obtain information (with different levels of simplicity and reliability) about the damage location and its extent. In this simplified description, such baseline changes are interpreted assuming unchanged operational and environmental conditions, i.e., neglecting additional variability that may otherwise produce similar signal variations even in the absence of damage.

3.4.2 Inverse Algorithm

Inverse approaches are generally better suited to complex problems, where a simple damage index is not sufficient to achieve reliable localization or quantitative assessment. In this setting, damage parameters (e.g., position, size, stiffness reduction) are treated as unknowns and are estimated by minimizing the mismatch between measured and predicted signals, or by solving a reconstruction problem using multiple sensing paths. The main strength of inverse methods is their potential to provide quantitative information (not only 'damage/no damage'), while the main limitation is the increased complexity in terms of modelling, computation and validation.

Artificial Intelligence

Artificial intelligence (AI) techniques represent one of the most promising families of inverse methods, especially in light of the rapid development of sensing hardware and computational resources. In Lamb-wave SHM, AI can be used to perform

classification (damage type), regression (damage location or severity), or anomaly detection (departure from normal conditions) by learning patterns directly from the measured signals or from features extracted in time, frequency, or time–frequency domains. Once trained, AI-based approaches can be extremely fast in inference and can handle complex, multi-parameter relationships; however, they usually require representative datasets for training and careful strategies to ensure robustness to operational variability.

3.4.3 Sensor Network Technology

Independent of the selected identification algorithm, the availability of a suitable sensor network is a key enabling factor for reliable SHM. Distributed actuator–sensor layouts increase spatial coverage, redundancy and the number of available propagation paths, thereby improving damage detectability and localization capability. Moreover, a sensor network naturally enables *tomographic* concepts: by combining information from multiple paths that cross the inspected area, it becomes possible to reconstruct a damage-related map (or probability field) over a large region rather than relying on a single measurement path. This aspect is particularly relevant for large and complex structures, where the objective is not only to detect damage but also to constrain its location within an extended monitored surface.

3.5 Challenges and Common Solutions

Despite the fact that guided waves represent a powerful and highly promising tool for SHM, significant obstacles, investigated by an extensive body of research, must be fully addressed before reaching mature and reliable solutions suitable for complex systems such as a pressurized lunar rover. Beyond the already discussed aspects (namely the strong dispersive behaviour of GWs, their multi-modal nature and boundary reflections that complicate feature extraction and damage localization) additional major limitations include the computational cost of high-fidelity simulations and, most importantly, the pronounced sensitivity of Lamb-wave responses to environmental and operational variability. Furthermore, practical constraints related to the employed sensors and hardware (e.g., installation, durability, stability and long-term reliability) still represent a key barrier to large-scale real-world deployment.

Nevertheless, substantial progress has been achieved in all these directions and numerous studies investigate these challenges individually and, increasingly, in a combined manner, thereby improving the current understanding of the phenomenon and proposing mitigation strategies. In the following subsection, with reference to *"Environmental and operational conditions effects on Lamb wave based structural*

health monitoring systems: A review" by Rahim Gorgin, Ying Luo and Zhanjun Wu [29], the main concepts currently established in this context are briefly outlined.

3.5.1 Environmental and operational conditions effects

Despite the fact that these effects have not been explicitly accounted for in the present study, it is worth emphasizing once again that the multiphysics extensions of the CUF framework, introduced in Section 2.3.3, can partially support the modelling of some of the phenomena associated with environmental and operational variability. Nevertheless, reliable SHM under real conditions typically requires coupling such modelling capabilities with dedicated compensation strategies and adequate computational resources.

In brief, Table 3.3 summarizes the main environmental and operational conditions affecting Lamb-wave-based SHM systems, together with commonly adopted mitigation strategies, based on [29].

EOC factor	**Main effects on Lamb-wave signals**	**Typical mitigation / solutions**
Temperature	• Time shift (TOF/group velocity changes) and amplitude variations. • Frequency-dependent behaviour; multiple mechanisms (material stiffness, thermal expansion, transducer and bond-layer properties).	• Data-driven compensation (baseline databases). • Model-driven compensation (baseline signal stretch).
Moisture (mainly composites)	• Changes in matrix-dominated properties; velocity/TOF shifts and amplitude reduction. • Risk of false indications if baselines are collected at different moisture states.	• Calibration/compensation strategies tailored to the material system. • Sensor and bonding choices to reduce long-term drift.

Vibration	• Superposition with low-frequency structural response; waveform disturbance. • TOF often less affected than amplitude in typical ranges.	• High-pass filtering; alignment/normalization; robust features.
Applied load / stress state	• Phase/time shifts (acoustoelasticity, dimensional changes); direction/path dependence.	• Compensation models; multi-path networks; separating global trends from local damage.
Bonding layer (PZT–structure adhesive) and debonding	• Strong influence on coupling: amplitude/phase/waveform changes. • Debonding reduces repeatability and measurement reliability.	• Controlled bonding process; sensor self-diagnosis; redundancy; maintainability (when feasible).

Table 3.3: Main environmental and operational conditions (EOCs) affecting Lamb-wave-based SHM and common mitigation strategies (summary adapted from [29]).

Chapter 4

Framework and Results

This chapter presents and discusses the results obtained from the different studies carried out. The analysis begins with the h/p convergence studies in static simulations and then proceeds to the identification of the most suitable model for dynamic analyses on an undamaged plate involving guided waves. It also includes the sensitivity analyses performed by varying the damage parameters in the plate and, finally, presents the results obtained by training an artificial intelligence model for damage localization.

The analyses were conducted on thin plates, either homogeneous or orthotropic, designed to reproduce in a simplified manner the external structure of the rover. The results presented were obtained through the MUL2 software, which was used to perform the numerical simulations, together with a custom MATLAB framework described in the following paragraph.

4.1 Analysis Framework

To develop a flexible system capable of managing multiple analyses such as those presented in the following sections, a dedicated *MATLAB* framework was implemented. Its main purpose is to provide a more intuitive and efficient interface with the *MUL2* software, while also automating several repetitive and optimization-related processes, both in the convergence studies and during the training phase of the predictive model. The most relevant and useful tasks implemented within the framework are summarized below:

- **Automatic acquisition of input parameters.** Through simplified interfaces, all parameters required for the generation of *MUL2* input files can be easily defined. The corresponding files are then automatically created and organized into dedicated folders for each analysis.
- **Damage generation.** The framework allows the initialization of damage features, either by varying their size at a fixed location or by changing their position randomly while keeping the size constant. This functionality facilitates sensitivity analyses and proved fundamental for the creation of the dataset provided to the artificial intelligence model.

- **Preliminary visualization of the mesh.** Functions are provided to plot both the plate stacking sequence and its layout in the x, y plane. These visualizations allow verification of the correctness of the input files, especially with regard to the mesh in the x, y plane and the laminate configuration adopted in the study.
- **Automation of analyses and data collection.** The framework manages the full execution of the analyses and automatically collects results upon completion. This automation is particularly useful when handling a large number of simulations.
- **Automatic post-processing.** The framework automatically detects whether the analysis is static or dynamic and generates the corresponding graphical outputs, such as through-thickness magnitude profiles for static cases or time-dependent plots for dynamic simulations, directly from the *MUL2* output files.
- **Convergence and damage effect evaluation.** Dedicated functions are included to compute convergence indices and generate comparative plots among multiple analyses, as well as to quantify and visualize the structural impact of damage with respect to the undamaged baseline configuration.
- **Feature extraction and AI-model development.** In a second code, denoted as `AI_CODE.m`, separated from the first one (`CODE.m`) for the sake of clarity but directly dependent on its outputs, several dedicated sections are implemented. These routines first compute key parameters, referred to as *features*, from the obtained time-domain signals and organize them into a structured dataset (`T`) to be used as input for the artificial intelligence model; then identify the most effective among these features and finally define the model providing the best predictive performance.

In addition, the analysis framework is complemented by the use of *ParaView 6.0.1*, which enables the generation of three-dimensional visualizations of the simulation results. These graphical representations are of great importance for the interpretation and understanding of the physical phenomena under investigation. The framework is also supported by the use of the *MATLAB Regression Learner App*, which provides a more effective graphical interface during the final stages of model selection, once the most suitable predictive model has been identified.

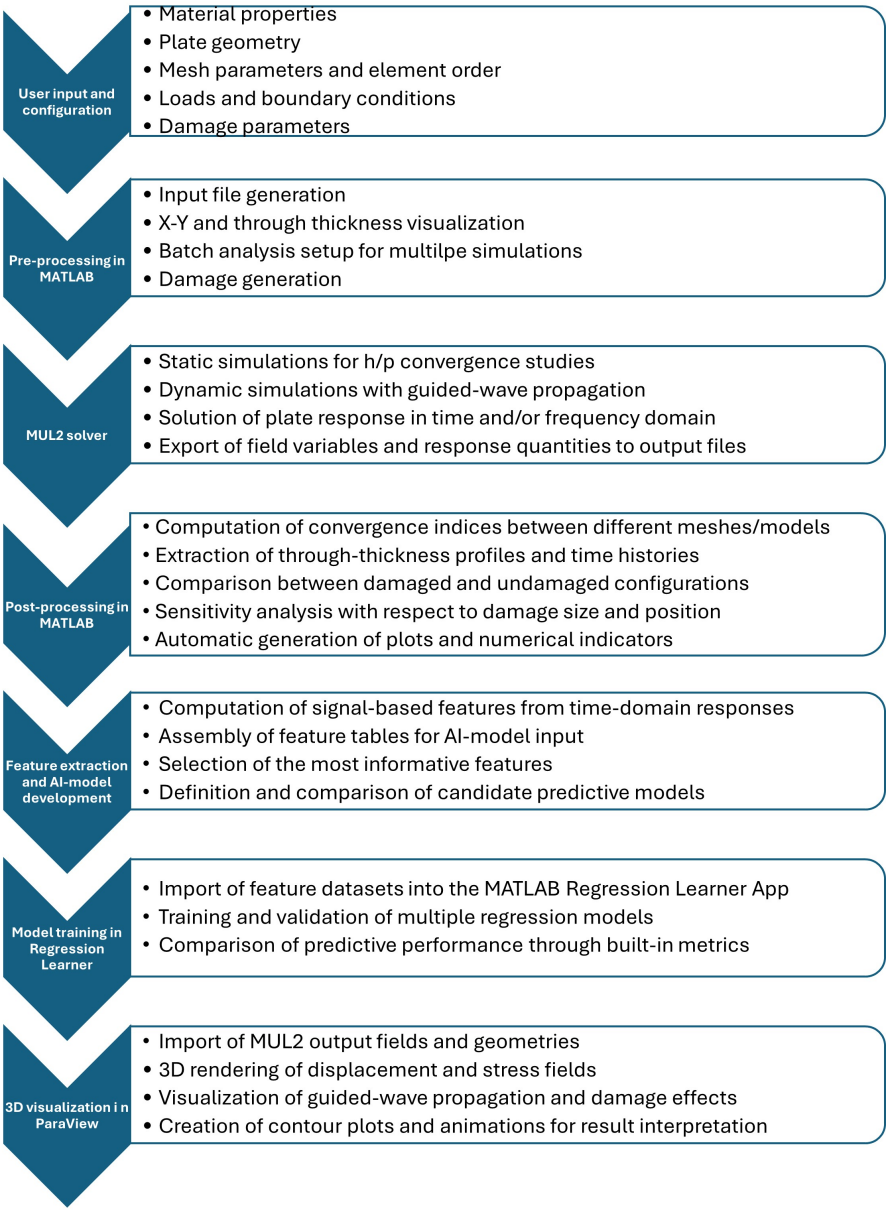

Figure 4.1: Schematic representation of the analysis framework.

4.2 Convergence with Varying Through-Thickness Expansion

As a first benchmark, the computational capability of the Carrera Unified Formulation is assessed by varying the order of the thickness expansion functions and comparing the corresponding results with those obtained by means of classical plate theories recalled in the previous chapters. Two static analyses are performed on simply supported composite plates with stacking sequence [0/90/0], which are identical in all respects except for their thickness.

The results are therefore evaluated for two plates: a thick configuration with a fixed side-to-thickness ratio $a/h = 10$ and a thin configuration with $a/h = 100$. In both cases, the in-plane mesh consists of 10×10 Q9 elements over a square plate of size $1\,\mathrm{m} \times 1\,\mathrm{m}$ and the corresponding finite element mesh and thick-plate layering scheme are shown in Figure 4.2. A uniformly distributed pressure load of $50\,000\,\mathrm{N/m^2}$ is applied on all nodes of the top surface of the plate, while the material properties adopted in the simulations are summarized in Table 4.1.

E_1	E_2 [GPa]	E_3	ν_{12}	ν_{13} [-]	ν_{23}	G_{12}	G_{13} [GPa]	G_{23}	ρ [kg/m^3]
132.38	10.76	10.76	0.24	0.24	0.49	5.65	5.65	3.61	1578

Table 4.1: Orthotropic material properties.

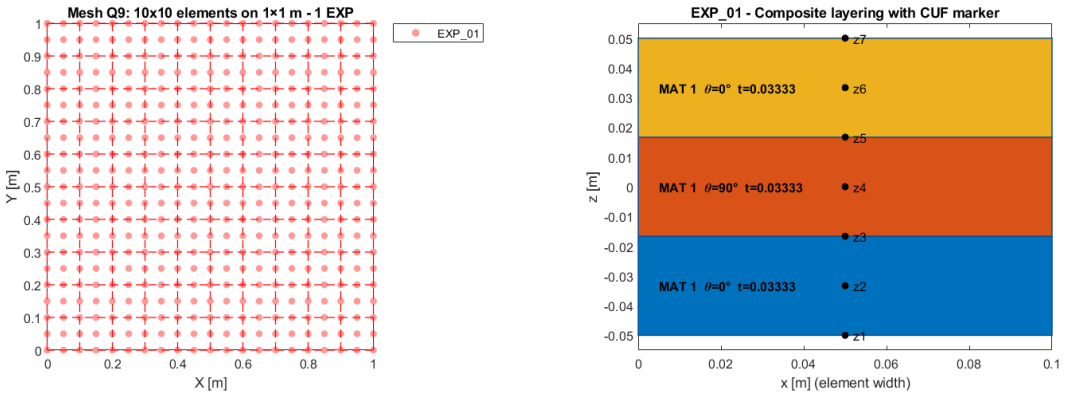

(a) **(b)**

Figure 4.2: Finite element model of the composite plate: (a) in-plane mesh with 10×10 Q9 elements over a $1\,\mathrm{m} \times 1\,\mathrm{m}$ domain; (b) through-thickness layering scheme adopted for the thick configuration.

4.2.1 Thin Composite Plate Analysis

For the thin plate analysis, the results confirm that increasing the order of the through-thickness expansion functions leads to more accurate solutions, which progressively converge towards a reference response. In particular, the TE1 model exhibits a noticeable deviation and a slightly different shape of the through-thickness profiles compared to the higher-order formulations.

For brevity, only a subset of output quantities is reported for each analysis. Figure 4.3 shows the through-thickness profiles of the transverse displacement $w(z)$, the in-plane normal stress $\sigma_{xx}(z)$ and the transverse shear stress $\sigma_{xz}(z)$, evaluated at the plate center ($x = 0.5\,\mathrm{m}$, $y = 0.5\,\mathrm{m}$), together with the corresponding plots of the relative error with respect to the most accurate solution. By assuming the second-order Lagrange expansion (LE2) as the reference solution, it can be observed that the other models, including those based on Taylor expansions, tend to converge to LE2 approximately at the fifth order for the thin plate case.

The error distribution along the thickness is defined as

$$e_k(z_j) = x_k(z_j) - x_f(z_j), \tag{4.1}$$

where $x_k(z_j)$ is the quantity computed with model k at the j-th through-thickness point and $x_f(z_j)$ is the corresponding reference value (here, the LE2 solution).

A global root-mean-square (RMS) error is then evaluated as

$$\mathrm{RMS}_k = \sqrt{\frac{1}{N}\sum_{j=1}^{N} e_k(z_j)^2}, \tag{4.2}$$

and the corresponding relative error index is defined as

$$\mathrm{RelErr}_k = \frac{\sqrt{\sum_{j=1}^{N} e_k(z_j)^2}}{\sqrt{\sum_{j=1}^{N} x_f(z_j)^2}}. \tag{4.3}$$

These indicators allow a compact quantitative comparison between different through-thickness expansion models.

Analysis	$w(z)$ [m]		$\sigma_{xx}(z)$ [Pa]		$\sigma_{xz}(z)$ [Pa]	
	RMS	RelErr	RMS	RelErr	RMS	RelErr
LE1 vs LE2	3.162×10^{-11}	5.609×10^{-10}	2.739×10^{-1}	1.206×10^{-9}	9.625×10^{-2}	2.258×10^{-7}
LE2 vs LE2	0.000×10^{0}	0.000×10^{0}	0.000×10^{0}	0.000×10^{0}	0.000×10^{0}	0.000×10^{0}
TE1 vs LE2	3.114×10^{-3}	5.523×10^{-2}	1.856×10^{7}	8.176×10^{-2}	1.105×10^{3}	2.591×10^{-3}
TE2 vs LE2	3.907×10^{-5}	6.930×10^{-4}	1.427×10^{5}	6.285×10^{-4}	3.011×10^{4}	7.062×10^{-2}
TE3 vs LE2	1.137×10^{-5}	2.016×10^{-4}	7.438×10^{4}	3.277×10^{-4}	1.284×10^{4}	3.012×10^{-2}
TE4 vs LE2	1.149×10^{-5}	2.038×10^{-4}	7.606×10^{4}	3.351×10^{-4}	1.287×10^{4}	3.020×10^{-2}
TE5 vs LE2	3.825×10^{-6}	6.784×10^{-5}	4.992×10^{4}	2.199×10^{-4}	3.740×10^{3}	8.772×10^{-3}
TE6 vs LE2	3.998×10^{-6}	7.091×10^{-5}	4.494×10^{4}	1.980×10^{-4}	3.731×10^{3}	8.751×10^{-3}
TE7 vs LE2	2.085×10^{-6}	3.697×10^{-5}	3.981×10^{4}	1.754×10^{-4}	1.882×10^{3}	4.414×10^{-3}
TE8 vs LE2	2.241×10^{-6}	3.974×10^{-5}	4.078×10^{4}	1.797×10^{-4}	1.882×10^{3}	4.415×10^{-3}

Table 4.2: RMS and relative error with respect to the LE2 reference solution for the thin composite plate (displacement w, global stresses σ_{xx} and σ_{xz}).

4.2.2 Thick Composite Plate Analysis

The main difference observed in the thick plate analysis is fully consistent with the theoretical background of the CUF and the behaviour of Taylor expansions. While Lagrange polynomials interpolate the solution at a set of points along the thickness, Taylor expansions provide a local approximation around a given point, which affects their convergence properties for thicker plates. As a consequence, the convergence of Taylor-based models is delayed in the thick plate case and the desired accuracy is reached only at higher expansion orders compared to the thin plate configuration.

For brevity, in Figure 4.4, only a subset of output quantities is reported for each analysis with the same layout adopted for the thin plate case.

Comparing the data in Tables 4.2 and 4.3, it can be observed that the relative errors obtained for the thick-plate analyses are typically 1–2 orders of magnitude larger than those computed for the thin-plate case.

Analysis	$w(z)$ [m]		$\sigma_{xx}(z)$ [Pa]		$\sigma_{xz}(z)$ [Pa]	
	RMS	ErrRel	RMS	ErrRel	RMS	ErrRel
LE1 vs LE2	0.000×10^{0}	0.000×10^{0}	0.000×10^{0}	0.000×10^{0}	0.000×10^{0}	0.000×10^{0}
LE2 vs LE2	0.000×10^{0}	0.000×10^{0}	0.000×10^{0}	0.000×10^{0}	0.000×10^{0}	0.000×10^{0}
TE1 vs LE2	5.088×10^{-6}	7.099×10^{-2}	1.902×10^{5}	8.417×10^{-2}	2.302×10^{2}	3.086×10^{-1}
TE2 vs LE2	1.698×10^{-6}	2.370×10^{-2}	3.417×10^{4}	1.512×10^{-2}	3.556×10^{1}	4.767×10^{-2}
TE3 vs LE2	6.559×10^{-7}	9.152×10^{-3}	2.017×10^{4}	8.925×10^{-3}	3.380×10^{1}	4.531×10^{-2}
TE4 vs LE2	6.544×10^{-7}	9.130×10^{-3}	2.067×10^{4}	9.144×10^{-3}	1.572×10^{1}	2.107×10^{-2}
TE5 vs LE2	2.374×10^{-7}	3.312×10^{-3}	1.215×10^{4}	5.377×10^{-3}	9.335×10^{0}	1.251×10^{-2}
TE6 vs LE2	2.378×10^{-7}	3.318×10^{-3}	1.209×10^{4}	5.349×10^{-3}	5.322×10^{0}	7.134×10^{-3}
TE7 vs LE2	1.207×10^{-7}	1.684×10^{-3}	7.334×10^{3}	3.245×10^{-3}	8.562×10^{0}	1.148×10^{-2}
TE8 vs LE2	1.210×10^{-7}	1.688×10^{-3}	7.253×10^{3}	3.209×10^{-3}	8.746×10^{0}	1.172×10^{-2}

Table 4.3: RMS and relative error with respect to the LE2 reference solution for the thick composite plate (displacement w, global stresses σ_{xx} and σ_{xz}).

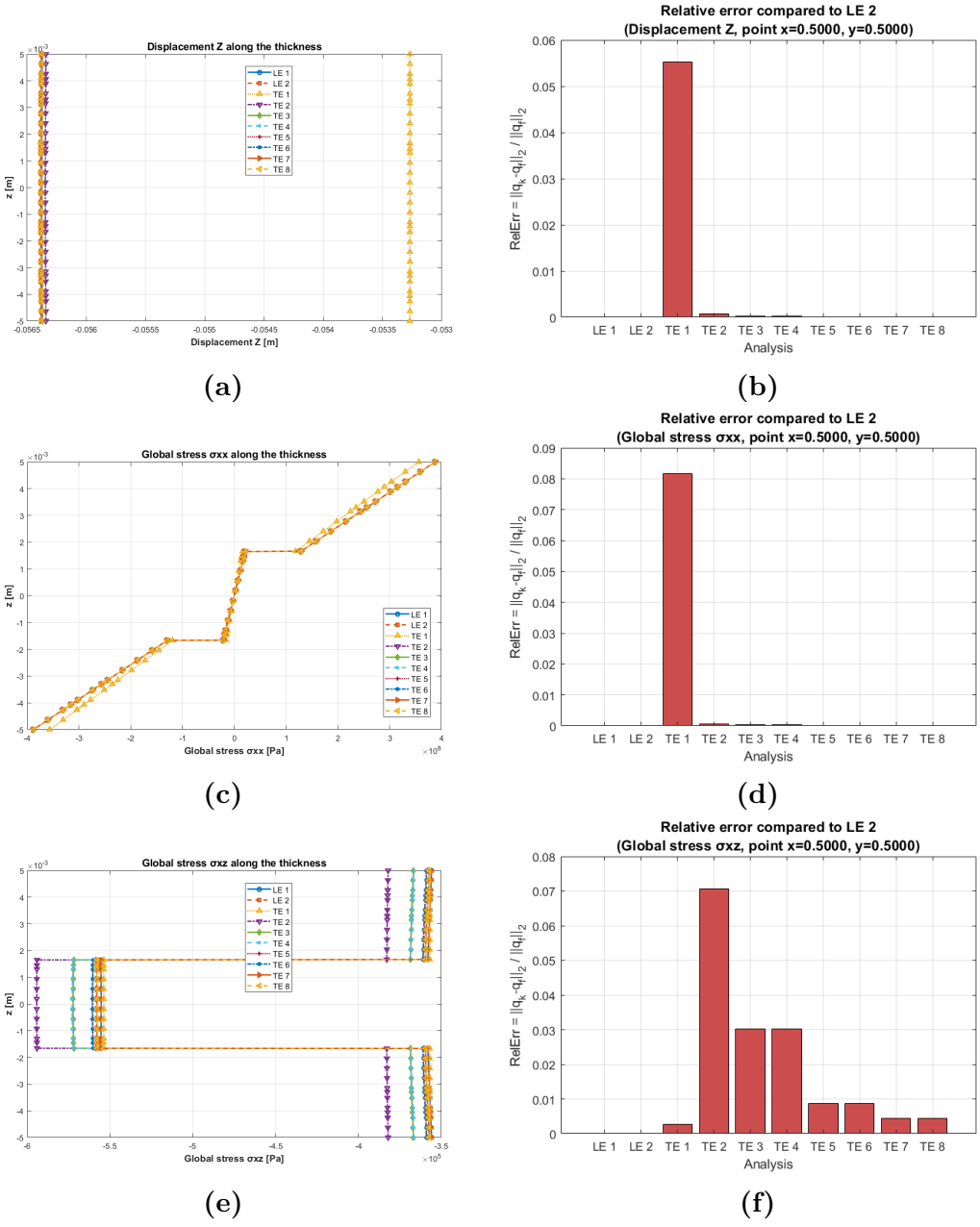

Figure 4.3: Thin composite plate: (a)–(c)–(e) through-thickness distributions of $w(z)$, $\sigma_{xx}(z)$ and $\sigma_{xz}(z)$; (b)–(d)–(f) corresponding relative error indices with respect to the LE2 reference solution.

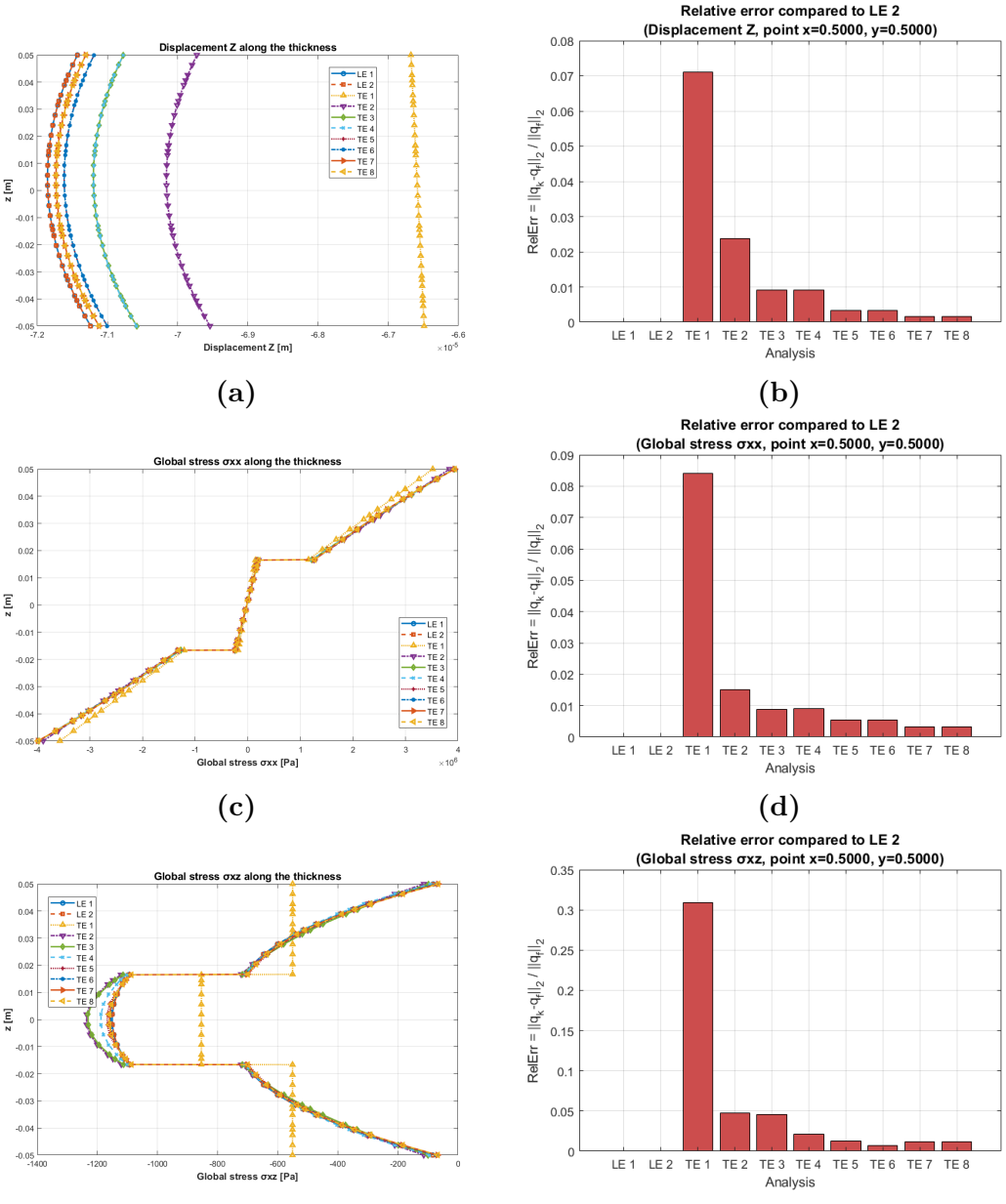

Figure 4.4: Thick composite plate: (a)–(c)–(e) through-thickness distributions of $w(z)$, $\sigma_{xx}(z)$ and $\sigma_{xz}(z)$; (b)–(d)–(f) corresponding relative error indices with respect to the LE2 reference solution.

4.3 Difference between ESL and LW Approaches

The second set of analyses aims at assessing the impact of adopting an Equivalent Single Layer approximation, by comparing it with a fully layer-wise description of the composite plate introduced in the previous subsection on the thin plate analysis. These two modelling strategies, already discussed in Subsection 2.3.2 on the CUF, are implemented in the code through the lamination commands `LAMC` (ESL) and `LAM2` (LW). Figure 4.5 highlights the differences obtained when applying the ESL simplification to the composite plate with respect to the more accurate LW solution. The comparison is restricted to Lagrange-type through-thickness expansions, since the `LAMC` command does not currently support Taylor expansions and hierarchical Legendre polynomials are implemented only for dynamic analyses.

Figure 4.5, together with the summary in Table 4.4, clearly show the significant approximations introduced by the ESL approach. Besides noticeable quantitative discrepancies, the ESL models exhibit through-thickness profiles that are qualitatively different from the LW reference solution and fail to properly capture the physical behaviour of the individual layers of the laminate.

In this case, it is also observed that increasing the expansion order within the same modelling strategy does not significantly affect the results, so that higher-order ESL solutions remain unable to recover the layer-wise reference behaviour.

Analysis	$w(z)$ [m]		$\sigma_{xx}(z)$ [Pa]		$\sigma_{xz}(z)$ [Pa]	
vs LAM2–LE2	RMS	ErrRel	RMS	ErrRel	RMS	ErrRel
LAM2–LE1	0.000×10^{0}	0.000×10^{0}	0.000×10^{0}	0.000×10^{0}	0.000×10^{0}	0.000×10^{0}
LAM2–LE2	0.000×10^{0}	0.000×10^{0}	0.000×10^{0}	0.000×10^{0}	0.000×10^{0}	0.000×10^{0}
LAMC–LE1	1.698×10^{-6}	2.370×10^{-2}	3.982×10^{5}	1.762×10^{-1}	1.991×10^{2}	2.669×10^{-1}
LAMC–LE2	1.698×10^{-6}	2.370×10^{-2}	3.982×10^{5}	1.762×10^{-1}	1.991×10^{2}	2.669×10^{-1}

Table 4.4: RMS and relative error with respect to the LAM2–LE2 reference solution for the composite plate, comparing ESL (`LAMC`) and LW (`LAM2`) models for displacement w and global stresses σ_{xx} and σ_{xz}.

It is indeed expected that, as the plate becomes thicker and the stacking sequence and material heterogeneity become more complex, the ESL approximation becomes progressively less accurate. In such cases, interlaminar stress gradients and layer-wise kinematics become more relevant, whereas an ESL model, based on thickness-averaged properties, cannot represent these effects explicitly, leading to larger discrepancies in stresses and shear-related quantities with respect to a layer-wise formulation.

Nevertheless, mixed ESL–LW strategies can be adopted in some applications, for example by employing LW descriptions only in critical regions or for selected quantities of interest while retaining an ESL model elsewhere, thus achieving a suitable balance between accuracy and computational cost.

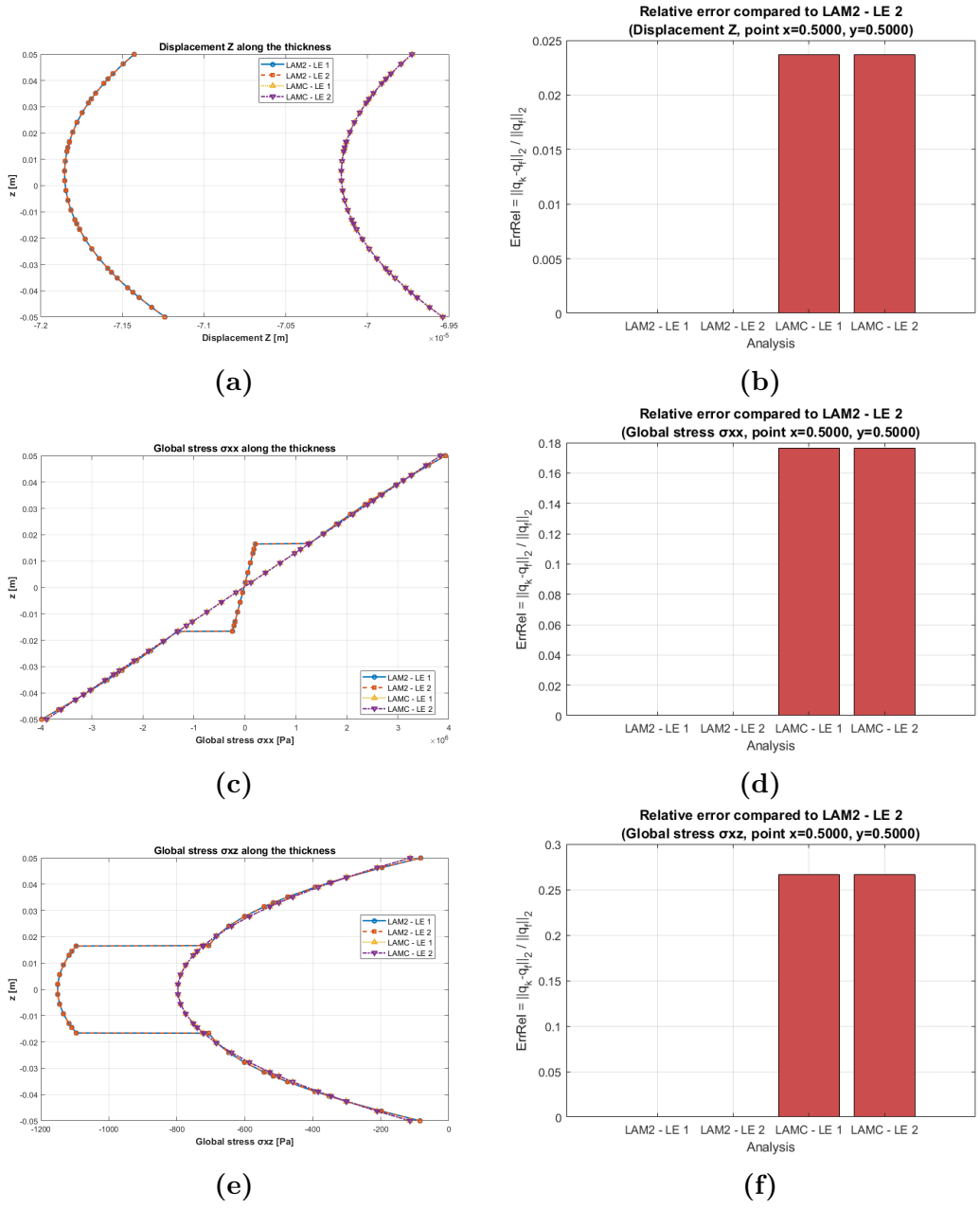

Figure 4.5: Thick composite plate: (a)–(c)–(e) through-thickness distributions of $w(z)$, $\sigma_{xx}(z)$ and $\sigma_{xz}(z)$; (b)–(d)–(f) corresponding relative error indices with respect to the LE2 reference solution.

4.4 Dynamic Convergence Assessment for Guided-Wave Propagation: Influence of In-Plane Element Type, Mesh Density and Through-Thickness Expansion Order

Dynamic analyses are now considered, with the aim of assessing how modelling choices affect the predicted guided-wave response. In particular, the sensitivity of the results to the in-plane discretisation is investigated by varying both the finite-element type (Q4, Q9 and Q16) and the mesh density and by additionally changing the order of the through-thickness expansion adopted for the hierarchical nodes. Two benchmark configurations are studied: (i) a single-excitation case, selected to promote a predominantly antisymmetric response (with prevalence of the A_0 contribution) and (ii) a dual-excitation case, where loads are applied on both the top and bottom faces to better activate the symmetric response. In these dynamic simulations, hierarchical Legendre nodes are employed, which, as discussed in Subsection 3.3.1, have proven particularly effective for problems involving guided-wave propagation.

All simulations reported in this section refer to a homogeneous isotropic plate with dimensions 0.3 m $\times$ 0.3 m $\times$ 0.002 m, simply supported along its edges (enforced on the plate mid-surface kinematics) and made of Aluminum 7075 with properties summarised in Table 4.5. At the plate centre, a five-cycle tone-burst (Lamb-type) load packet with carrier frequency $f = 50$ kHz and amplitude equal to 25 is applied, as illustrated in Figure 4.6. The resulting guided waves are monitored by means of virtual sensors located at selected positions on the plate surface, where the relevant time histories are extracted for the subsequent convergence and sensitivity assessments.

E [Pa]	ν [-]	ρ [kg/m^3]
71.7×10^9	0.33	2810

Table 4.5: Isotropic material properties adopted for the Lamb wave convergence analyses (Aluminum 7075).

To ensure that the observed differences are only due to the spatial discretisation and the through-thickness approximation, the time-integration parameters are kept fixed for all convergence studies. A total simulation time of 3×10^{-4} s is discretised into 300 uniform time steps, leading to a time increment $\Delta t = 1 \times 10^{-6}$ s. This choice satisfies the usual stability and accuracy requirements for explicit time-marching schemes in guided-wave simulations, where the time step is commonly selected so as to adequately resolve the highest frequency content of the excitation (see Section 3.3.2). On this basis, the adopted time step is considered sufficiently small to provide accurate Lamb-wave propagation results without incurring an unnecessary increase in computational cost.

For each analysis, the out-of-plane displacement $w(t)$, the global stress components $\sigma_{xx}(t)$ and $\sigma_{xz}(t)$ are extracted at the sensors. Although multiple sensors are available in the model, the convergence assessment reported in the following is based on a single

representative sensor located at $(x, y) = (0.15\text{ m}, 0.05\text{ m})$, whose time histories are compared against the chosen reference solution.

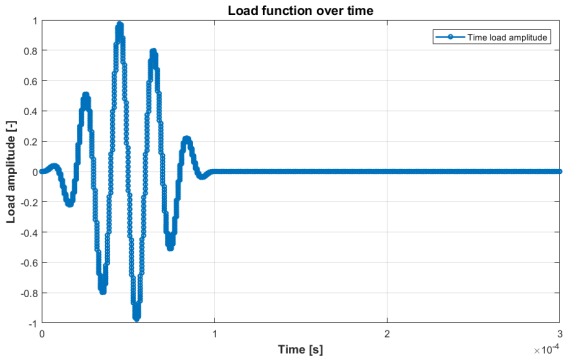

Figure 4.6: Time history of the applied Lamb-type load: five-cycle burst at a carrier frequency of 50 kHz with amplitude equal to 25.

The reference solution is obtained using the finest discretisation considered in the present study and, at least from a theoretical standpoint, is expected to provide the closest approximation to the actual response. It must be emphasised that, in the absence of an exact solution free from simplifying assumptions in the constitutive laws, it is not possible to rigorously quantify the deviation of the numerical signals from the actual physical response; therefore, the chosen reference is simply the model that is expected to approach the real behaviour more closely. Differently from the static case, convergence is assessed directly in the time domain by means of a normalised cross-correlation measure. Specifically, the normalised cross-correlation function is used to determine the optimal time lag between two signals and the corresponding maximum correlation coefficient.

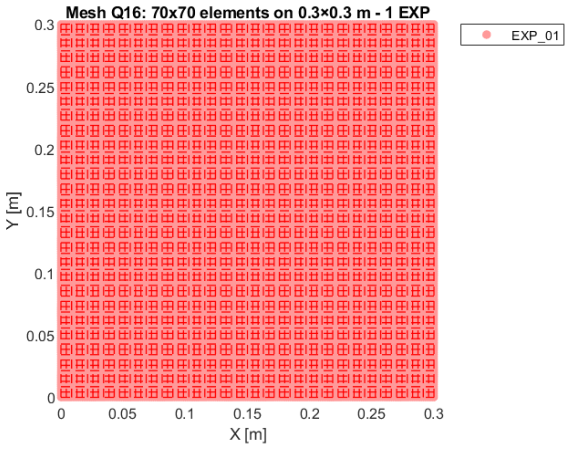

Figure 4.7: Example of a mesh adopted in the plate mid-plane (x-y) for the present study (70×70 Q16 elements).

4.4.1 Dispersion-based spatial resolution estimate

The expected spatial resolution requirements are estimated from the dispersion characteristics of the investigated plate. By considering the dispersion curves shown in Figure 4.8, obtained using the *Dispersion Calculator* developed by the Center for DLR Lightweight Production Technology [47], the most restrictive contribution at the adopted excitation frequency (50 kHz) is associated with the A_0 mode, whose wavelength is $\lambda_{A_0} = 18$ mm. For comparison, the corresponding wavelength of the S_0 mode at 50 kHz is $\lambda_{S_0} = 105$ mm. Therefore, the nodal spacing implied by the "10–20 nodes per wavelength" rule introduced in Section 3.3.1 can be estimated, based on λ_{A_0}, as

$$L_{\text{nodes}} = \frac{\lambda_{A_0}}{10\text{–}20} = 1.8\text{–}0.9 \text{ mm},$$

which yields an expected minimum total node count (for a 300 mm × 300 mm domain) equal to

$$N_{\text{nodes}} = \left(\frac{300}{1.8\text{–}0.9}\right)^2 = 2.78 \times 10^4\text{–}1.1 \times 10^5.$$

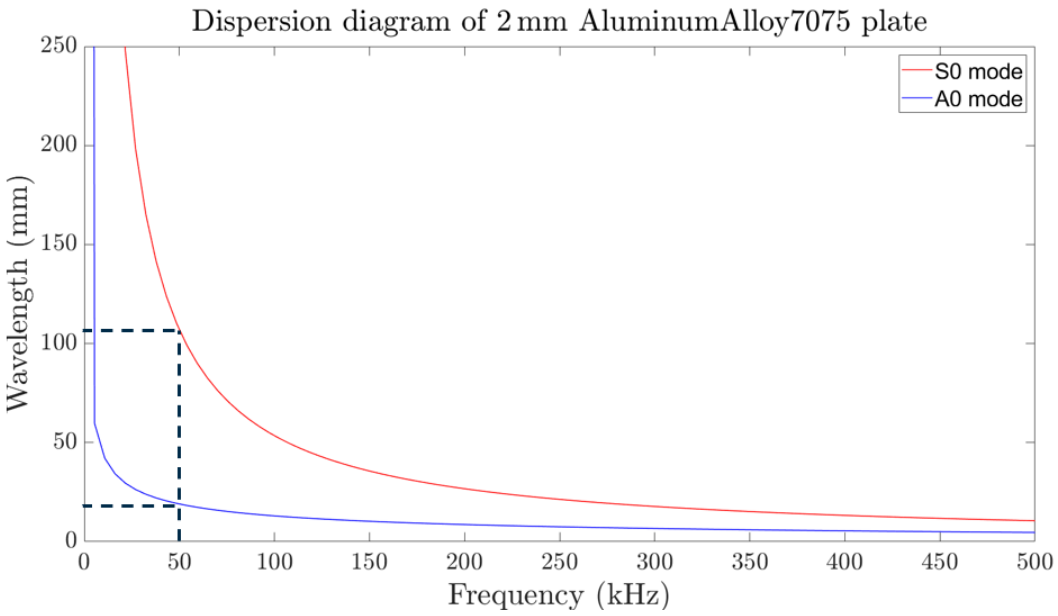

Figure 4.8: Dispersion curve of the investigated plate, computed with the DLR *Dispersion Calculator*, used to estimate the A_0 and S_0 wavelengths at 50 kHz.

4.4.2 Illustrative example: correlation factor

In order to clarify the adopted convergence metric and provide an intuitive interpretation of the correlation factor, a representative baseline analysis is first reported. The results shown in this illustrative example refer to the single-excitation benchmark case. In this example, the through-thickness expansion order is fixed (HLE2) and the in-plane element type is kept constant, while the mesh is progressively refined. Alongside the time histories obtained with the various discretisations in the x–y plane, bar plots are used to display the corresponding maximum correlation values. A summary table reports, for each mesh, the optimal lag and the associated maximum normalised cross-correlation coefficient.

The results obtained using linear Q4 elements are reported in Figure 4.9 and summarised in Table 4.6. These plots and numerical indicators allow the assessment of the convergence behaviour of the Lamb-wave response as the in-plane mesh density is progressively refined.

Mesh	Displacement $w(t)$		Global stress $\sigma_{xx}(t)$		Global stress $\sigma_{xz}(t)$	
vs 320×320 Q4	Max corr. [-]	Optimal lag	Max corr. [-]	Optimal lag	Max corr. [-]	Optimal lag
160×160 Q4	0.4796	-9	0.4164	-13	0.7345	-15
180×3180 Q4	0.5601	-7	0.5422	-10	0.8247	-11
200×200 Q4	0.6685	-5	0.7259	-7	0.8859	-8
240×240 Q4	0.8885	-3	0.8795	-4	0.9521	-4
280×280 Q4	0.9740	-1	0.9624	-2	0.9857	-2
320×320 Q4	1.0000	0	1.0000	0	1.0000	0

Table 4.6: Maximum normalised cross-correlation coefficient and optimal lag obtained with different Q4 meshes, with respect to the 320×320 Q4 reference.

The results show that, as the spatial discretisation is refined (i.e., by increasing the number of elements and, consequently, the total number of nodes), the time alignment required with respect to the reference solution progressively decreases: the optimal lag tends to values close to zero. At the same time, the maximum normalised cross-correlation coefficient increases and approaches unity, indicating an increasing similarity between the computed signals and those of the reference solution.

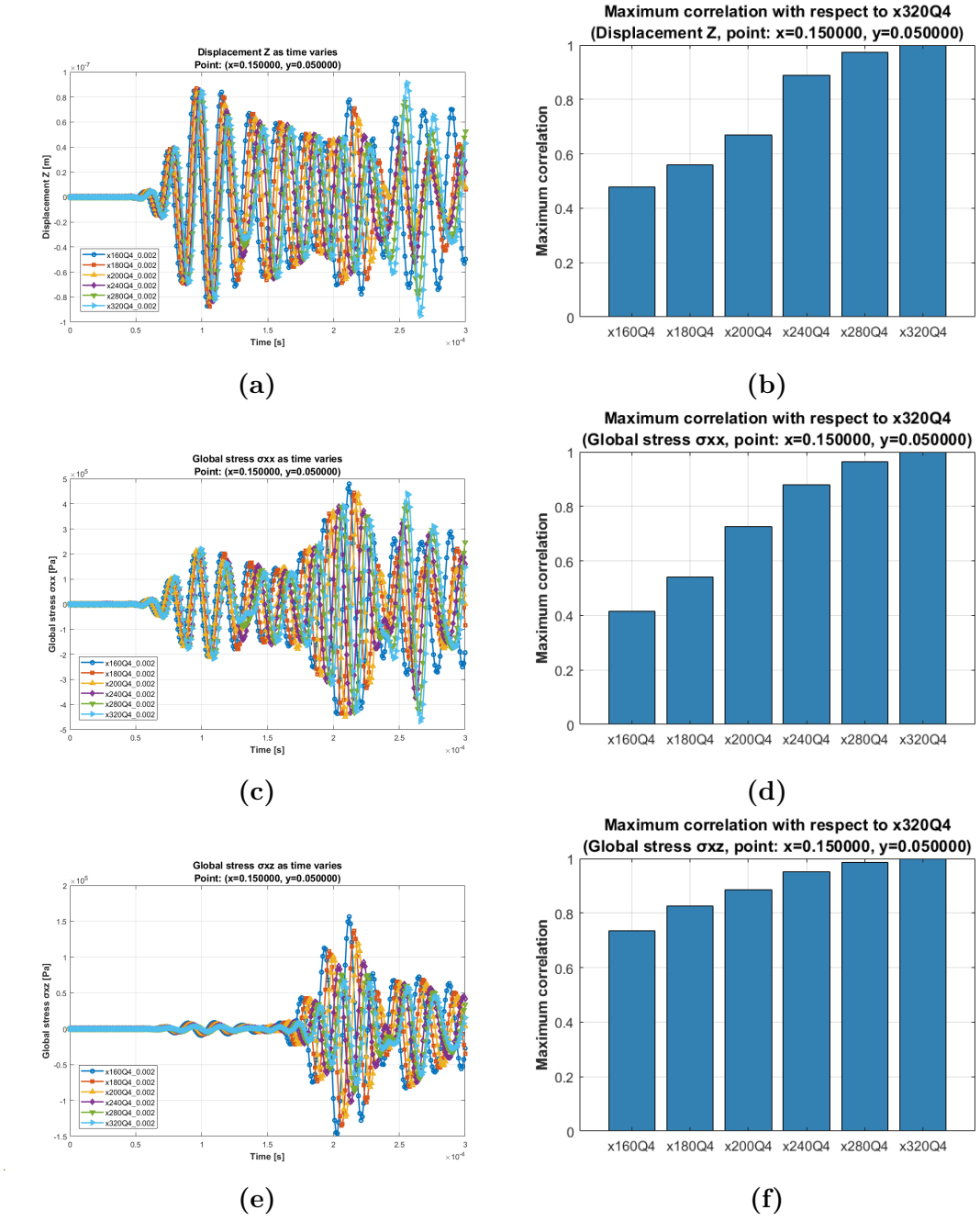

Figure 4.9: Lamb-wave convergence study for Q4 elements: (a), (c), (e) time histories of transverse displacement $w(t)$, in-plane normal stress $\sigma_{xx}(t)$ and transverse shear stress $\sigma_{xz}(t)$ at the selected sensor location for different mesh densities; (b), (d), (f) corresponding maximum normalised cross-correlation coefficients with respect to the reference solution obtained with the 320×320 Q4 mesh.

4.4.3 Single-excitation benchmark

In the single-excitation benchmark, convergence is assessed by plotting, on logarithmic axes, the error proxy

$$e = 1 - \rho_{\max},$$

where $\rho_{\max}$ denotes the maximum normalised cross-correlation coefficient introduced in the previous paragraphs. By construction, as the numerical solution approaches the reference one, $\rho_{\max} \to 1$ and the error proxy tends to zero, so that e remains strictly positive and is therefore well suited for a log-scale representation. The reference solution is taken, for all cases, as the response obtained with the finest discretisation, namely the 140×140 Q16 mesh with HLE3 through-thickness expansion.

The resulting log–log plots of e versus the total number of nodes N_{nodes} provide, at a glance, much richer information than the original correlation coefficients. In particular, they allow one to

- follow the convergence history over several orders of magnitude of the error;
- directly compare the behaviour of different families of discretisations, grouped according to the in-plane element type (Q4, Q9, Q16) and through-thickness expansion order (HLE1, HLE2, HLE3);
- identify the onset (or absence) of an asymptotic regime, in which the curves exhibit an approximately linear trend in the log–log plane.

Within this presumptive asymptotic range, an experimental convergence index m is estimated for each family by fitting a straight line to the last points of the corresponding curve in the $\log(e)$ versus $\log(N_{\text{nodes}})$ plane. In the present work, the fit is performed using at most the last six available points for each curve, under the assumption that the corresponding meshes are sufficiently fine to have entered (or approached) the asymptotic regime. To reduce the influence of numerical noise, data points with very small errors, specifically $e < 10^{-7}$, are discarded before performing the fit. It must be emphasised that the resulting values of m should be interpreted with care: they are computed with respect to a numerical reference solution (rather than the exact physical response), the error proxy e is not a relative error in the strict sense and in some cases the available data do not display a fully developed linear trend in the log–log scale. The indices m are therefore to be regarded as indicative measures of the convergence rate of each discretisation family.

Assuming that, asymptotically, the correlation error behaves as $e(h) \approx C\, h^p$, with h a characteristic mesh size and C a constant and recalling that in the present two-dimensional setting the total number of nodes scales as $N_{\text{nodes}} \sim h^{-2}$, one has

$$e(h) \approx C\, h^p \quad \Rightarrow \quad e(N_{\text{nodes}}) \approx C'\, N_{\text{nodes}}^m,$$

for some exponent m and constant C'. Taking the logarithm of both sides gives

$$\log(e) \approx \log(C') + m\, \log(N_{\text{nodes}}),$$

so that, in a $\log(e)$ versus $\log(N_{\text{nodes}})$ plot, the data should align along a straight line whose slope coincides with the convergence index m. In this work, this slope is used

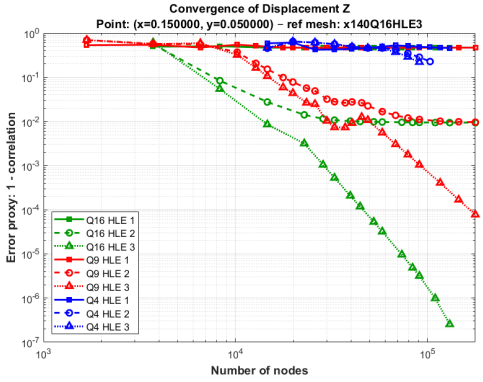

(a)

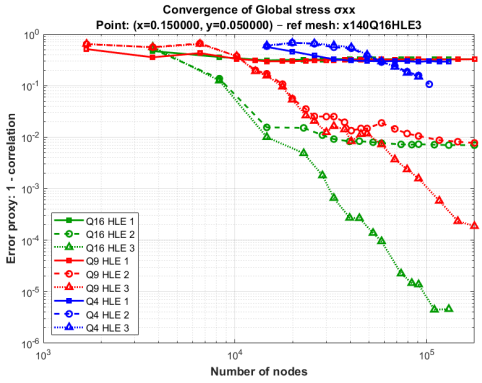

(b)

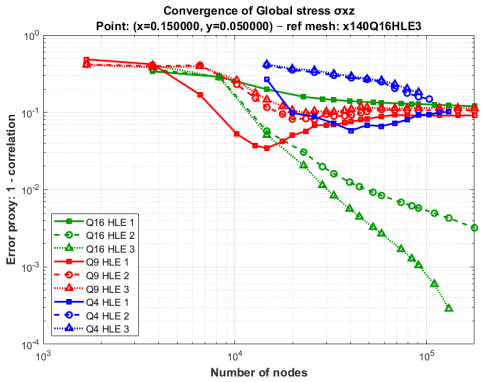

(c)

Figure 4.10: Convergence of the correlation factor as a function of the total number of nodes for different element types (Q4, Q9 and Q16), using the 140×140 Q16 mesh as reference solution: (a) transverse displacement $w(t)$; (b) global in-plane normal stress $\sigma_{xx}(t)$; (c) global transverse shear stress $\sigma_{xz}(t)$.

Discretisation	Displacement w: m	Global stress σ_{xx}: m	Global stress σ_{xz}: m
Q4 HLE 1	-0.2207	-0.0338	0.5251
Q4 HLE 2	-0.9749	-1.6034	-0.8482
Q4 HLE 3	-0.9537	-1.6422	-0.5931
Q9 HLE 1	0.0042	0.0106	-0.0132
Q9 HLE 2	-0.3474	-0.6314	-0.0076
Q9 HLE 3	-3.8440	-3.3377	0.0033
Q16 HLE 1	0.0012	-0.0027	-0.0942
Q16 HLE 2	-0.0244	-0.0443	-0.8576
Q16 HLE 3	-5.9075	-3.8241	-2.7209

Table 4.7: Estimated slopes m from the $\log(e)$ versus $\log(N_{\text{nodes}})$ plots for the single-excitation benchmark.

directly as a compact indicator of how rapidly the error proxy decreases with mesh refinement.

From the log–log plots and from the slopes reported in Table 4.7, a negative value of the index m indicates that the error proxy decreases as the number of nodes increases, i.e. that the corresponding family of discretisations exhibits convergence towards the reference solution. Conversely, values of m close to zero or even positive are associated with an error level that remains almost constant, or slightly increases, under mesh refinement, suggesting that the asymptotic regime has not been fully reached or that the behaviour of the error is affected by numerical noise and modelling uncertainties. In this sense, m should be interpreted as a qualitative indicator of the convergence rate: large negative slopes correspond to rapidly convergent formulations, whereas small-magnitude or positive slopes highlight cases in which the refinement does not lead to a clear and systematic reduction of the correlation error.

In particular, the plots highlight that formulations employing HLE1 are not sufficient to accurately capture the guided-wave response. For these cases, the correlation factor remains limited to values of approximately 0.6–0.8 for both the displacement $w(t)$ and the in-plane stress $\sigma_{xx}(t)$, while the transverse shear stress $\sigma_{xz}(t)$ is associated with error levels of the order of 10^{-1}.

If correlation errors below 10^{-2} are sought, one has to resort to higher-order through-thickness expansions, such as Q16 elements with HLE2 or HLE3 and more than 10^4 nodes. Alternatively, Q9 elements also provide satisfactory convergence for $w(t)$ and $\sigma_{xx}(t)$, but they remain less effective in reducing the out-of-plane shear stress error, which confirms $\sigma_{xz}(t)$ as the most demanding quantity in terms of spatial resolution and kinematic richness.

More generally, the convergence indices m support these observations: for all three response quantities, the Q4 families exhibit only mild or irregular decay of the error proxy, indicating that they do not approach the reference solution in a robust way within the considered mesh range. The Q9 formulations display more favourable (i.e., more negative) values of m, especially when combined with higher through-thickness orders, suggesting

that they can represent a viable compromise between accuracy and computational cost, albeit with a slower convergence rate than the Q16 elements.

4.4.4 Two-excitation benchmark

In the two-excitation benchmark, the convergence analysis is performed in a way entirely analogous to the single-excitation case outlined in Section 4.4.3. The resulting slopes m are reported in Table 4.8.

Discretisation	Displacement w: m	Global stress σ_{xx}: m	Global stress σ_{xz}: m
Q4 HLE 1	-1.7040	-0.6356	0.0176
Q4 HLE 2	-1.9856	-1.5258	0.0070
Q4 HLE 3	-1.9831	-1.5206	0.0047
Q9 HLE 1	0.0146	-0.5744	-0.0283
Q9 HLE 2	-1.1711	-1.8506	-0.0276
Q9 HLE 3	-3.3608	-2.1974	-0.0250
Q16 HLE 1	-0.0913	-0.0442	-1.3161
Q16 HLE 2	-0.9476	-0.8810	-3.5539
Q16 HLE 3	-4.9417	-2.1655	-3.5145

Table 4.8: Estimated slopes m from the $\log(e)$ versus $\log(N_{\text{nodes}})$ plots for the two-excitation benchmark.

The results indicate that, in the two-excitation case, the correlation errors are significantly lower for both the displacement $w(t)$ and the in-plane stress $\sigma_{xx}(t)$, especially when higher-order through-thickness expansions are used. Even the Q4 elements show interesting convergence behaviour for these quantities, with clearly negative m values suggesting a robust reduction of the error as the mesh is refined. For $\sigma_{xz}(t)$, by contrast, only the Q16 elements yield consistently high convergence rates, while Q9 and Q4 formulations exhibit values of m close to zero or slightly positive, indicating that the error level for the transverse shear stress remains almost constant under mesh refinement.

This behaviour suggests that the introduction of the symmetric mode and the presence of a second excitation source make the accurate representation of σ_{xz} particularly sensitive to the in-plane discretisation and to the element type. This can be attributed to the fact that, under symmetric excitation, σ_{xz} takes values close to zero throughout the thickness; as a consequence, the convergence indicators lose reliability, since small absolute differences between models translate into disproportionately large relative errors when the reference quantity is near-zero.

Moreover, since the employed method is in weak form, the solution satisfies the integral statement of the governing equations but not necessarily the pointwise one. Evaluating the error at a specific point may therefore result in a pointwise discrepancy between the numerical and reference solutions, especially for derivative-based quantities such as stresses and the local character of the present analysis should be taken into account when interpreting the convergence indices.

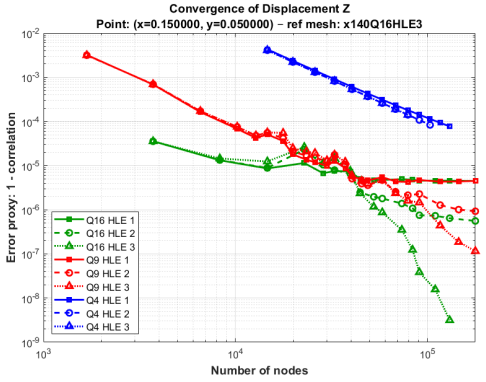

(a)

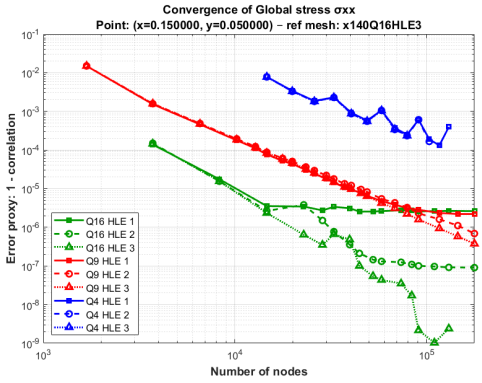

(b)

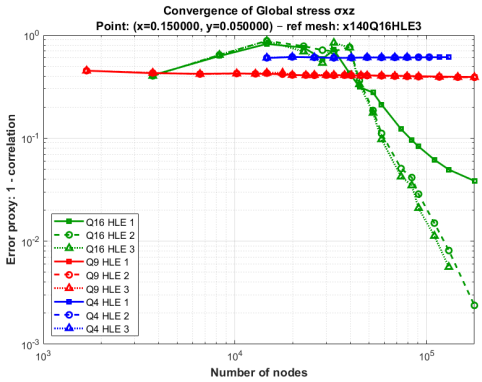

(c)

Figure 4.11: Convergence of the correlation factor as a function of the total number of nodes for different element types (Q4, Q9 and Q16), using the 140×140 Q16 mesh as reference solution: (a) transverse displacement $w(t)$; (b) global in-plane normal stress $\sigma_{xx}(t)$; (c) global transverse shear stress $\sigma_{xz}(t)$.

4.5 Sensitivity to Damage Variations

In this section, two alternative strategies for introducing damage in the analysed plates are first presented, followed by two preliminary studies aimed at assessing the influence of both damage size and location, with the objective of identifying patterns that can support the development of a Lamb-wave-based structural health monitoring system. The subsequent analyses are carried out using one of the numerical models defined in the previous subsections. In terms of in-plane discretisation of the x–y mesh, a model was selected that provides a favourable compromise between computational cost and reliability of the results for the two-excitation benchmark. In particular, the 80×80 Q16 HLE3 configuration was adopted as the "final" model.

4.5.1 Damage Introduction in Homogeneous Plates

In a homogeneous plate, several physical mechanisms may lead to a degradation of the structural performance, ranging from manufacturing-related defects to damage induced by the service environment. Without entering into the details of these phenomena, the aim of the present and the following chapter is to illustrate how a reduction of mechanical performance is introduced in both a homogeneous and a composite plate. Owing to the isotropic nature of the material considered in this section, damage is modelled by assigning to a selected set of "defective" elements the same physical and geometrical properties as the undamaged ones, except for a prescribed percentage reduction of the Young's modulus through the entire thickness. Figure 4.13 highlights in green (EXP_02) the elements affected by damage, whereas Table 4.9 summarises the material parameters associated with the two laminations introduced via two distinct EXP files, as anticipated in Section 2.4. In particular, the Young's modulus of the damaged material is set to 10% of the undamaged value, while Poisson's ratio and mass density are kept unchanged.

Material	Young's modulus E [Pa]	Poisson's ratio ν [-]	Density ρ [kg/m^3]
MAT 1 (undamaged)	71.7×10^9	0.33	2810
MAT 2 (damaged)	71.7×10^8	0.33	2810

Table 4.9: Material properties adopted for the homogeneous plate: undamaged material (EXP_01, MAT 1) and damaged material (EXP_02, MAT 2).

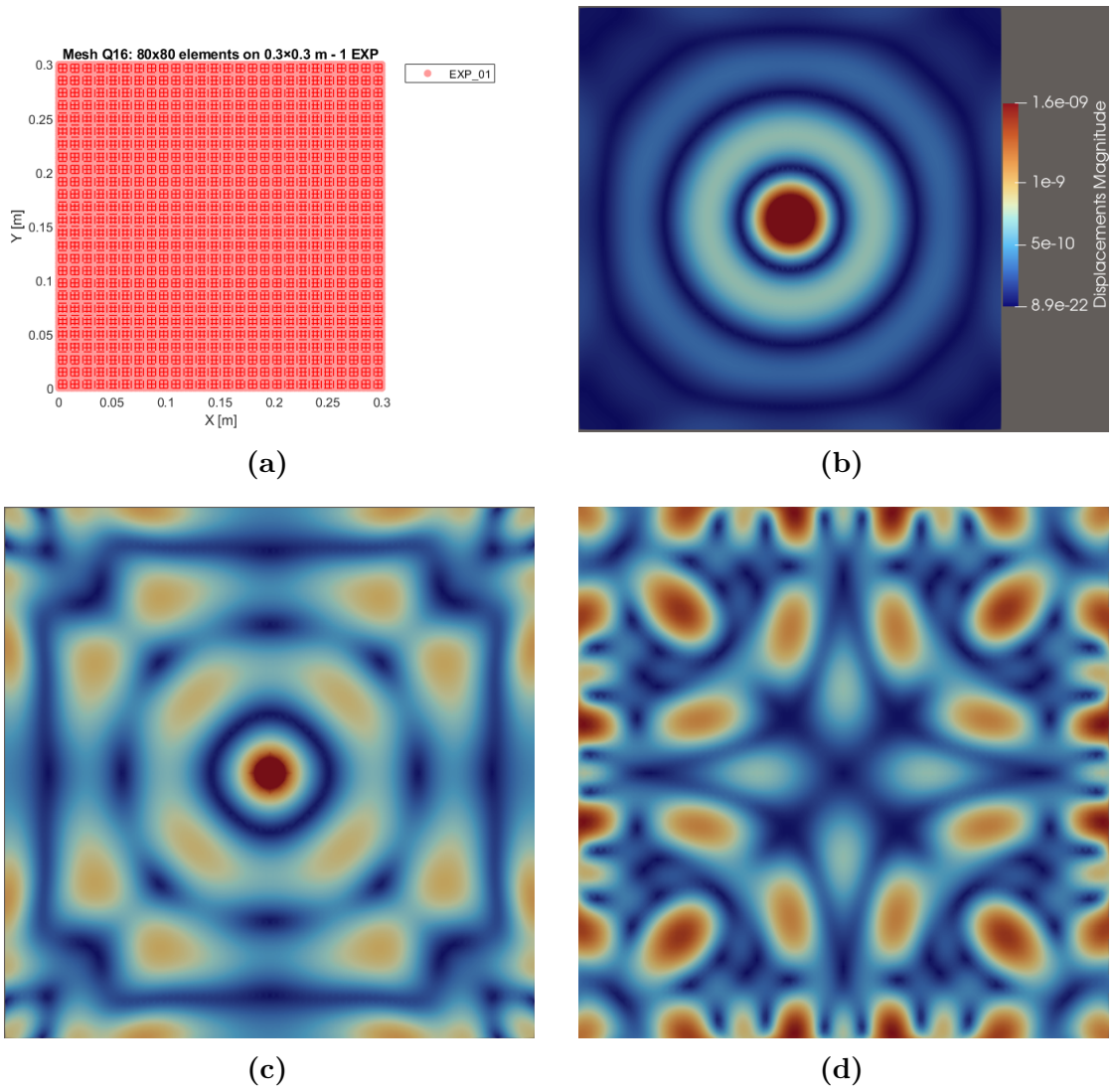

Figure 4.12: In-plane mesh adopted for the final numerical model and representative snapshots of the Lamb-wave propagation in the homogeneous plate: (a) finite element mesh in the x-y plane; (b) out-of-plane displacement field (in meters) at $t = 4.5 \times 10^{-5}$ s; (c) $t = 7.5 \times 10^{-5}$ s; (d) $t = 1.5 \times 10^{-4}$ s.

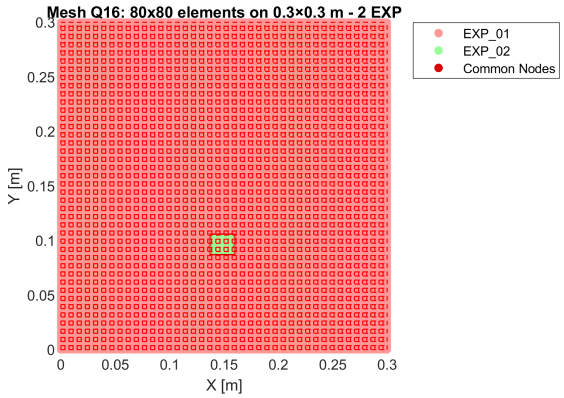

Figure 4.13: In-plane mesh of the homogeneous plate showing the region affected by stiffness reduction.

4.5.2 Damage Introduction in Composite Plates

In order to model damage in a more realistic way for composite structures, a different approach is adopted with respect to the homogeneous case. In this case, the damaged elements are assigned the same stacking sequence as the undamaged ones, but with reduced material properties for one or more laminate plies, as shown in Figure 4.14. In this manner, one of the main degradation mechanisms in composite materials, namely delamination, is reproduced in a simplified form. These proposed modelling strategies are therefore intended to illustrate possible approaches to this problem rather than to provide a definitive solution.

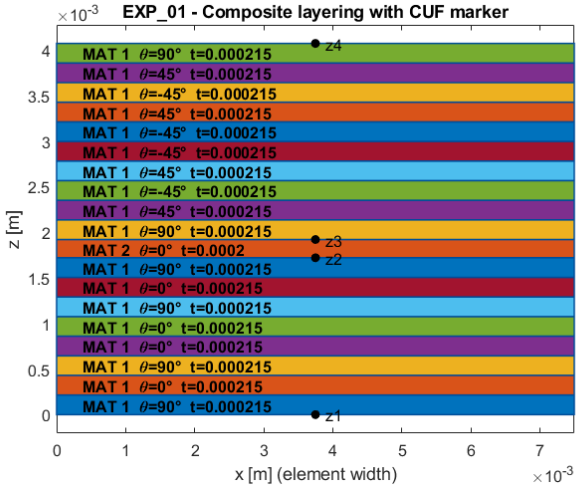

Figure 4.14: Through-thickness lay-up adopted for the composite plate, where a single laminate ply (MAT 2) is assigned modified material properties.

4.5.3 Results for Varying Damage Position

In this first study, the damage position is varied while keeping its extent fixed. The defect is modelled as a cluster of four finite elements with reduced stiffness (a 10% reduction of the Young's modulus) and its x-coordinate is kept constant at $x = 0.15$. The y-coordinate is progressively moved closer to one of the virtual sensors (S2), as illustrated in Figure 4.18, while remaining between the excitation point at the centre of the plate, $(x, y) = (0.15, 0.15)$ and the sensor location at $(x, y) = (0.15, 0.05)$. Specifically, the y-coordinate of the damaged region ranges from $y = 0.075$ to $y = 0.13125$ in five incremental steps, whose values are reported in the legends of the corresponding result plots. For each configuration, the resulting waveforms are compared with the pristine-plate response, in order to highlight systematic changes in the arrival times and amplitudes that can be associated with the varying distance between the damage and the sensor.

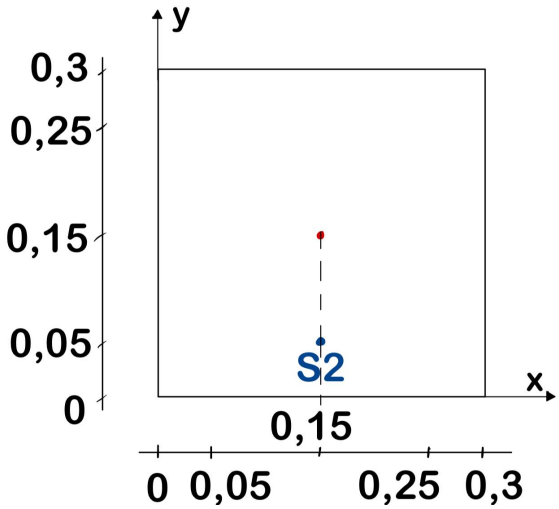

Figure 4.15: Schematic representation of the plate with the excitation point (red dot) and the virtual sensor "S2" (blue dot).

Referring to the results shown in Figure 4.16, the choice to represent the signals in terms of displacement u_y and stress σ_{xx} was made arbitrarily, as different physical quantities can highlight complementary damage-sensitive patterns. It is crucial to focus on the early-time response, before boundary reflections distort the signal (as highlighted by the zoomed views in Figure 4.16(b,d)).

For the displacement u_y, a systematic decrease in amplitude is observed as the defect moves away from the sensor (from $y_d = 0.075$ to $y_d = 0.13125$), while the time of flight remains nearly constant. This behaviour reflects the attenuation of the backscattered contribution generated by the defect: when the damage is located closer to sensor S2, the scattered waves travel a shorter path before being recorded and therefore reach the sensor with larger amplitude. Conversely, as the defect moves farther from the sensor (closer to the source), the scattered component must propagate over a longer distance to reach S2, leading to increased attenuation and a reduced amplitude at the sensor,

without introducing a significant change in the overall time of flight.

Conversely, the stress σ_{xx} exhibits a clear delay in the arrival time of the main peaks, with progressively later crests as y_d increases. This time shift arises because the defect acts as a scattering centre that modifies the primary wavefront propagation: defects farther from the sensor cause greater phase delays detectable in the stress field, which is inherently sensitive to wave propagation characteristics through its derivative nature. These complementary effects, amplitude variation for displacement and time-of-flight shift for stress, provide distinct features for damage localisation.

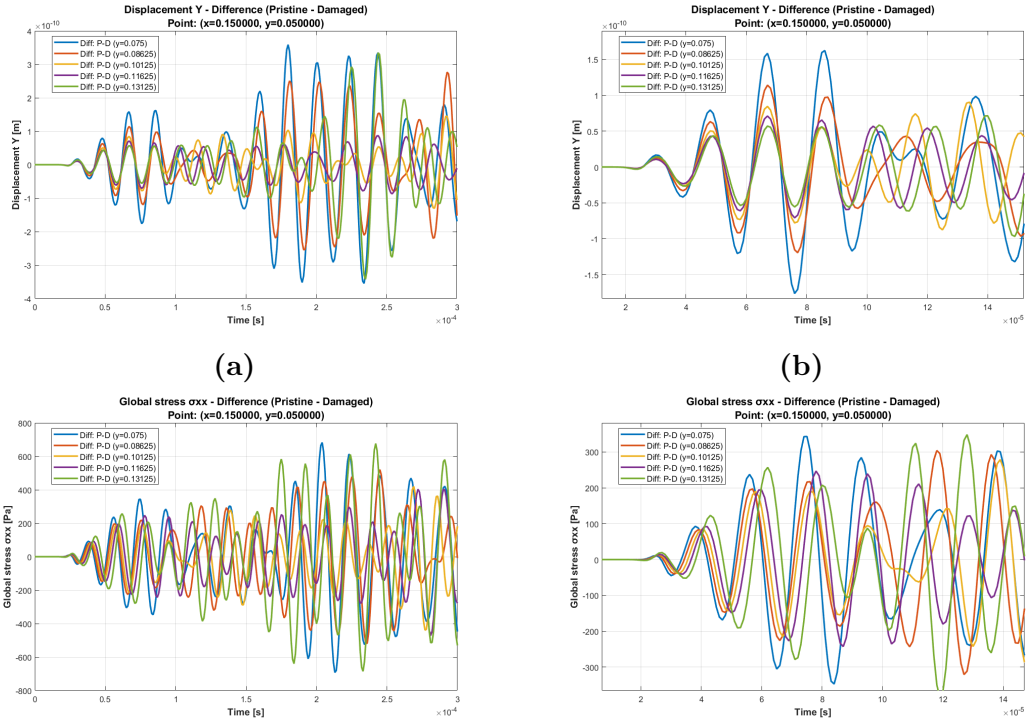

Figure 4.16: Comparison of pristine vs damaged responses at sensor S2 for different damage positions ($y_d = \{0.075, 0.08625, 0.10125, 0.11625, 0.13125\}[m]$). Both displacement u_y and stress σ_{xx} are shown in full time range (a,c) and zoomed view (b,d) of the early-time response.

4.5.4 Results for Varying Damage Size (Number of Elements)

In the second study, the extent of the damage is varied while keeping its position fixed. The defect is modeled as a cluster of finite elements with reduced stiffness and its centroid is positioned at $(x_d, y_d) = (0.15, 0.1)$, approximately midway between the excitation point and sensor S2. Specifically, the number of damaged elements increases from 2 to 36 elements[1], forming progressively larger clusters aligned along the wave propagation path.

Figure 4.17 shows that for both quantities, a clear trend emerges: as damage size increases, both the amplitude increases and the time of flight (TOF) exhibits a progressive delay.

This dual effect can be explained by the combined influence of two mechanisms:

1. Enhanced backscattering (similar to the position-variation study): Larger damage zones intercept more of the primary wavefront closer to the source, producing stronger reflections that travel the full source-damage-sensor path and arrive with greater amplitude.
2. Increased scattering/diffraction delay: Unlike the position study, where only the interaction distance changed, here the physical size of the obstacle grows substantially. The wavefront must now diffract around a larger scattering object, introducing additional phase delay independent of the source-damage distance. This effect is more pronounced for stress σ_{xx}, which is inherently sensitive to wavefront distortion through its derivative nature.

These combined effects, amplitude enhancement from stronger scattering and TOF delay from diffraction around larger obstacles, provide complementary features that are robust indicators of damage severity.

These controlled studies demonstrate that variations in both damage position and size produce distinct, reproducible signatures in the early-time wave responses captured across the sensor network.

The key insight is that these identifiable patterns, regardless of the specific physical field measured by practical sensors, provide the foundation for training artificial intelligence models. Such models can then autonomously process large volumes of multi-sensor data to localize damage position and characterize its extent, enabling robust structural health monitoring in operational environments.

[1]O denotes "horizontal" orientation: when the number of elements did not form a perfect square, rectangular clusters were extended horizontally along the wave propagation path.

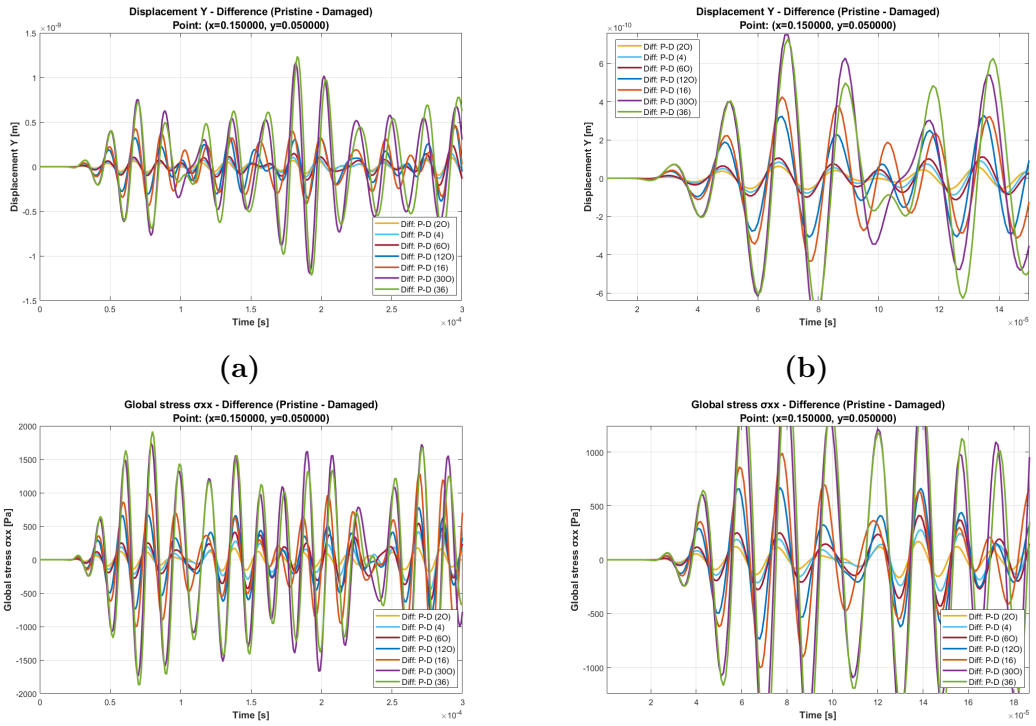

Figure 4.17: Comparison of pristine vs damaged responses at sensor S2 for different damage sizes (2O, 4, 6O, 12O, 16, 30O, 36 elements). Both displacement u_y and stress σ_{xx} are shown in full time range (a,c) and zoomed view (b,d) of the early-time response.

4.6 A.I. Based Damage Localization

This final results section builds upon the outcomes obtained in Section 4.5, converging the sensitivity analyses into a unified damage localization framework applied to a plate identical to that used in the preceding study and selected on the basis of the convergence analyses previously carried out.

In particular, Figure 4.13 schematically illustrates both the virtual sensor network implemented on the upper surface of the plate and the damage zone, highlighted in orange, which defines the region within which the damage is positioned across all the analyses included in the initial dataset. In this regard, it is important to specify that the present study focuses on a simplified yet representative configuration: the model is trained in the absence of environmental variability and its target is limited to the estimation of the x and y coordinates of the damage within the plate.

Two separate regression models are trained, one for each spatial coordinate, as this approach is better suited to the single-output formulation adopted in this study and generally yields more accurate predictions. The overall workflow is managed through a dedicated *MATLAB* code (`AI_CODE.m`), which automates the feature extraction, dataset assembly and preliminary model evaluation steps described in the following sections. The *MATLAB Regression Learner* application is then employed as a complementary tool, leveraging its graphical interface to perform a systematic comparison of multiple regression algorithms including linear models, regression trees, support vector machines, Gaussian process regression and ensemble methods.

It is worth noting that the problem can be progressively extended in complexity by introducing additional target variables (such as damage size, severity, or environmental factors) and by providing increasingly comprehensive datasets, following the baseline methodology established in this study.

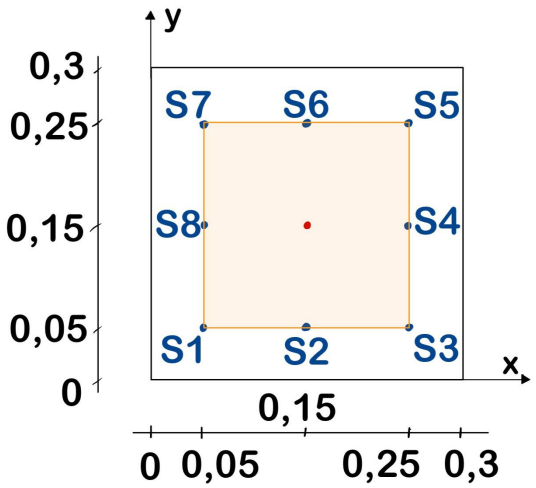

Figure 4.18: Schematic representation of the plate with the excitation point (red dot) and virtual sensors (blue dots). In orange is highlighted the "damage zone", within which the defect can be localised.

4.6.1 Feature Extraction and Dataset Construction

The first fundamental step towards training the localization model is the identification of suitable features to be provided as input for each analysis in the dataset. As an initial approach, rather than passing the complete time-domain signals (in terms of displacement, strain and stress) for each of the eight sensors present on the plate, it is more effective to extract from these signals a set of compact parameters that synthesize their informational content.

To this end, a structured feature extraction procedure was implemented, constructing a table that, for all eight sensors and for each of the following output variables:

$$\texttt{signalList} = \{\, U_x,\ U_y,\ U_z,\ \sigma_{xx},\ \sigma_{yy},\ \sigma_{xy} \,\}$$

extracts a set of scalar parameters from each time-domain signal. The code implements the following available features:

- **max**: the maximum value of the signal over time;
- **min**: the minimum value of the signal over time;
- **rms**: the Root Mean Square, computed as $\sqrt{\frac{1}{N}\sum_{i=1}^{N} x_i^2}$, providing a measure of the signal energy content;
- **mean**: the arithmetic mean of the signal;
- **std**: the standard deviation;
- **final**: the value of the signal at the last time step;
- **peakabs**: the signal value at the absolute peak instant;
- **idxpeak**: the time index corresponding to the absolute peak;
- **idxpeaknorm**: the normalized peak index, defined as the peak time index divided by the total number of time steps;
- **pre20**: the signal value 20 time steps before the peak;
- **post20**: the signal value 20 time steps after the peak.

For the present study, the subset selected for the initial dataset construction is:

$$\texttt{featureList} = \{\, \texttt{max},\ \texttt{rms},\ \texttt{final},\ \texttt{pre20},\ \texttt{post20} \,\}$$

yielding, for the full training dataset of 385 analyses, a feature table $\mathbf{T}$ of dimensions $385 \times (8 \times 6 \times 5) = 385 \times 240$. In addition, two target vectors $\mathbf{X}$ and $\mathbf{Y}$ are constructed, collecting the x and y damage coordinates for each analysis, respectively. These vectors represent the output quantities that the model is required to predict and are provided separately to the two regression models, one per spatial coordinate.

It should be noted that the selected features were chosen on a heuristic basis, as they are expected to carry information relevant to damage localization; however, alternative feature sets could potentially lead to improved model performance.

4.6.2 Feature Selection and Relevance Analysis

Starting from the 240 available features, the first part of `AI_CODE.m` implements dedicated routines to identify the most informative subset according to three evaluation criteria, each based on well-established regression performance metrics. In particular, the metrics used throughout the selection process are:

- **RMSE** (Root Mean Square Error): $\sqrt{\frac{1}{N}\sum_{i=1}^{N}(\hat{y}_i - y_i)^2}$, measuring the average magnitude of prediction errors. It should be noted that RMSE is particularly sensitive to large individual errors, as squaring the residuals gives disproportionate weight to analyses in which the model produces significantly inaccurate predictions;
- **MAE** (Mean Absolute Error): $\frac{1}{N}\sum_{i=1}^{N}|\hat{y}_i - y_i|$, providing a more robust measure of average deviation, less influenced by isolated outlier predictions;
- R^2 (coefficient of determination): quantifying the proportion of variance in the target variable explained by the model, with values closer to 1 indicating better predictive performance.

The three feature selection methods implemented are the following:

- **Random feature search.** The code performs a randomized search over subsets of features of fixed size for a given target variable (x_{damage} or y_{damage}). Each candidate subset is evaluated by training a linear regression model (`fitrlinear`) with K-fold cross-validation[2], computing RMSE, MAE and R^2 for each trial. The features most frequently appearing in the top-performing subsets are then returned as the most relevant candidates.
- **Sequential feature selection with linear regression criterion.** A more structured selection is carried out using the MATLAB `sequentialfs` function, which builds the feature subset incrementally by evaluating a user-defined criterion function. The target variable is selected via `responseVar`, while `directionMode` controls whether the search proceeds in *forward* mode, in which one feature at a time is added as long as model performance improves, or in *backward* mode, in which the search starts from the full feature set and progressively removes the least informative features. The criterion function is based on a linear regression model.
- **Sequential feature selection with SVM criterion.** This method follows the same sequential selection strategy as the previous one, but replaces the linear criterion function with a Support Vector Machine (SVM) regressor using a Gaussian (RBF) kernel, trained via `fitrsvm`. SVM regression with a Gaussian kernel maps the input features into a high-dimensional space, allowing the model to capture nonlinear relationships between the features and the target coordinate.

[2] K-fold cross-validation partitions the dataset into K equally sized folds, trains the model on $K-1$ of them and validates it on the remaining one, repeating the process K times so that every sample is used for validation exactly once.

The choice of adopting SVM as the guiding criterion for feature selection was not made a priori, but rather emerged as a consequence of the model selection study described in Section 4.6.3. Indeed, an initial feature selection based on the linear regression criterion was first carried out and the corresponding subset was used to perform a preliminary comparison of candidate regression models. The results of that analysis consistently indicated SVM-based regression as the best-performing approach; it was therefore considered appropriate to repeat the feature selection using SVM as the criterion function, so as to identify the subset most suited to that specific model class.

The optimal feature subsets identified through forward SVM-based sequential selection are reported below. For the x-coordinate target, the selected features are:

- `S2_Uz_max`
- `S3_Ux_max`
- `S3_Uy_max`
- `S3_sigxx_max`
- `S3_sigxx_rms`
- `S3_sigyy_max`
- `S3_sigyy_rms`
- `S4_sigyy_post20`
- `S5_Ux_max`
- `S5_Ux_rms`
- `S5_Uy_max`
- `S5_sigxx_final`
- `S5_sigyy_max`
- `S5_sigyy_rms`
- `S6_sigxx_post20`
- `S7_sigxx_final`

For the y-coordinate target, the selected features are:

- `S1_Ux_max`
- `S1_Uy_max`
- `S1_sigxx_max`
- `S1_sigxx_rms`
- `S2_Uz_pre20`
- `S2_sigxx_max`
- `S2_sigxx_post20`
- `S2_sigxx_pre20`
- `S3_Ux_post20`
- `S3_Ux_rms`
- `S3_Uz_max`
- `S3_sigxx_max`
- `S3_sigxx_post20`
- `S3_sigyy_max`
- `S3_sigxx_pre20`
- `S4_Uz_max`
- `S8_Uz_post20`

The two subsets exhibit a comparable level of complexity, comprising 16 and 17 features respectively and both draw from a diverse combination of displacement components (U_x, U_y, U_z) and stress quantities (σ_{xx}, σ_{yy}), distributed across multiple sensors. This diversity suggests that the localization of damage along each coordinate relies on complementary physical information captured at different locations on the plate. It is worth noting that, in a practical implementation, the actual measurable quantities would depend on the type of sensors deployed; displacement and strain components could be acquired through piezoelectric sensors or FBGs, while stress quantities would generally require indirect estimation from measured strains via the constitutive relations of the material.

4.6.3 Model Selection and Optimization

The model selection process was carried out in two sequential stages, following the logical progression mentioned before. In the first stage, the feature subset identified through linear-regression-based sequential selection was used to perform a systematic comparison of four candidate regression models, evaluated on the same feature subset and the same cross-validation partition to ensure a fair benchmark. The models considered are a linear regression model, a linear SVM regressor, a Gaussian SVM regressor and an automatically selected model via `fitrauto`, the MATLAB function for automatic regression model selection, which internally explores a range of algorithms and returns the best-performing one. All results are collected into a summary table sorted by increasing RMSE, allowing immediate identification of the best-performing model.

The results of this comparison for the x-coordinate target are reported in Table 4.10 and consistently indicate the Gaussian SVM as the most accurate approach, motivating the subsequent tuning stage and the adoption of SVM as the criterion function in the feature selection phase described in Section 4.6.2.

Model	**RMSE**	**MAE**	R^2
Gaussian SVM (`fitrsvm`)	0.02425	0.01673	0.808
Auto (`fitrauto`)	0.03220	0.02346	0.662
Linear SVM	0.03697	0.02643	0.554
Linear regression	0.05293	0.04511	0.086

Table 4.10: Model comparison for the x-coordinate target using the feature subset identified through linear-regression-based sequential selection.

In the second stage, a dedicated hyperparameter tuning was performed to verify whether an optimisation of the Gaussian SVM could further improve predictive performance. The model is trained with automatic optimisation of three key hyperparameters: **BoxConstraint**, which controls the penalty assigned to training errors; **KernelScale**, which determines the width of the Gaussian kernel and influences how locally or globally the model fits the data; and **Epsilon**, which defines the width of the insensitive band around the regression function within which errors are not penalised.

The optimisation process generates a Minimum MSE plot, shown in Figure 4.19a, which tracks the evolution of two quantities across iterations: the *observed minimum MSE*, representing the best validation loss actually measured up to that iteration and the *estimated minimum MSE*, which is the surrogate model's prediction of the optimal loss based on the evaluations performed so far. The rapid convergence observed within the first few iterations, followed by a stable plateau, carries two complementary pieces of information: on one hand, it indicates that the optimiser located a well-defined minimum of the loss surface early in the search, suggesting that the hyperparameter landscape is relatively smooth and that the Gaussian SVM is well-suited to this regression task; on the other hand, it reflects the quality of the dataset itself, since a noisy or poorly structured dataset would typically produce a more irregular convergence curve with slower stabilisation.

Table 4.11 reports the optimised hyperparameters and performance metrics for both models, with R^2 above 0.81, confirming good generalisation to unseen damage positions.

	x-coordinate model	**y-coordinate model**
Kernel	Gaussian	Gaussian
Standardize	true	true
BoxConstraint	0.1650	0.1358
KernelScale	1.3729	0.6652
Epsilon	2.66×10^{-4}	1.09×10^{-3}
Num. features	16	17
RMSE (CV)	0.02284	0.02473
MAE (CV)	0.01485	0.01633
R^2 (CV)	0.830	0.816

Table 4.11: Optimised hyperparameters and cross-validated performance metrics for the two tuned Gaussian SVM models, targeting the x- and y-damage coordinates.

A closer inspection of the response plot in Figure 4.19, which shows the predicted versus true x-coordinate values across all the observations, also reveals an interesting characteristic of the dataset composition. The 385 training analyses were assembled by combining two complementary strategies: 169 analyses with damage placed at regularly spaced positions forming a structured grid over the damage zone, providing the model with a uniform spatial coverage of the input domain and 216 analyses with randomly positioned damage, introducing variability and ensuring that the model is exposed to a denser and more representative sampling of the target space. This hybrid strategy proved more effective than either the structured grid or random sampling alone, yielding better generalisation performance.

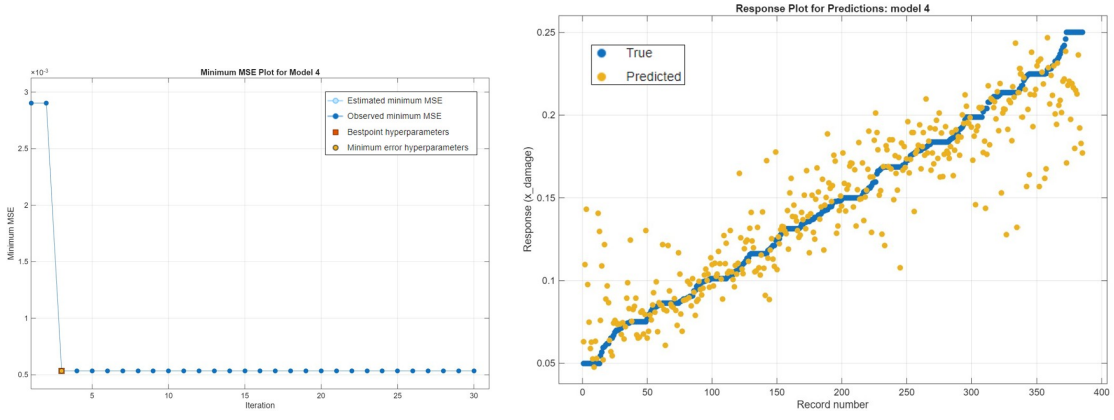

(a) **(b)**

Figure 4.19: **(a)** Minimum MSE plot for the x-coordinate model. **(b)** Response plot for the x-coordinate model over the 385 training observations.

4.6.4 Model Validation and Predictive Performance

The final stage applies the trained models to predict damage positions on a dedicated set of analyses never used during training. Evaluating on unseen data is essential to obtain an unbiased estimate of generalisation performance, since testing on training samples would artificially inflate accuracy by rewarding memorisation rather than true predictive ability.

For each test case, the models produce predictions $\hat{x}$ and $\hat{y}$, which are compared against the true coordinates x_{true} and y_{true}. The overall Euclidean error is computed as:

$$e_{xy} = \sqrt{(\hat{x} - x_{\text{true}})^2 + (\hat{y} - y_{\text{true}})^2}$$

which represents the most meaningful measure of localisation quality, as it captures the total displacement between the predicted and actual damage position in the plane.

For each test case, a figure is generated overlaying the predicted and true damage positions on the plate map, as shown in Figure 4.20, providing immediate visual feedback on localisation accuracy. The per-axis errors are also expressed as relative percentage quantities to facilitate interpretation across different plate geometries.

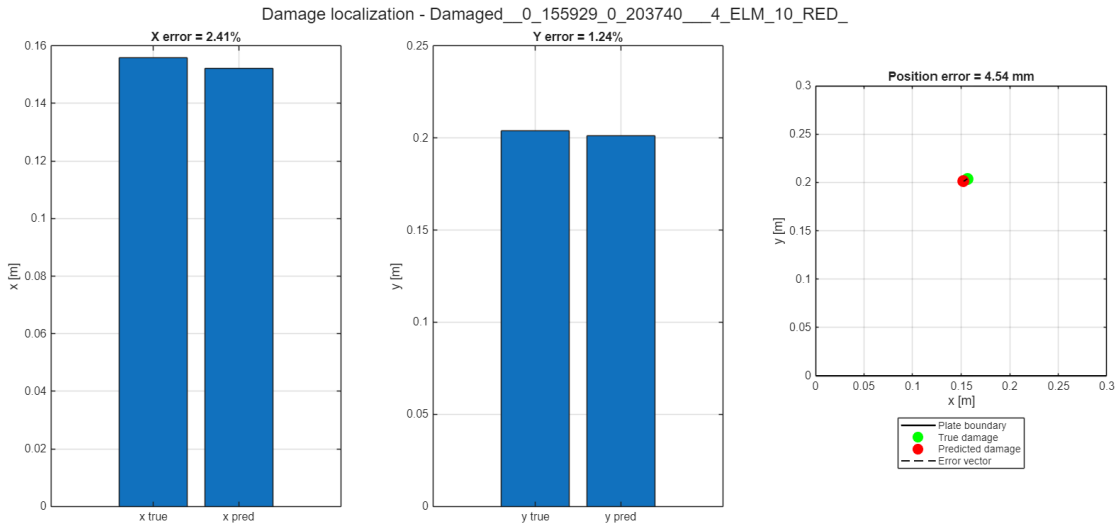

Figure 4.20: Damage localisation output for a representative test case: per-axis predictions and relative percentage errors (left) and true vs. predicted position on the plate map (right).

The validation was conducted on 50 unseen analyses. The models achieved a mean Euclidean error of 21.08 mm, which is a highly satisfactory result, demonstrating that the trained models generalise effectively and are capable of localising damage with millimetre-level accuracy on previously unseen structural configurations.

Chapter 5

Conclusions

5.1 Summary of Main Results

This thesis developed and validated a comprehensive numerical framework for guided-wave-based structural health monitoring of thin plates, combining the Carrera Unified Formulation with an artificial intelligence model for damage localisation.

The h/p convergence studies on composite plates under static loading demonstrated that Lagrange-type through-thickness expansions provide accurate and rapidly convergent solutions. In the thin-plate configuration, Taylor expansion models converge to the LE2 reference approximately at the fifth order, while in the thick-plate case the relative errors are 1–2 orders of magnitude larger, consistent with the local approximation properties of Taylor polynomials. The comparison between ESL and LW modelling strategies confirmed that the ESL approach introduces significant quantitative and qualitative discrepancies in through-thickness stress profiles, particularly for shear quantities and that increasing the expansion order within an ESL framework does not recover the layer-wise behaviour.

For dynamic analyses, the convergence study on Lamb-wave propagation showed that HLE1 through-thickness expansions are insufficient to accurately resolve the guided-wave field, with correlation errors remaining at the level of of approximately 0.6–0.8 for both the displacement $w(t)$ and the in-plane stress $\sigma_{xx}(t)$, combining Q16 in-plane elements with HLE2 or HLE3 expansions yields rapidly convergent solutions with errors below 10^{-2}. On this basis, the 80×80 Q16 HLE3 configuration was selected as the final model, providing the most suitable trade-off between computational cost and accuracy.

The sensitivity analyses demonstrated that variations in damage position and size produce distinct, reproducible signatures in the early-time Lamb-wave response. Specifically, moving the defect closer to the sensor increases the backscattered amplitude in the displacement field, while increasing damage size introduces additional time-of-flight delays in the stress field due to diffraction effects around a larger obstacle. These complementary physical mechanisms provided the observational foundation for the subsequent AI-based localisation study.

The damage localisation framework, based on two independent Gaussian SVM regression models trained on a hybrid dataset of 385 numerical analyses, achieved cross-validated

R^2 values above 0.81 for both spatial coordinates, with RMSE of approximately 23–25 mm. Validation on 50 unseen analyses yielded a mean Euclidean localisation error of 21.08 mm, demonstrating good generalisation to previously unseen structural configurations, considering the limitations arising from the adopted dataset, the study approximations and the employed software tools.

5.2 Limitations of the Present Work

Despite the encouraging results, several simplifying assumptions limit the scope of the present framework and should be acknowledged.

The numerical model is restricted to single-damage scenarios on simplified flat plates designed to reproduce the external surface of the rover in a schematic manner. Real structural components involve complex geometries, multi-layer composite lay-ups, joints and stiffening elements that are not represented in the current model. Furthermore, all analyses are conducted under idealised boundary conditions and in the absence of environmental variability, including temperature fluctuations, mechanical noise and pre-existing structural variations, which are inherent to operational conditions.

The training dataset, though assembled through a hybrid structured-random strategy, is limited to 385 numerical analyses confined to a specific damage zone and a fixed damage severity (90% stiffness reduction). The predictive models were not exposed to damage outside this zone, to variable damage severities, or to multi-damage configurations, which constrains their generalisation capacity. Finally, the model targets only the x- and y-coordinates of a single localised defect and does not provide information on damage size, orientation, or through-thickness extent.

An additional limitation concerns the accuracy of the labels associated with the randomly generated damage configurations. In particular, the random damage-generation procedure was not implemented in a fully robust manner and therefore some of the coordinates provided to the artificial intelligence model do not exactly correspond to the actual centroid of the cluster of four damaged finite elements. This introduces an intrinsic source of error in the dataset, since part of the prediction discrepancy may originate not only from the regression model itself, but also from an imperfect correspondence between the target labels and the effective physical position of the damage. However, the resulting mismatch is expected to remain comparable to the characteristic length of a single finite element and is therefore limited to a very small spatial scale in the context of the present model. For the same reason, a small number of the 385 analyses are effectively associated with slightly different spatial coordinates even though they correspond to the same set of four damaged finite elements; as a result, identical input signals may be linked to slightly different target positions in the dataset. This inconsistency may have introduced an additional source of ambiguity during training. Owing to time constraints, this issue could not be fully corrected within the present work. Nevertheless, it does not represent a structural limitation of the proposed methodology and could be resolved relatively easily by refining the automatic damage-generation routine so as to compute and store the exact centroid coordinates of the damaged element set and to remove duplicated physical configurations associated with inconsistent labels.

5.3 Application Perspectives for Lunar Missions

The framework developed in this thesis is motivated by the structural monitoring requirements of planetary rovers operating in the lunar environment, where maintenance operations are impossible and structural integrity is critical for mission success.

In this context, a Lamb-wave-based SHM system integrated into the rover's external panels would allow continuous in-situ monitoring of structural health without the need for periodic human inspection. The low-power, embedded nature of piezoelectric actuator-sensor networks makes them well suited to the mass and energy constraints typical of space missions and the purely numerical nature of the present framework makes it possible to design and validate the monitoring system prior to manufacturing.

The lunar environment introduces specific challenges that distinguish it from terrestrial applications. The absence of an atmosphere eliminates acoustic coupling effects but also removes any aerodynamic damping; the wide thermal excursions between lunar day and night induce significant thermo-mechanical stresses and alter the elastic properties of the structural material, potentially shifting the dispersion characteristics of the guided waves. An additional source of uncertainty is related to the integrity of the sensor network itself: piezoelectric transducers bonded to the structural surface may partially debond, degrade, or fail completely due to the combined effect of thermal cycling, vacuum exposure and mechanical vibrations induced by rover locomotion. Such sensor-level anomalies alter the recorded waveforms in a way that is difficult to distinguish from genuine structural damage, potentially leading to false positives or missed detections if not explicitly accounted for in the monitoring strategy. Robust SHM architectures for lunar applications should therefore incorporate sensor self-diagnostic capabilities and fault-tolerant signal processing schemes able to identify and compensate for degraded or missing measurement channels. Furthermore, although piezoelectric sensor networks are inherently low-power, the continuous acquisition and transmission of time-domain signals from multiple channels generate a considerable data volume that requires on-board computing resources capable of handling real-time processing and storage under the strict mass, power and thermal constraints typical of space platforms. These factors must all be accounted for in any operational extension of the present methodology.

5.4 Possible Framework Extensions

The results of this work establish a validated baseline that can be extended along several directions of increasing complexity and realism.

In terms of structural modelling, future work could consider actual composite lay-ups representative of rover panels, curved shell geometries and the inclusion of structural discontinuities such as stiffeners, riveted joints or bonded patches. The introduction of multi-damage scenarios, where two or more defects are simultaneously present, would require a reformulation of the regression problem and a significant expansion of the training dataset.

On the physical side, incorporating environmental variability (particularly the effect of temperature on material properties and on the dispersion characteristics of guided waves)

is essential for operational robustness. In this respect, the MUL2 software framework, offers a solid foundation for such extensions: its native support for hygro-thermo-electro-mechanical coupled analyses allows the direct inclusion of thermal gradients, moisture content and electromechanical coupling effects into the structural model. This capability makes it possible to augment the training dataset with analyses performed at different temperature-dependent material states, capturing the shift in dispersion characteristics induced by thermal excursions in a physically consistent manner. Alternatively, or in combination, transfer learning strategies could be adopted to adapt a baseline model trained under reference conditions to varying environmental states, reducing the number of additional simulations required.

From the machine learning perspective, the regression framework could be extended to predict additional target quantities, such as damage size and severity, by introducing dedicated output variables and corresponding features. More advanced architectures, including convolutional neural networks operating directly on the time-domain waveforms or physics-informed neural networks that embed the governing wave equations as constraints, represent promising avenues for improving both accuracy and physical consistency. Finally, an experimental validation campaign on physical specimens would be a necessary step towards the qualification of the methodology for actual space applications.

Bibliography

[1] National Aeronautics and Space Administration. *Cross-Program Design Specification for Natural Environments (DSNE)*. Tech. rep. SLS-SPEC-159. Washington, D.C.: NASA, 2019 (cit. on pp. 3, 6).

[2] D. E. Wilhelms. *The Geologic History of the Moon*. U.S. Geological Survey Professional Paper 1348, 1987 (cit. on p. 3).

[3] G. Neukum and B. A. Ivanov. «Crater Size Distributions and Impact Probabilities on Earth from Lunar, Terrestrial Planet, and Asteroid Cratering Data». In: *Hazards due to Comets and Asteroids* (1994). Ed. by T. Gehrels, pp. 359–416 (cit. on p. 3).

[4] DA Paige et al. «The Lunar Reconnaissance Orbiter Diviner Lunar Radiometer Experiment». In: *Space Sci Rev* 150 (Jan. 2009), pp. 125–160. DOI: 10.1007/s11214-009-9529-2 (cit. on pp. 3, 5).

[5] Gábor Kalácska, Gyorgy Barko, Hailemariam Shegawu, Ádám Kalácska, L. Zsidai, Róbert Keresztes, and Zoltán Károly. «The Abrasive Effect of Moon and Mars Regolith Simulants on Stainless Steel Rotating Shaft and Polytetrafluoroethylene Sealing Material Pairs». In: *Materials* 17 (Aug. 2024), p. 4240. DOI: 10.3390/ma17174240 (cit. on p. 3).

[6] D. W. I. Carrier, G. R. Olhoeft, and W. Mendell. «Physical Properties of the Lunar Surface». In: *Lunar Sourcebook: A User's Guide to the Moon*. Ed. by Grant Heiken, David Vaniman, and Bevan M. French. Cambridge University Press, 1991, pp. 475–594 (cit. on p. 4).

[7] J. Halekas, Gregory Delory, R. Lin, Timothy Stubbs, and William Farrell. «Lunar Prospector observations of the electrostatic potential of the lunar surface and its response to incident currents». In: *Journal of Geophysical Research* 113 (Sept. 2008). DOI: 10.1029/2008JA013194 (cit. on p. 4).

[8] Telana Jackson, William Farrell, and Michael Zimmerman. «Rover Wheel Charging on the Lunar Surface». In: *Advances in Space Research* 14 (Jan. 2015). DOI: 10.1016/j.asr.2014.12.027 (cit. on p. 4).

[9] Paul Hayne et al. «Global regolith thermophysical properties of the Moon from the Diviner Lunar Radiometer Experiment». In: *The Journal of Geophysical Research Planets* 122 (Dec. 2017), pp. 2371–2400. DOI: 10.1002/2017JE005387 (cit. on p. 5).

[10] Daniel Matthiä and Thomas Berger. *Radiation Exposure and Shielding Effects on the Lunar Surface*. Tech. rep. Nov. 2020 (cit. on pp. 5, 7).

[11] NASA Meteoroid Environment Office. *Meteoroid Engineering Model (MEM): User's Guide and Model Description*. Tech. rep. Model for meteoroid flux at 1 AU; use exact report details if disponibili. NASA, 2019 (cit. on pp. 6, 8).

[12] Md Abdur Rakib, Scott T. Smith, and T. Tafsirojjaman. «A review of shielding systems for protecting off-earth structures from micrometeoroid and orbital debris impact». In: *Acta Astronautica* 223 (2024), pp. 404–425. ISSN: 0094-5765 (cit. on p. 6).

[13] John Zipay, Karen Bernstein, Raymond Patin, Erica Bruno, and Phillipe Deloo. «Structural Verification of the First Orbital Wonder of the World - The Structural Testing and Analysis of the International Space Station (ISS)». In: Apr. 2012. ISBN: 978-1-60086-937-2. DOI: 10.2514/6.2012-1772 (cit. on p. 7).

[14] Eric Christiansen. «Meteoroid/Debris Shielding». In: (Sept. 2003) (cit. on pp. 7, 9, 10).

[15] E Benton and E Benton. «Space radiation dosimetry in low-Earth orbit and beyond». In: *Nuclear instruments & methods in physics research. Section B, Beam interactions with materials and atoms* 184 (Oct. 2001), pp. 255–94. DOI: 10.1016/S0168-583X(01)00748-0 (cit. on p. 7).

[16] Afaf El-Hameed. «Radiation effects on composite materials used in space systems: a review». In: *NRIAG Journal of Astronomy and Geophysics* 11 (Sept. 2022), pp. 313–324. DOI: 10.1080/20909977.2022.2079902 (cit. on p. 7).

[17] Lawrence Townsend. «Overview of active methods for shielding spacecraft from energetic space radiation». In: *Physica medica : PM : an international journal devoted to the applications of physics to medicine and biology : official journal of the Italian Association of Biomedical Physics (AIFB)* 17 Suppl 1 (Feb. 2001), pp. 84–5 (cit. on p. 7).

[18] John Wilson, Jack Miller, A Konradi, and Francis Cucinotta. «Shielding Strategies for Human Space Exploration». In: (Apr. 1998) (cit. on p. 7).

[19] N. C. Costes, J. E. Farmer, and B. G. Edwin. *Mobility Performance of the Lunar Roving Vehicle: Terrestrial Studies; Apollo 15 Results*. NASA Technical Report. NASA, 1972 (cit. on p. 8).

[20] Liang Ding, Keiji Nagatani, Keisuke Sato, Andres Mora, Kazuya Yoshida, Haibo Gao, and Zongquan Deng. «Terramechanics-based High-Fidelity Dynamics Simulation for Wheeled Mobile Robot on Deformable Rough Terrain». In: *Proceedings of the 2010 IEEE International Conference on Robotics and Automation (ICRA)*. Anchorage, Alaska, USA, May 2010, pp. 921–926 (cit. on p. 8).

[21] Erasmo Carrera. «Theories and Finite Elements for Multilayered Plates and Shells: A Unified Compact Formulation with Numerical Assessment and Benchmarking». In: *Archives of Computational Methods in Engineering* 10 (Sept. 2003), pp. 215–296 (cit. on p. 8).

[22] Cláudia Lopes et al. «Smart Carbon Fiber-Reinforced Polymer Composites for Damage Sensing and On-Line Structural Health Monitoring Applications». In: *Polymers* 16.19 (2024) (cit. on p. 9).

[23] Nathan D. Wells and Eric I. Madaras. «The Potential for Health Monitoring in Expandable Space Modules: the Bigelow Expandable Activity Module on the ISS». In: *Proceedings of the 11th International Workshop on Structural Health Monitoring*. 2017 (cit. on p. 9).

[24] NASA. *Meteoroid and Orbital Debris Risk and Mitigation*. Accessed March 22, 2026. 2023. URL: https://ntrs.nasa.gov/api/citations/20230016225/downloads/UA%20NASA%20MMOD%20Squire%20v1.pdf (cit. on p. 9).

[25] «Hypervelocity testing of advanced shielding concepts for spacecraft against impacts to 10 km/s». In: *International Journal of Impact Engineering* 14.1 (1993), pp. 95–106 (cit. on p. 10).

[26] R. Shannon and E. L. Christiansen. *Hypervelocity Impact Testing of Aluminum Foam Core Sandwich Panels*. Tech. rep. Houston, TX: NASA Johnson Space Center, 2015 (cit. on p. 10).

[27] NASA. *Alternative MMOD Shielding Concepts*. Accessed March 22, 2026. 2023. URL: https://ntrs.nasa.gov/api/citations/20230014767/downloads/MMOD_shielding_alternatives_IOC2_6086_v2.pdf (cit. on p. 10).

[28] Arnaud Deraemaeker and Keith Worden. *New Trends in Vibration Based Structural Health Monitoring*. Vol. 520. Jan. 2010. ISBN: 978-3-7091-0398-2. DOI: 10.1007/978-3-7091-0399-9 (cit. on p. 11).

[29] Rahim Gorgin, Ying Luo, and Zhanjun Wu. «Environmental and operational conditions effects on Lamb wave based structural health monitoring systems: A review». In: *Ultrasonics* 105 (2020), p. 106114. ISSN: 0041-624X. DOI: https://doi.org/10.1016/j.ultras.2020.106114. URL: https://www.sciencedirect.com/science/article/pii/S0041624X20300536 (cit. on pp. 11, 49, 50).

[30] Horace Lamb. «On Waves in an Elastic Plate». In: *Proceedings of the Royal Society of London. Series A* 93.648 (1917), pp. 114–128 (cit. on p. 12).

[31] Joseph L. Rose. *Ultrasonic Waves in Solid Media*. Cambridge, UK: Cambridge University Press, 1999 (cit. on p. 12).

[32] Zhi-Fang Su and Larry Ye. *Identification of Damage Using Lamb Waves*. Dordrecht, The Netherlands: Springer, 2009 (cit. on pp. 12, 47).

[33] Peter Cawley and David Alleyne. «The Use of Lamb Waves for the Long Range Inspection of Large Structures». In: *NDT and E International* 29.2 (1996), pp. 77–82 (cit. on p. 12).

[34] Anand Raghavan and Christopher E. Cesnik. «Review of Guided-Wave Structural Health Monitoring». In: *The Shock and Vibration Digest* 39.2 (2007), pp. 91–116 (cit. on pp. 12, 47).

[35] Erasmo Carrera, Marco Cinefra, Michele Petrolo, and Elio Zappino. *Finite Element Analysis of Structures Through Unified Formulation*. Chichester, UK: Wiley, 2011 (cit. on p. 12).

[36] Michele Petrolo. *Advances in Predictive Models and Methodologies for Numerically Efficient Linear and Nonlinear Analysis of Composites*. Cham, Switzerland: Springer, 2019 (cit. on p. 12).

[37] J. N. Reddy. *Theory and Analysis of Elastic Plates and Shells*. 2nd ed. CRC Press, 2007 (cit. on p. 13).

[38] Robert M. Jones. *Mechanics of Composite Materials*. 2nd ed. Philadelphia: Taylor & Francis, 1999 (cit. on p. 19).

[39] Erasmo Carrera. *Finite Element Analysis of Structures Through Unified Formulation*. Chichester, England: Wiley, 2014. ISBN: 9781118536650 (cit. on pp. 22, 24–27).

[40] Marco Petrolo, ed. *Advances in Predictive Models and Methodologies for Numerically Efficient Linear and Nonlinear Analysis of Composites*. Cham: Springer, 2019. ISBN: 978-3-030-11968-3. DOI: 10.1007/978-3-030-11969-0 (cit. on pp. 22, 24).

[41] F. Moleiro, E. Carrera, G. Li, M. Cinefra, and J.N. Reddy. «Hygro-thermo-mechanical modelling of multilayered plates: Hybrid composite laminates, fibre metal laminates and sandwich plates». In: *Composites Part B: Engineering* 177 (2019), p. 107388. ISSN: 1359-8368. DOI: https://doi.org/10.1016/j.compositesb.2019.107388. URL: https://www.sciencedirect.com/science/article/pii/S1359836819319389 (cit. on p. 30).

[42] Mul2 Group Piero Chiaia. *Introduction to MUL2 finite element in-house code*. Internal training material (cit. on p. 35).

[43] Zhongqing Su, Lin Ye, and Ye Lu. «Guided Lamb waves for identification of damage in composite structures: A review». In: *Journal of Sound and Vibration* 295.3–5 (2006), pp. 753–780. DOI: 10.1016/j.jsv.2006.01.020 (cit. on pp. 38, 40).

[44] Faeez Masurkar and Nitesh Yelve. «LambWave Based Experimental and Finite Element Simulation Studies for Damage Detection in an Aluminium and a Composite Plate using Geodesic Algorithm». In: *International Journal of Acoustics and Vibrations* 22 (Feb. 2015), pp. 413–421. DOI: 10.20855/ijav.2017.22.4486 (cit. on pp. 42, 43).

[45] A.G. de Miguel, A. Pagani, and E. Carrera. «Higher-order structural theories for transient analysis of multi-mode Lamb waves with applications to damage detection». In: *Journal of Sound and Vibration* 457 (2019), pp. 139–155. ISSN: 0022-460X. DOI: https://doi.org/10.1016/j.jsv.2019.05.053. URL: https://www.sciencedirect.com/science/article/pii/S0022460X19303220 (cit. on p. 43).

[46] Friedrich Moser, Laurence J. Jacobs, and Jianmin Qu. «Modeling elastic wave propagation in waveguides with the finite element method». In: *NDT & E International* 32.4 (1999), pp. 225–234. ISSN: 0963-8695. DOI: https://doi.org/10.1016/S0963-8695(98)00045-0. URL: https://www.sciencedirect.com/science/article/pii/S0963869598000450 (cit. on p. 46).

[47] Armin Huber. «The Dispersion Calculator - a free software for calculating dispersion curves of guided waves». In: *e-Journal of Nondestructive Testing* 29 (June 2024). DOI: 10.58286/29894 (cit. on p. 63).